Antenna Design and Foreground Characterization for Improved Detection of the Redshifted 21 cm Global Signature During the Epoch of Reionization

by

Thomas J. Mozdzen

A Dissertation Presented in Partial Fulfillment
of the Requirements for the Degree
Doctor of Philosophy

Approved August 2017 by the
Graduate Supervisory Committee:

Judd Bowman, Chair
Christopher Groppi
Evan Scannapieco
Paul Scowen
Rogier Windhorst

ARIZONA STATE UNIVERSITY

December 2017

ABSTRACT

The Universe transitioned from a state of neutral hydrogen (HI) shortly after recombination to its present day ionized state, but this transition, the Epoch of Reionization (EoR), has been poorly constrained by observational data. Estimates place the EoR between redshifts $6 < z < 13$ (330-770 Myr).

The interaction of the 21 cm hyperfine ground state emission/absorption-line of HI with the cosmic microwave background (CMB) and the radiation from the first luminous sources in the universe can be used to extract cosmological information about the EoR. Theorists have created global redshifted 21 cm EoR models of this interaction that predict the temperature perturbations to the CMB in the form of a sky-averaged difference temperature, $T_{\rm b}$. The difficulty in measuring $T_{\rm b}$ is that it is predicted to be on the order of 20 to 100 mK, while the sky foreground is dominated by synchrotron radiation that is 10^5 times brighter. The challenge is to subtract the much brighter foreground radiation without subtracting the $T_{\rm b}$ signal and can only be done when the data has small error levels.

The Experiment to Detect the Global EoR Signature (EDGES) is an effort to measure $T_{\rm b}$ with a single wide field-of-view well-calibrated antenna. This dissertation focuses on reducing systematic errors by quantifying the impact of the chromatic nature of the antenna's beam directivity and by measuring the variability of the spectral index of the radio sky foreground. The chromatic beam study quantified the superior qualities of the rectangular blade-shaped antenna and led to its adoption over the previously used fourpoint-shaped antenna and determined that a 5 term polynomial was optimum for removing the foreground. The spectral index, β, of the sky was measured, using 211 nights of data, to be $-2.60 > \beta > -2.62$ in lower LST regions, increasing to -2.50 near the Galactic plane. This matched simulated results using the Guzmán et al. (2011) sky map ($\Delta\beta < 0.05$) and demonstrated the

exceptional stability of the EDGES instrument. Lastly, an EoR model by Kaurov & Gnedin (2016) was shown to be inconsistent with measured EDGES data at a significance level of 1.9σ.

DEDICATION

I dedicate my thesis to

my wife Barb

who was always supportive of me returning to school to get the PhD which I had placed on the back-burner ever since graduating college in 1979.

ACKNOWLEDGMENTS

I would like to thank my advisor Judd Bowman for his support and guidance during my tenure in graduate school and especially for his courage to take on a non traditional graduate student such as myself. His leadership and commitment were first class and were indispensable to the success of the project and to myself. I also thank my committee members for their wonderful support: Chris Groppi, Paul Scowen, Evan Scannapieco, and Rogier Windhorst.

I would especially like to thank my fellow project members Raul Monsalve and Alan Rogers who were invaluable sources of knowledge and awesome technical discussion partners. I highly value the many fruitful technical discussions we have had over the years. I also thank Nivedita Mahesh who took over antenna simulations from me and continued the effort to advance the accuracy and sophistication of the models. A special thanks to Hamdi Mani who was always willing to show me how to do any lab task that arose.

I would also like to mention the helpful discussions with Danny Jacobs, Sean Bryan, Adam Beardsley, and Boom Kittiwisit on a variety of topics, but especially with Python. I thank all of my colleagues for being a great group of people to socialize with be it picnics for various occasions, barbecues, hikes in the desert, climbing at the Phoenix Rock Gym, or Fridays at Four Peaks that made the graduate student experience great.

A thank you also goes to Larry Clark who helped ease me out of the corporate world by asking me to teach EEE425 in the fall of 2007 while still working at Intel, which then led to me quitting my day job the following semester to work on one of his research grants which could also serve as my EE PhD thesis.

Finally, I want to thank Rogier Windhorst for giving a talk at the Saguaro Astronomy Club in Phoenix in October of the year 2010 in which he ended his talk

by saying "... and we need lots of Post-docs and Grad-students." In the following weeks we had numerous phone conversations that helped me make the decision to change majors and employment status from EE staff in the PhD program to SESE Astrophysics grad student and pursue the Astrophysics degree.

This work was supported by the NSF through research awards for the Experiment to Detect the Global EoR Signature (AST-0905990, AST-1207761, and AST-1609450). EDGES is located at the Murchison Radio-astronomy Observatory. We acknowledge the Wajarri Yamatji people as the traditional owners of the Observatory site. We thank CSIRO for providing site infrastructure and support.

TABLE OF CONTENTS

CHAPTER Page

CHAPTER Page

CHAPTER Page

LIST OF TABLES

LIST OF FIGURES

Figure Page

Figure Page

Figure Page

Chapter 1

INTRODUCTION

1.1 The Epochs of the Universe

Astrophysicists and cosmologists have made great progress increasing our understanding of the history and evolution of the Universe by testing theoretical models against astrophysical observations over the past three decades. The history of the Universe can be organized into several epochs whose onsets are marked by unique characteristic traits (see Fig. 1.1). Within 10 minutes of the Big Bang, nucleosynthesis finished producing all of the baryons of the early Universe, mostly in the form of free protons (HII) and helium nuclei. Photons dominated the expansion of the Universe from 10 s to ∼50,000 yrs after the Big Bang and interacted with matter via frequent scattering. The Universe remained opaque until ∼380,000 yrs when two milestones occurred in a relatively short period of time. First, the nuclei of ionized baryonic matter joined with enough electrons such that the ion density equaled the neutral density, and this event is coined "Recombination" (age ∼377,000). Next, the rate of photon scattering off electrons decreased to the Hubble time, at which time we say that matter and photons decoupled (z ∼1100, age ∼380,000 yrs, T ∼3000 K). The lower density of free electrons resulted in a dramatic increase in the mean free path of photons and gave rise to the cosmic microwave background (CMB) (Loeb & Furlanetto, 2013).

The Recombination event also marked the onset of the Dark Ages Epoch whose duration was from 0.38 to ∼100-200 Myr, where the starless universe was filled mainly with neutral hydrogen (HI) and helium. At this time, there was no radiation from

stars, but the CMB radiation was present, and it interacted with the 21 cm hyperfine ground state of neutral hydrogen. The onset of star and galaxy formation (large scale structure) is loosely constrained and is thought to have occurred ∼100-200 Myr (z∼20-30) after the Big Bang and is sometimes called the epoch of Cosmic Dawn (Bromm & Larson, 2004). As stars, galaxies, quasars, and black holes reionized the intergalactic medium (IGM), the universe transitioned to a transparent state, which it remains in today (Bromm & Loeb, 2003). This transition period is termed the Epoch of Reionization (EoR), whose timing is also loosely constrained, but placed between redshifts of $13 > z > 6$ (age ∼330 to 940 Myr) by current cosmological models (Furlanetto, 2006; Loeb & Furlanetto, 2013). The Universe transitioned from a fully neutral to a fully ionized state in a period of approximately 800 Myr, which is relatively fast considering that the age of the Universe is approximately 14 Gyr (McGreer, Mesinger, & D'Odorico, 2015).

Much knowledge has been obtained about the universe at the time of last scattering via the CMB by using specifically designed equipment such as the Cosmic Background Explorer (COBE) (Mather et al., 1990, 1994), Wilkinson Microwave Anisotropy Probe (WMAP) (Bennett et al., 2013; Hinshaw et al., 2013), and Planck (Planck Collaboration I, 2016). Specifically designed equipment to study the Epoch of Reionization via the 21 cm line has only begun to come online ∼10 years ago. A few examples are interferometry arrays such as the Low-Frequency Array for Radio astronomy (LOFAR[1] first station 2006), the Precision Array to Probe the Epoch of Re-ionization (PAPER[2] 2005), and the Murchison Widefield Array (MWA[3] 2007), as well as the single antenna Experiment to Detect the Global EoR Signature (EDGES

[1]www.lofar.org

[2]http://eor.berkeley.edu/

[3]www.mwatelescope.org

first data 2006). The arrival of these instruments has also spurred the refinement of theoretical models such as the Cosmic Reionization on Computers (CROC) project (Gnedin & Shaver, 2004; Gnedin, 2014; Kaurov & Gnedin, 2016). In recognition of this important area of study, the New Worlds New Horizons (2010) decadal study lists Cosmic Dawn and the Epoch of Reionization as top science priorities.

1.2 Probing the Epoch of Reionization - Scientific Background

The epoch of reionization is the focus of significant theoretical and observational research efforts due to its importance in understanding the events of cosmic evolution. The time of its onset and duration are related to fundamental information about the first stars, galaxies, and accreting black holes, such as their mass, radiative output, and composition (Furlanetto, Oh, & Briggs, 2006; Morales & Wyithe, 2010; Pritchard & Loeb, 2008, 2010, 2012; Mesinger, Ferrara, & Spiegel, 2013). The onset of the epoch is more difficult to determine than the end, which is generally placed at z=6 and estimated by observations of the Gunn-Peterson trough using high redshift Quasars and gamma-ray bursts (GRBs) (Fan et al., 2004, 2006; Mesinger, 2010; Bolton et al., 2011; Chornock et al., 2013; McGreer, Mesinger, & D'Odorico, 2015) and by observing Lyman-α emitting galaxies (Malhotra & Rhoads, 2004; Stark et al., 2010; Pentericci et al., 2011, 2014; Schenker et al., 2013, 2014; Treu et al., 2013; Rhoads et al., 2013; Tilvi et al., 2014). The low-frequency interferometer arrays and the global 21 cm instruments have been steadily increasing in capability and observational constraints have begun to emerge. This information will help guide theorists to narrow the set of possible parameters of cosmic evolution (Bowman & Rogers, 2010b; Zahn et al., 2012; Robertson et al., 2013, 2015; Parsons et al., 2014; Ali, 2015; Pober et al., 2015; Bouwens et al., 2015; George et al., 2015; Planck Collaboration XLVII, 2016).

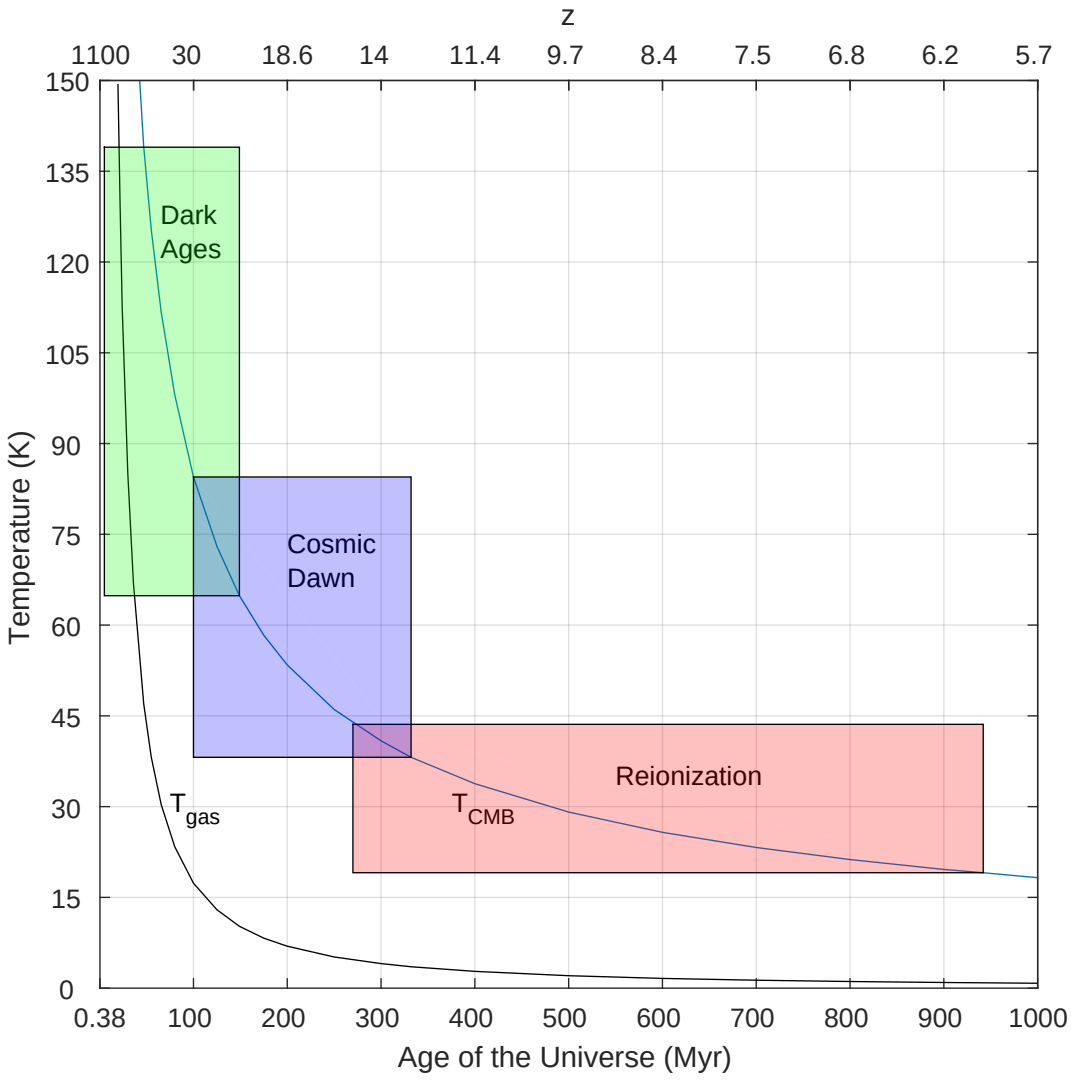

Figure 1.1: Relationship between the age, redshift, and the CMB temperature of the Universe. The IGM temperature was coupled to the CMB until z$\sim$ 150, after which it began to cool faster at a rate of $(1+z)^2$ (Zaroubi, 2013). Assuming no heating yet from the first luminous objects, the IGM would be at 47 and 17 K for redshifts z=50 and 30, respectively, well below the CMB temperature. The continued evolution of the gas temperature does not include eventual heating from UV and X-ray sources. Ages and redshifts calculated using the on-line cosmology calculator Wright (2006), assuming a flat Universe and H_0=69.6 km/s/Mpc.

1.2.1 Summary of EoR Constraints From Non-21 cm Instruments

We briefly mention constraints that have been placed on the timing and duration of the Epoch of Reionization (Liu & Parsons, 2016) from astronomical observations other than those focusing directly on redshifted 21 cm observations (Fig. 1.2).

The South Pole Telescope (SPT) measures secondary anisotropies in the CMB to produce angular power spectra. A main contributor to the power spectra is the kinematic Sunyaev-Zel'dovich (kSZ) effect in which primary CMB photons inverse Compton scatter off clouds of free electrons (with a non-zero bulk velocity) and then are Doppler shifted to higher or lower energies depending upon the orientation of the observer. In a patchy reionization scenario, aided by Monte Carlo reionization simulations, the kSZ power spectra has a strong dependence upon the duration of the reionization epoch. George et al. (2015) and Zahn et al. (2012) report a maximum $\Delta z < 5.7$, with a 95% confidence limit, a 1σ limit of $\Delta z \sim 3$, and a maximum likelihood of $\Delta z = 1.3$. These duration limits are shown in Fig. 1.2 as a horizontal dashed line and by a green horizontal rectangular region near the top of the figure.

The Planck Collaboration XLVII (2016) calculates the optical depth, τ, by measuring E-mode polarization of the CMB, which is caused by CMB photons scattering off free electrons (Thompson scattering). The column density is derived from the optical depth and is related to the occurrence of reionization. Higher optical depth and column density are due to earlier reionization than lower values. Planck Collaboration XLVII (2016) have analyzed several scenarios, and the results from their redshift-asymmetric model places reionization at $z = 8.5 \pm 0.9$, while their redshift-symmetrical model with consideration for SPT data finds $z = 7.8 \pm 0.9$, with a duration of $\Delta z < 2.8$. We show the z_r values ($x_{HI} = 50\%$) and limits as vertical bars in Fig. 1.2.

The limits placed by observations of high redshift quasars, galaxies, and gamma-ray bursts are shown as the triangular region to the right, $\Delta z < 2(z_r - 6)$ (Bouwens et al., 2015). Also shown are two examples of studies that estimate the location of $\bar{x}_{HI}$=50%. Robertson et al. (2015) combine HST star formation rates with Planck optical depth results to set a limit on the beginning of the EoR and to estimate a duration. They conclude that star forming galaxies between $6 < z < 10$ can account for the reionization of the IGM and account for the optical depth calculated by Planck Collaboration XLVII (2016) without the need for significant star forming galaxies before $z > 10$ as would be called for by the WMAP implications that the EoR onset begins near z$\sim$15 with a center value $z_r = 10.5 \pm 1.1$ (Hinshaw et al., 2013; Dunlop, 2013). Greig & Mesinger (2017) quantify existing observations using a Bayesian framework to create a "Golden Sample" estimate, which includes Planck Collaboration XLVII (2016) CMB optical depth calculations and $\bar{x}_{HI}$ dark fractions of high-z QSOs in the Lyman α and β forests.

The white space in the middle of the figure is the parameter space EDGES is working to constrain. Publications in progress are working to rule out faster reionization scenarios at the 1σ and 2σ confidence levels, effectively raising the lower limit on the duration placed by (Bowman & Rogers, 2010b).

1.2.2 The 21 cm Line

At radio wavelengths, the 21 cm hyperfine transition of neutral hydrogen (rest frequency of 1420 MHz) provides a versatile signal for studying the Cosmic Dawn Period and the Epoch of Reionization by probing the temperature and ionization state fraction of neutral hydrogen gas in the IGM. The 1S ground state of neutral hydrogen consists of two closely separated energy levels which differ by 5.9×10^{-6} eV ($\lambda = 21$ cm, $\nu = 1420$ MHz). This hyperfine structure of the ground state is caused

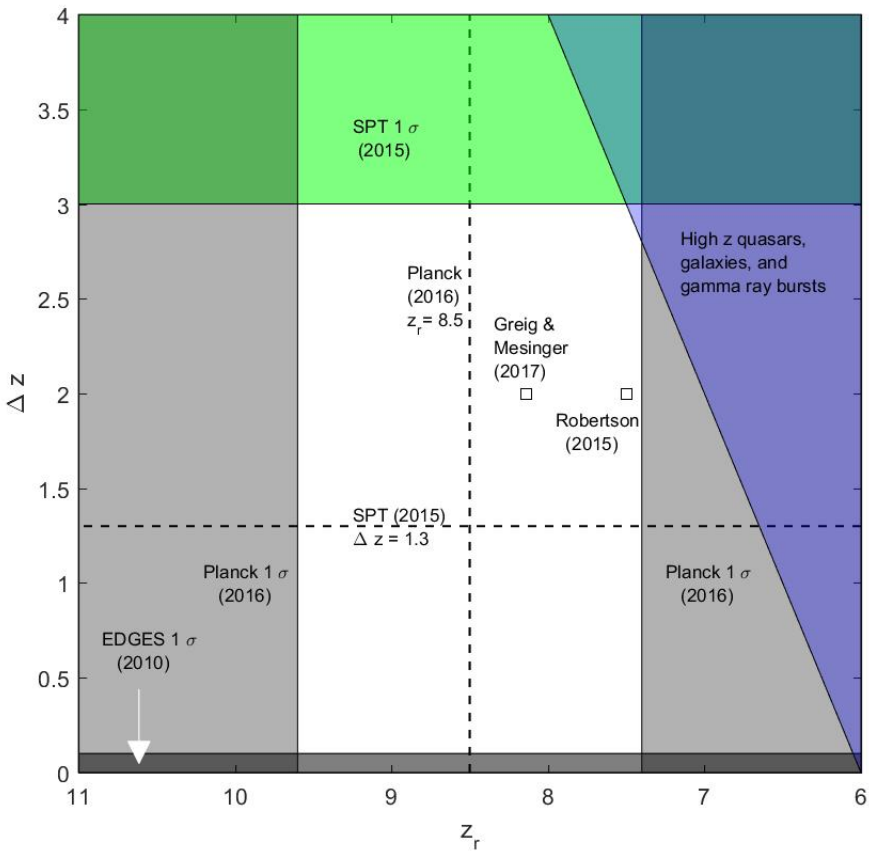

Figure 1.2: Constraints placed on the EoR from CMB measurements reported by the SPT and Planck along with high redshift observations of galaxies, quasars, and gamma ray bursts. The SPT places a limit on the duration of the reionization process to $\Delta z < 5.7$, with a 95% confidence limit, with a maximum likelihood of Δz=1.3 (Zahn et al., 2012; George et al., 2015). A 1σ limit is inferred to be $\Delta z \sim 3$. Planck Collaboration XLVII (2016) analyzes several scenarios and their redshift-asymmetric model places reionization at $z = 8.5 \pm 0.9$, while their redshift-symmetrical model with consideration for SPT data finds $z = 7.8 \pm 0.9$, with a duration of $\Delta z < 2.8$. The limits placed by observations of high redshift quasars, galaxies, and gamma-ray bursts are conservatively shown as the triangular region to the right, $\Delta z < 25(z_r - 6)$ (Bouwens et al., 2015). Also shown are two examples of studies that estimate the location of $\bar{x}_{HI}$=50%. Robertson et al. (2015) combine HST star formation rates with Planck optical depth results to set a limit on the beginning of the EoR and to estimate a duration. Greig & Mesinger (2017) quantify existing observations using a Bayesian framework to create a "Golden Sample" estimate, which includes Planck Collaboration XLVII (2016) CMB optical depth calculations and $\bar{x}_{HI}$ dark fractions of high-z QSOs in the Lyman α and β forests.

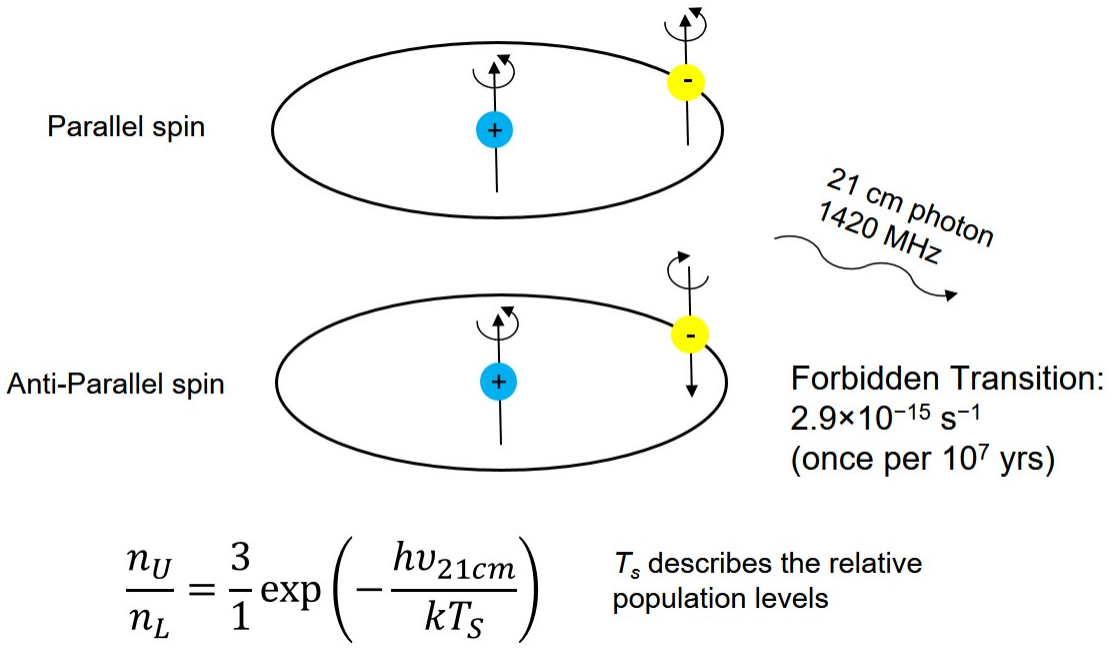

Figure 1.3: Origin of 21 cm radiation in neutral hydrogen

by the interaction of the spin states of the proton and electron which can be oriented either parallel or antiparallel. The higher energy state (parallel) has a degeneracy of 3, and the transition from the upper to lower energy ground state will emit a 21 cm wavelength photon. This is a forbidden transition and rarely happens (once every 10^7 yrs on average), but the abundance of HI in the early universe makes this an important spectral line. Fig. 1.3 depicts the concepts of the 21 cm line.

1.2.3 Theoretical Global (Sky-Averaged or Monopole) Redshifted 21 cm Models of the Epoch of Reionization

As the Universe evolves, the 21 cm line of HI will also evolve as it interacts with its environment and perturb the CMB temperature, giving us clues as to the timing of the onset and strengths of early radiative sources. As such, it is an excellent probe to constrain cosmological models of Cosmic Dawn and the Epoch of Reionization. The

detectable brightness temperature due to redshifted 21 cm emission or absorption from the early IGM is given by (Madau, Meiksin, & Rees, 1997; Fan et al., 2004; Furlanetto, Oh, & Briggs, 2006; Pritchard & Loeb, 2008, 2012) as

$$T_{\rm b}(z) \approx 27 x_{\rm HI} \left(\frac{1+z}{10}\right)^{\frac{1}{2}} \left(1 - \frac{T_{\rm CMB}(z)}{T_{\rm S}(z)}\right) {\rm mK}, \tag{1.1}$$

where $x_{\rm HI}$ is the neutral fraction of the gas, $T_{\rm S}$ is the spin temperature that describes the relative populations of the ground and the hyperfine excited states, and $T_{\rm CMB}$ is the temperature of the cosmic microwave background (CMB) radiation, all of which depend upon z implicitly. It is a difference temperature often denoted by $\delta T_{\rm b}(z)$, but for simplicity we will refer to it as $T_{\rm b}(z)$ or $T_{\rm b}$.

The spin temperature amplitude is affected by UV radiation via the Wouthuysen-Field mechanism (Wouthuysen, 1952; Field, 1958), collisions with IGM gas, and interactions with CMB photons. Thus $T_{\rm b}$ can be either positive or negative depending upon the spin temperature relative to the CMB temperature. The shape of the $T_{\rm b}$ vs redshift curve indicates the relative strength and timing of the early processes mentioned above and theoretical studies have varied the model parameters to produce a variety of scenarios of cosmic evolution (see e.g. Furlanetto 2006; Furlanetto, Oh, & Briggs 2006; Natarajan & Schwarz 2009; Pritchard & Loeb 2010; Morandi & Barkana 2012; Mesinger, Ferrara, & Spiegel 2013). These interactions and the resulting brightness temperature profile are illustrated in Fig. 1.4. A typical set of $T_{\rm b}$ model scenarios is shown in Fig. 1.5.

1.2.4 Cosmological Processes and the Shape of the Brightness Temperature Curve

We now discuss the shape of the $T_{\rm b}$ curve seen in Figs. 1.4 - 1.5. Referring to Eq. 1.1 we note that the sign of the brightness temperature depends upon the comparison of the spin temperature, $T_{\rm S}$, with the CMB temperature, $T_{\rm CMB}$. $T_{\rm b}$ will

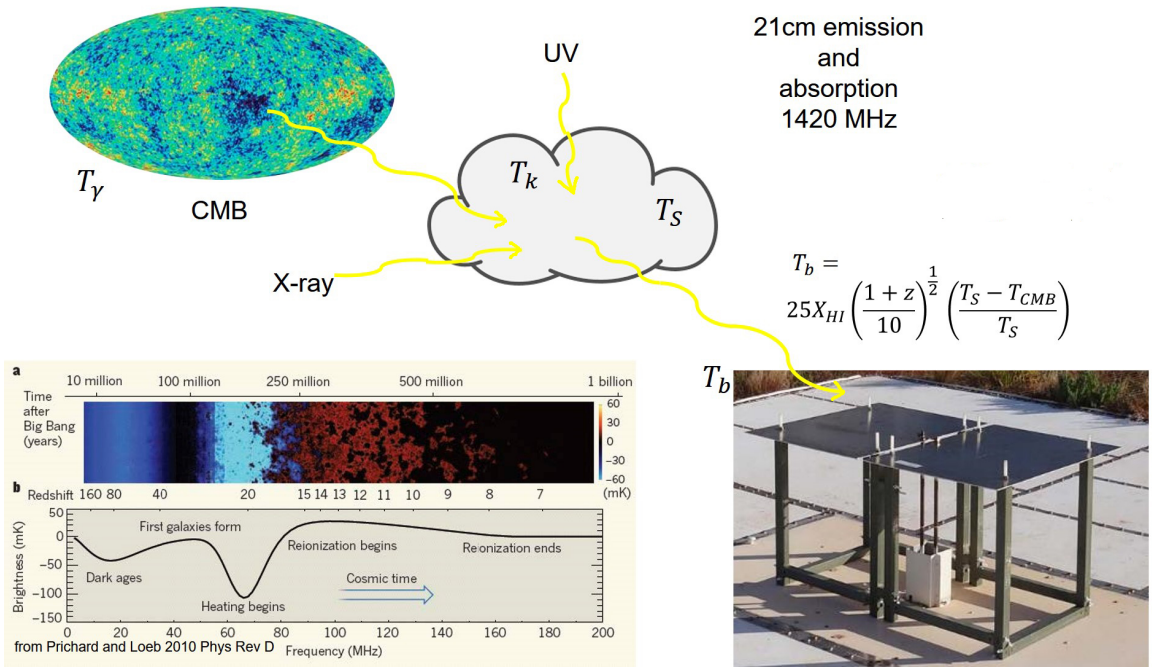

Figure 1.4: Interactions between the CMB, $T_{\rm S}$, UV and X-ray radiation, and the gas temperature, $T_{\rm k}$. The 21 cm line of HI can be in either in an absorbing or emitting state. The interactions between the CMB, the temperature of the HI gas cloud, interacting UV and Xray radiation, and the ground state of the HI atoms are complex. The predicted sky averaged brightness temperature, $T_{\rm b}$, is in the lower left (Pritchard & Loeb, 2010) with a pictoral sky image, before averaging, above it. A picture of the the EDGES blade antenna is at the lower right, and the equation for $T_{\rm b}$ is above the blade antenna. The blade antenna is most sensitive in the frequency range of 90 to 190 MHz which corresponds to a redshift range of $6.5 < {\rm z} < 14.8$.

become zero anytime the spin and CMB temperatures are in equilibrium with each other, i.e., $T_{\rm S} = T_{\rm CMB}$. When $T_{\rm S} < T_{\rm CMB}$, the spin temperature will be able to absorb photons and $T_{\rm b}$ will be negative meaning the HI clouds will be in absorption. Conversely, when $T_{\rm S} > T_{\rm CMB}$, the HI 21 cm line will be in emission.

In the early universe, the HI clouds are dense and colder than the CMB. Because the density is high enough, collisions can couple the spin temperature to the cloud's kinetic temperature, $T_{\rm k}$, which lowers $T_{\rm S}$ below $T_{\rm CMB}$ and puts the 21 cm line of the HI cloud into absorption. As the universe expands and cools, the collision process

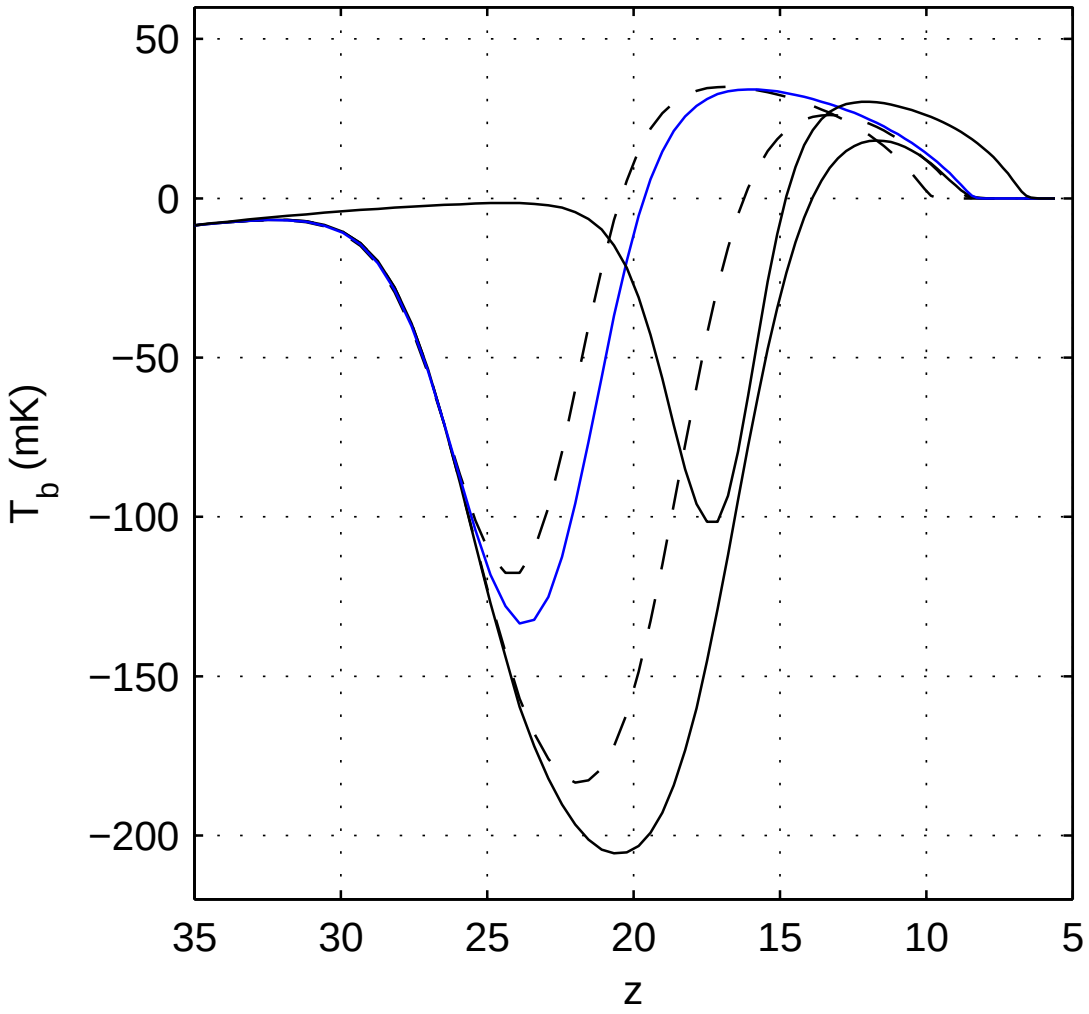

Figure 1.5: A sample of theoretical models for the 21 cm brightness temperature, $T_{\rm b}$, with various values for model parameters (courtesy Mesinger, Ferrara, & Spiegel 2013). The models predict the magnitude of $T_{\rm b}$ to peak between 15 and 40 mK when in emission between redshifts 6 and 20. The absorption trough may be as large as -200 mK between redshifts 15 and 25. Observations are needed to provide constraints to the models.

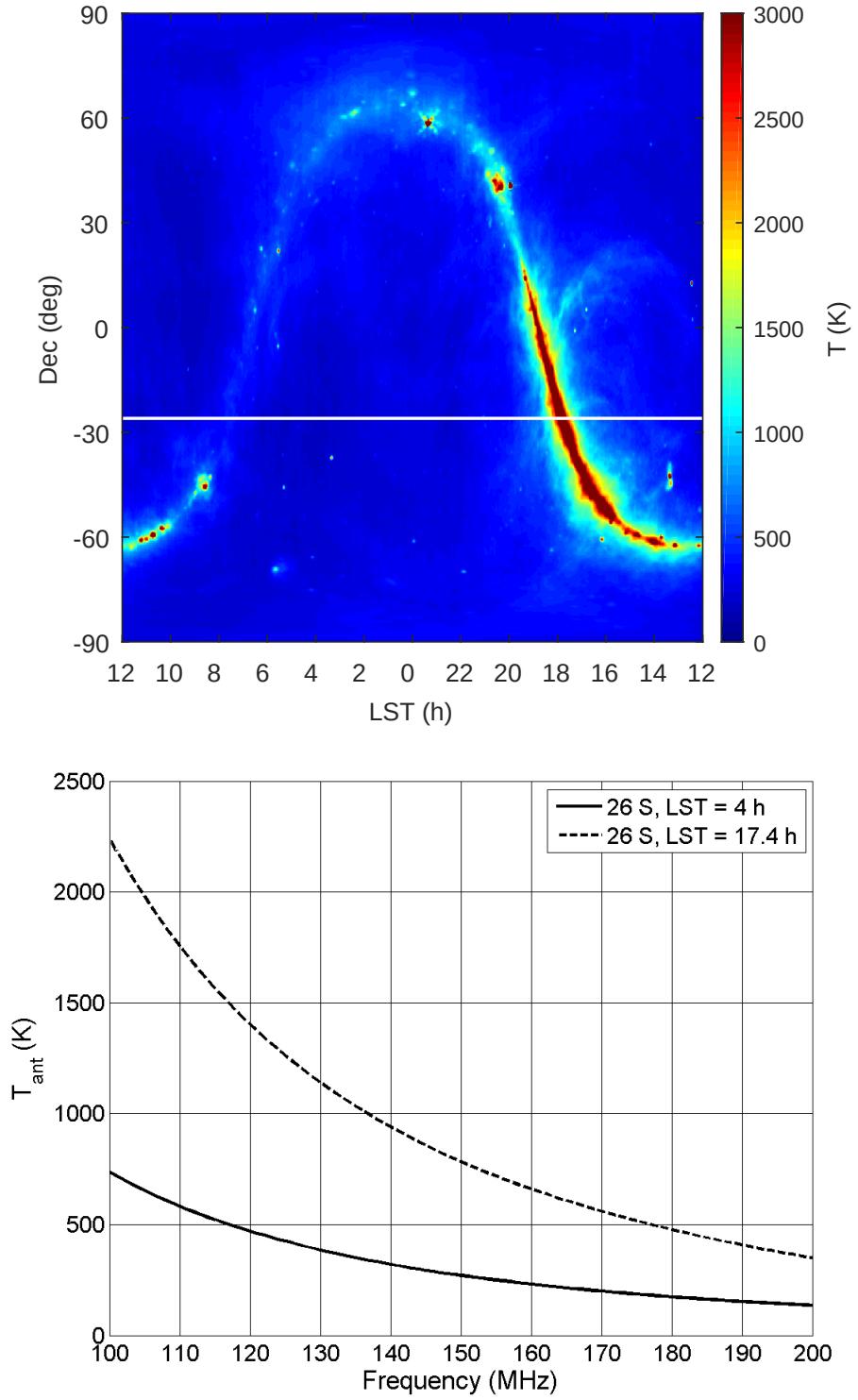

Figure 1.6: A view of the radio sky at 150 MHz extrapolated from the 408 MHz Haslam Sky Map (Haslam et al., 1981)(top). Simulated EDGES antenna temperature (wide field of view) centered at two LST values (4 h and 17.3 h) at the latitude of the EDGES deployment $-26°$ Lat (bottom).

becomes less efficient and $T_{\rm S}$ is driven towards equilibrium with $T_{\rm CMB}$, which decreases $T_{\rm b}$. These processes can be seen in Fig. 1.4 towards the left side of the graph where $30 < \rm z < 100$.

At z$\sim$30 (universe age 100 Myrs) the UV light from the first stars couples the cold HI gas clouds to the spin temperature through the Wouthuysen-Field effect (Wouthuysen, 1952; Field, 1958). This begins the absorption trough because $T_{\rm k} \sim T_{\rm S} < T_{\rm CMB}$. X-ray sources and UV radiation then begin to heat the IGM, which raises $T_{\rm S}$ because it is still coupled to the IGM temperature, $T_{\rm k}$, pushing $T_{\rm S}$ closer to $T_{\rm CMB}$, marking the end of the absorption trough (Madau, Meiksin, & Rees, 1997).

At this point there are two factors affecting $T_{\rm b}$: a) the continued heating of the IGM by X-ray sources and UV radiation (raising $T_{\rm S}$); and b) the ionization of the IGM driving $x_{\rm HI}$ to zero which diminishes the magnitude of $T_{\rm b}$. If the heating continues and happens early enough while the IGM is still mostly neutral, then $T_{\rm S} > T_{\rm CMB} \Rightarrow T_{\rm b} > 0$, and the HI in the IGM will be in emission for the scenarios in Fig. 1.5 for which $6 < \rm z < 20$. If the heating occurs later in time, when the IGM is further along in the reionization process, then the emission phase becomes weaker and may not even exist.

1.2.5 Measurement Approaches

There are two practical approaches to detect the redshifted 21 cm signal. The first method attempts to image the sky by using interferometric arrays, such as the Murchison Widefield Array (MWA; Bowman et al. 2013; Tingay 2013), the Precision Array to Probe the Epoch of Reionization (PAPER; Ali 2015), the Hydrogen Epoch of Reionization Array (HERA; Pober et al. 2015), the Low-Frequency Array (LOFAR; van Haarlem et al. 2013), and the Low-frequency Aperture Array component of the Square Kilometer Array (SKA; Mellema et al. 2013). These arrays aim

to measure spatial fluctuations in the sky brightness temperature on arcminute and degree scales resulting from variations in the density, ionization, and temperature of the intergalactic medium (IGM) above redshift $z > 6$ (below 200 MHz).

The second approach exploits the bulk properties of the high-redshift IGM that yield a global (monopole) contribution of redshifted 21 cm signal to the all-sky radio foreground. This approach is being pursued by EDGES (Bowman, Rogers, & Hewitt 2008; Bowman & Rogers 2010b), Broadband Instrument for Global Hydrogen Reionization Signal (BIGHORNS Sokolowski et al. 2015a), Sonda Cosmológica de las Islas para la Detección de Hidrógeno Neutro (SCI-HI Voytek et al. 2014), Large-aperture Experiment to detect the Dark Age (LEDA Bernardi, McQuinn, & Greenhill 2015), Shaped Antenna measurement of background Radio Spectrum (SARAS Patra et al. 2013; Singh et al. 2015), and the Dark Ages Radio Explorer (DARE; Burns et al. 2012). These projects are described in more detail in the next two sections.

The sky foreground is composed mainly of synchrotron (non-thermal) emission caused by relativistic electrons in the weak Galactic magnetic field (tens of μ Gauss). The electrons originate from supernova remnants inside our Galaxy or from extragalactic sources with active galactic nuclei. Free-free emission also contributes to the diffuse foreground, but is weaker than the synchrotron radiation by two orders of magnitude at 150 MHz. Both diffuse components vary smoothly with frequency and follow a power law characterized by a spectral index β, where $T \sim \nu^{\beta}$, and for synchrotron radiation, it is typically in the range of -2.5 to -2.6 and slightly lower for free-free radiation (Smoot, 1999). The foreground strength is greatest at low Galactic latitudes and weakest at high latitudes. At 100 MHz, the sky foreground near the Galactic center is $\sim$10,000 K, which is five orders of magnitude higher than most EoR model predictions of T_b (see Fig. 1.6). For either of the two EoR signal detection methods, careful and accurate subtraction of the sky foreground is required.

1.3 Global Redshifted 21 cm Efforts Other than EDGES

1.3.1 BIGHORNS

BIGHORNS (**B**roadband **I**nstrument for **G**lobal **H**ydr**O**gen **R**eio**N**isation **S**ignal) is a mobile total-power radiometer. It uses a broadband (20-300 MHz) off-the-shelf biconical antenna (wire frame) that is placed 52 cm above a 3×3 m^2 wire mesh ground screen (Sokolowski et al., 2015a). The front end has a total gain of $\sim 68-75$dB and can switch between the antenna and a known temperature source, namely a 50 Ω terminator. The duty cycle can be set to 7 s or 15.5 s on the antenna with 5 s on the reference in both cases.

The RF signal travels 100m to the backend electronics where it is amplified and filtered. The bandwidth of the ADC is 500 MHz and the signal is sampled at 960 M Samples/s and digitized at 8 bits precision. The empty spectrum above 350 MHz provides a useful diagnostic window for variations in the signal noise floor due to analogue or digital effects. The spectrometer places the data into 4096 channels with spectral resolution of $\sim$117 kHz.

BIGHORNS extracts the EoR brightness temperature by subtracting the simulated expected sky foreground from the measured data. Laboratory calibration was performed to create a baseline for the variation in temperature of the 50Ω termination and integrations reduced the error in the reference temperature down to the single digit mK level.

Data was taken in three different widely separated (400 to 800 km) locations in Western Australia between October 2012 and April 2014: 1) Muresk; 2) Eyre Bird Observatory; and 3) Wondinong Station. Most of the data was taken at Muresk (42 of 54 days) and used for system evaluation and RFI evaluation. Several improvements were made to the instrument based upon the data collected such as improving

the front end impedance isolation, adding a hot load in addition to the ambient calibration load, replacing solid state switches with mechanical switches, and replacing the biconical antenna with a conical log spiral antenna, which has a smoother beam shape over frequency, better matching over frequency to the front end input and the removal of a 3 dB attenuator between the antenna and the first LNA.

Data was also taken at the MRO with the conical log spiral antenna during October 2014 through January 2015 to study ionospheric properties such as electron temperature, magnitude, and optical depth variability (Sokolowski et al., 2015b). They found that the ionosphere was not a limiting factor for ground based EoR instruments because the noise introduced by ionospheric refraction could be averaged down through extended integration times, which conflicts with Datta et al. (2016) who argued that flicker noise caused by ionospheric variability could not be averaged down low enough for ground based EoR measurements. Sokolowski et al. (2015b) found that the ionospheric variability was higher than the expected EoR signal, but was dominated by absorption and emission, and not refraction which is in agreement with Rogers et al. (2015). Suggesting an optimal strategy for removing the ionosphere emission and absorption variability is left for future work.

1.3.2 SCI-HI and PRIZM

SCI-HI (**S**onda **C**osmológica de las **I**slas para la Detección de **H**idrógeno **N**eutro) is a mobile broadband instrument operating in the range of $40 - 130$ MHz (Voytek et al., 2014). It was deployed at Guadalupe Island, Mexico, which is 260 km off the western coast of the Baja California peninsula in the Pacific Ocean at 29°2′ N 118°18′ W.

The antenna is dipole-like and consists of four flat trapezoidal petals tilted upward with an additional panel placed at the end of each trapezoid. The beam width is 55° at 70 MHz. For calibration, the system cycles the receiver's input between the antenna

and three known temperature sources of 0, 50, and 100 Ω terminators. The signals are sampled at a rate of 500 M Samples per second with 12 bits of resolution and then Fourier transformed to generate power spectra from $0 - 250$ MHz. SCH-HI has collected data during 2013 June 1-15 with 4.4 h of integration time at a reduced frequency range of 60-88 MHz. Beam models and sky models (de Oliveira-Costa et al., 2008) were used to aid in calibration and in calculating the expected sky foreground through simulations. From the subtraction of the simulated sky foreground from the calibrated data they concluded that an upper limit could be put on the EoR signal, but that the residuals were too high by one or two orders of magnitude to be able to measure the 21 cm brightness temperature. The residuals were dominated by systematic errors (not thermal noise) and instrument improvements would be needed prior to the next deployment to be able to produce residuals that were of the same temperature as typical 21 cm theoretical EoR models.

PRIZM (**P**robing **R**adio **I**ntensity at high-**Z** from **M**arion) is the second generation follow-on to SCI-HI and was renamed because the antennas and backend electronics were completely redesigned. It will study reionization in the frequency range of 30 to 200 MHz and consists of two new instruments with dual polarization that have bandwidths centered on 70 and 100 MHz. The receiver switches between the antenna and three calibration sources via an electromechanical switch. The signal is sampled at 500 Msamples/s and an FPGA generates the Fourier transform. The antennas are deployed on Marion Island ($-46°53'$ S $037°49'$ E), an island 2000 kms off the coast of Africa with with very low RFI. The 2017 goals were to locate a suitable observing site and insure long term robustness in the field (internal team report Chiang et al. (2017)) by running during the southern hemisphere's winter period.

1.3.3 LEDA

LEDA (**L**arge aperture **E**xperiment to detect the **D**ark **A**ges), is a sub-instrument of the Long Wavelength Array (LWA) at the Owens Valley Radio Observatory (LWA-OVRO), which operates in the frequency range 10-88 MHz (Taylor et al., 2012; Bernardi et al., 2016). LEDA consists of 1) a large-N correlator connected to the LWA array; 2) up to four outrigger dipoles for redundant calibrated total-power measurements; and 3) a data calibration pipeline to recover the full-Stokes sky brightness over a 140° field of view. The array consists of a core of 251 dual-polarization inverted-V dipole-type antennas within a 200-m diameter. There are 4 outrigger antennas a few hundred meters away from the core, which were customized for LEDA. Outrigger spectra are calibrated with a hot and ambient reference load, and the data is digitized at a rate of ∼196 MHz , yielding 4096 channels, 24 kHz wide.

Night-time data was collected on 2016 February 11 and 12 over a 2-hour period centered at LST = 10 h 30 m (quiet sky). Using 19 minutes of effective measurements from a single outrigger antenna, LEDA placed limits on the absorption trough between 50 and 100 MHz ($27.4 > z > 13.2$) in the form of 95% constraints on the amplitude, A_{HI}, and width, σ_{HI}, of a Gaussian model for the trough: $A_{HI} > -890$ mK and $1\sigma_{HI} > 6.5$ MHz ($\Delta z \sim 1.9$ at $z \sim 20$).

1.3.4 SARAS 2

SARAS 2 (**S**haped **A**ntenna Measurement of background **RA**dio **S**pectrum 2) is a portable wide-band wide-field spherical-disc monopole antenna with the receiver electronics placed underneath the antenna, but above the circular solid metallic disk (Patra et al., 2013, 2015; Singh et al., 2017). The bottom of the sphere attaches to the wide end of a cone tangentially and the apex of the cone is near the disk.

This arrangement serves as a balun as the circular disk and the apex of the cone are transformed into an unbalanced input. The disk connects to the outer conductor of a coax cable and the apex of the cone to the center conductor, which then connects to the receiver.

The sphere diameter is 0.292 m and the disk diameter is 0.870 m. The antenna beam is omnidirectional, with a peak at 30° elevation and half power beam width of 45°, but with nulls towards the horizon and zenith. The backend electronics are located 100 m away and operate over a frequency range of 40-250 MHz. The digital spectrometer samples with 10-bit precision and computes 8192-point discrete Fourier transforms. The complex cross-correlation is also measured in each of the 4096 frequency channels between 0-250 MHz.

SARAS 2 was deployed at the Timbaktu Collective in southern India (14°15′ N, Longitude=77°37′ E). Data was collected in the highband range of $110 \leq \nu \leq 200$ MHz over a 4 h period in Sept. 2016. The residuals were generated by fitting the data to a frequency-wise smooth model representing systematic effects and expected sky foreground spectra. 264 global 21 cm models predicted by Cohen et al. (2017) were evaluated and 21 were ruled out with a confidence greater than 1σ. All of the models ruled out were"very late heating" scenarios where the 21 cm EoR signal never goes into emission. Data collection continues with this instrument.

1.3.5 DARE

The **D**ark **A**ges **R**adio **E**xplorer (DARE) program is a proposed space based instrument that would orbit the moon. The first version of the system was described in Burns et al. (2012) and the team has been working on design improvements as described in Burns et al. (2017). The range of operation is from 40-120 MHz with spectral resolution of 50 kHz, a beamwidth of 60° at 60 MHz and less than 17 mK

systematic uncertainty. The antenna consists of a pair of orthogonal biconical dipoles over a ground plane from which the Stokes parameters can be generated. The receiver has an active temperature stabilization to minimize thermal variations. The effectiveness of lunar shielding from earth based RFI is cited as a major advantage for this proposed mission.

Beam directivity can be calibration by measuring the response to artificial circularly-polarized signals generated on the earth by the Greenbank Observatory while the instrument is on the near side of the moon. Instrument calibration is done continuously with 5 plot tones injected across the frequency range, each within one 50 kHz bin and 4 types of tone injection which are enabled for 10 s each. The observation strategy uses 4 quiet-sky direction pointings and instrument simulations along with the calibration information to conduct MCMC analysis in order to extract the EoR signal with 800 h of observation integration. Based upon global redshifted 21 cm cosmological models, this sensitivity is predicted to be adequate to detect the onset of Pop III and PoP II stars and X-ray heating efficiency using refined Bayesian statistical methods.

1.4 The EDGES Program

The EDGES program has been in development since 2006, and at the time functioned as a portable instrument (Bowman, Rogers, & Hewitt, 2008). Many improvements have been made since the first implementation and today there are three permanent installations on site at the Murchison Radio-astronomy Observatory at $-26.7°$ $116°$. In this section we describe the improvements made to the system over time, leading to the present day systems. A chronological list of changes and improvements are summarized in Table 1.1.

Table 1.1: EDGES System enhancement, expansion, and publication history

Site 1 (Receiver above ground)	Dates	Published Papers	Band (MHz)	Ground Plane
EDGES I Fourpoint Ferrite Balun (Fig. 1.7)	Oct 2006 - Oct 2013	Bowman Thesis 2007 Bowman, Rogers, & Hewitt (2008) Rogers & Bowman (2008) Bowman & Rogers (2010a,b) Rogers & Bowman (2012)	100-200	$6'$ mesh
EDGES II Fourpoint Roberts Balun (Fig. 1.8)	Oct 2013 - Oct 2014	Rogers et al. (2015)	90-190	Solid $4' \times 4'$ over a 5 m x 5 m mesh
Site 2 (Receiver below ground)	Dates	Published Papers	Band (MHz)	Ground Plane
EDGES II Fourpoint Roberts Balun (Fig. 1.9)	Oct 2014 - July 2015		90-190	Solid 5.4 m $\times$ 5.4 m + 2 m $\times$ 5 m mesh extensions
EDGES II Highband Blade Roberts Balun (Fig. 1.10)	July 2015 - present	Monsalve et al. (2016) Mozdzen et al. (2016) Monsalve et al. (2017a) Mozdzen et al. (2017) Monsalve et al. (2017b) Mozdzen thesis (this document)	90-190	same as above
Lowband Blade 1 Roberts Balun (Fig. 1.10)	Oct 2015 - present		50-100	Solid 2.2 m $\times$ 2.2 m on 20 m $\times$ 20 m mesh extended to 30 m $\times$ 30 m with 2 m $\times$ 5 m triangles
Lowband Blade 2 Roberts Balun Excitation axis is E-W -All other antennas are N-S	May 2017 - present		50-100	same as above

1.4.1 *The First Implementation of the EDGES Instrument (2006)*

The first implementation of the EDGES instrument was deployed at the Mileura Station in Western Australia and featured a four-point shaped antenna (Suh et al., 2004) with the receiver electronics below the antenna but above ground, a frequency range of $100 - 200$ MHz, and a modest $\sim$2 m diameter ground plane (see Fig. 1.7). One result of this deployment was the measurement of the spectral index from three nights of observation for 0 h $<$ LST $<$ 10 h, which yielded a value of -2.5 ± 0.1 (Rogers & Bowman, 2008). Another result constrained the maximum peak value of $T_{\rm b}$ to be < 450 mK with the assumption of a near instantaneous EoR transition and a systematic error level of 75 mK (Bowman, Rogers, & Hewitt, 2008). This result, along with the calibration process paper Rogers & Bowman (2012), made it clear that the systemic errors needed to be lower in order to more tightly constrain the EoR parameters. Despite these limitations, a loose lower limit on the duration of the EoR transition was found to be no shorter than $\Delta z > 0.06$, which was published in the journal Nature (Bowman & Rogers, 2010b). To make further progress, the systematic errors had to be reduced, and thus the focus of the project shifted to understanding and reducing systematic errors.

1.4.2 *Intermediate Improvement - Oct. 2013 to Oct. 2014*

EDGES was given a permanent location at the Murchison Radio-astronomy Observatory (MRO) in Western Australia ($-26.7°$, $+116.6°$) as it was allowed to co-exist with the Australian Square Kilometer Array Pathfinder (ASKAP) program while sharing electricity and internet connectivity infrastructure. The October 2013 deployment used the fourpoint shaped antenna but improved the balun and ground plane. A lower loss Roberts balun (Roberts, 1957) was implemented along with a

Figure 1.7: An early version of the antenna and receiver deployed in 2006 at the Mileura Station in Western Australia. The receiver was above ground and directly underneath the center of the antenna (see Table 1.1)

shield covering the balun tubes to limit vertical fields. Tuning capacitors were used at the edges between adjacent antenna panels, on top of the antenna in the middle, and between the balun tubes roughly half way between the ground and the panels. A solid $4' \times 4'$ ground plane was placed under the antenna with a rectangular mesh screen (5 m $\times$ 5 m) extending past the ground plane. The receiver was placed in a low profile rectangular box underneath the antenna (Fig. 1.8) and included hardware to enable remote in-situ reflection coefficient measurements of the antenna in the field.

This arrangement was an improvement but several issues were discovered with simulations and data collection. Two sources of asymmetry were discovered: 1) receiver box caused a tilt in the directivity pattern of the antenna beam; and 2) the tuning capacitor on top of the antenna was not electrically symmetric. In addition to these issues, it was speculated that resonances seen in the spectra might be due to the joining of the screen mesh extension panels. The paper by Rogers et al. (2015) was based upon data taken (April-May 2014) in which it was demonstrated that ionospheric variation could be represented by absorption and emission components. This was an important result because EDGES data analysis uses a polynomial for fore-

Figure 1.8: Intermediate upgrade to the EDGES instrument (see Table 1.1). The receiver enclosure can be seen on the central solid ground plane in the center photo. The solid ground plane sits atop a 5 m x 5 m mesh ground plane. The top capacitor is seen in the far right photo and the tuning capacitor is seen between the balun tubes in the left photo, which was taken atop the ISTB4 building at Arizona State University in Tempe, Az. during antenna characterization. Also seen in the left photo in the gaps between the panels at the edges are the quartz spacers used to control capacitance.

ground removal whose frequency dependence can remove this effect. A few months after this data was taken, the EDGES team was asked to relocate the instrument to a different area at the MRO. This move provided the team with an opportunity to implement more extensive improvements.

1.4.3 EDGES II Improvements - New Site Oct 2014 - Operational April 2015

Construction began in October of 2014 on tasks such as ground preparation, trench digging including a pit below the antenna, ground plane assembly, and conduit laying and cable pulling. The ground plane was redesigned and we put the front end receiver electronics underneath it in order to actively control the receiver's temperature with a thermal plate and forced air routed from the control hut. The highband antenna was installed with a solid 5.35×5.35 m^2 ground plane with side extensions of 2×5 m^2 mesh rectangles making it effectively 9.35×9.35 m^2.

Equipment failures and flooding from rain delayed the operation of the fourpoint antenna instrument at the new site until April 2015 at which time it became operational for a brief period (Fig. 1.9). Shortly thereafter the EDGES team decided to switch to the blade antenna and add a lowband (50-100 MHz) instrument. In July 2015 the highband blade began data collection and in October 2015 the lowband blade instrument became operational as well. Backend systems were installed to enable the two systems to run at the same time (Fig. 1.10). The lowband blade antenna's ground plane initially used a 2.2×2.2 m^2 metal panel center with a set of welded mesh screen extensions to make it effectively 10×10 m^2. It was later enhanced in September of 2016 by extending the mesh to 20×20 m^2 and additionally welding 2×5 m^2 triangles to give it an effective size of 30×30 m^2. A second lowband instrument (lowband 2), with the same design as lowband 1, was added in May 2017. It is located 100 m behind the equipment hut such that 150 m separates the two lowband

systems, with the equipment hut between them. The major hardware improvements of the new deployment were:

- electronics underground
  - forced air and active temperature stabilization
  - some weather protection
  - removed the impact on the antenna's directivity
- blade antenna
  - one tuning capacitor instead of six
  - improved reflection coefficient magnitude and smoothness
  - smooth antenna beam directivity
  - no asymmetry in shape
  - easier to simulate
  - lower foreground subtraction residuals
- large ground planes
  - highband with a solid center (5.35×5.35 m^2)
    - Square mesh extensions to 9.35×9.35 m^2
  - lowband with a solid center (2.2×2.2 m^2)
    - Square mesh extensions to 20×20 m^2
    - Triangular mesh extensions to 30×30 m^2
  - improved beam directivity
  - lower ground loss

1.4.4 Brief Calibration Overview

In order to calibrate the system so that the true sky temperature can be recovered from the recorded data, several parameters have to be measured in the field and in the lab. The calibration procedure is quite involved and is covered in Monsalve et al. (2017a). We list the parameters in Table 1.2 that must be measured in lab in order to solve the equations to extract the sky spectra from the instrument's response to the sky. Figure 1.11 shows the internal connections of the receiver and the connection to the backend electronics.

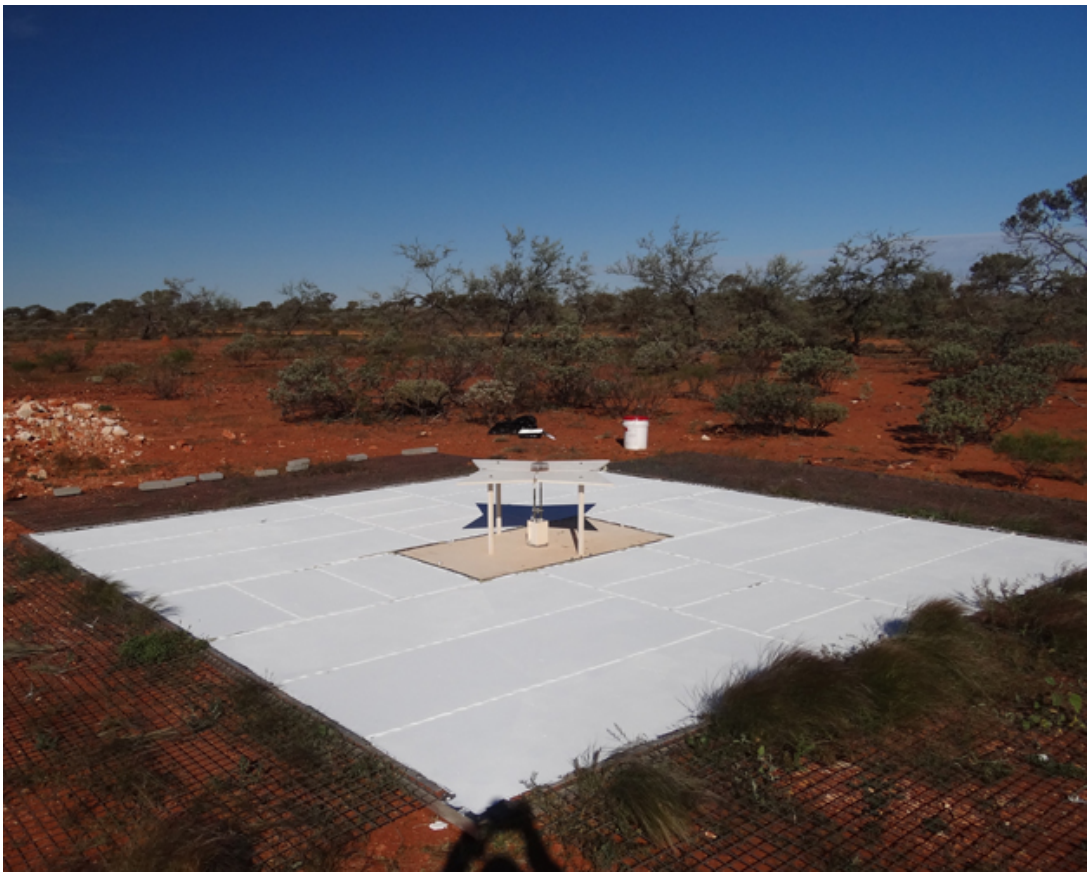

Figure 1.9: The fourpoint antenna (April 2015) would be replaced in July 2015 with the better performing blade antenna (see Table 1.1).

Table 1.2: EDGES calibration and verification loads for spectra recording. These measurements are done at three receiver temperatures of 15, 25, and 35 °C. The load temperatures are not regulated but are exposed to ambient ∼24 °C room temperature but actual load values are logged during spectra recording. The S11 values are measured through the Vector Network Analyzer (VNA) port of the receiver after spectra recording has finished. The long durations are to average down noise in the spectra.

Calibration load	Spectra duration
Long cable (8 m) open termination	24 h
Long cable (8 m) short termination	24 h
Ambient load	48 h
Hot load	48 h
Antenna Simulator (for verification)	72 h

Figure 1.10: Blade highband and lowband systems July 2015 (see Table 1.1). The highband blade can be seen in the foreground along with the solid ground plane and the 2 x 5 m mesh extensions. The lower panels (clockwise from the right) show the inside of the control hut revealing the forced air conduit on the wall on the right in the back, the lowband antenna, and the inside of the highband receiver showing the pink insulating foam on the outside. Between the equipment hut and the highband is the lowband blade antenna. An ASKAP dish can be seen in the background behind the equipment hut.

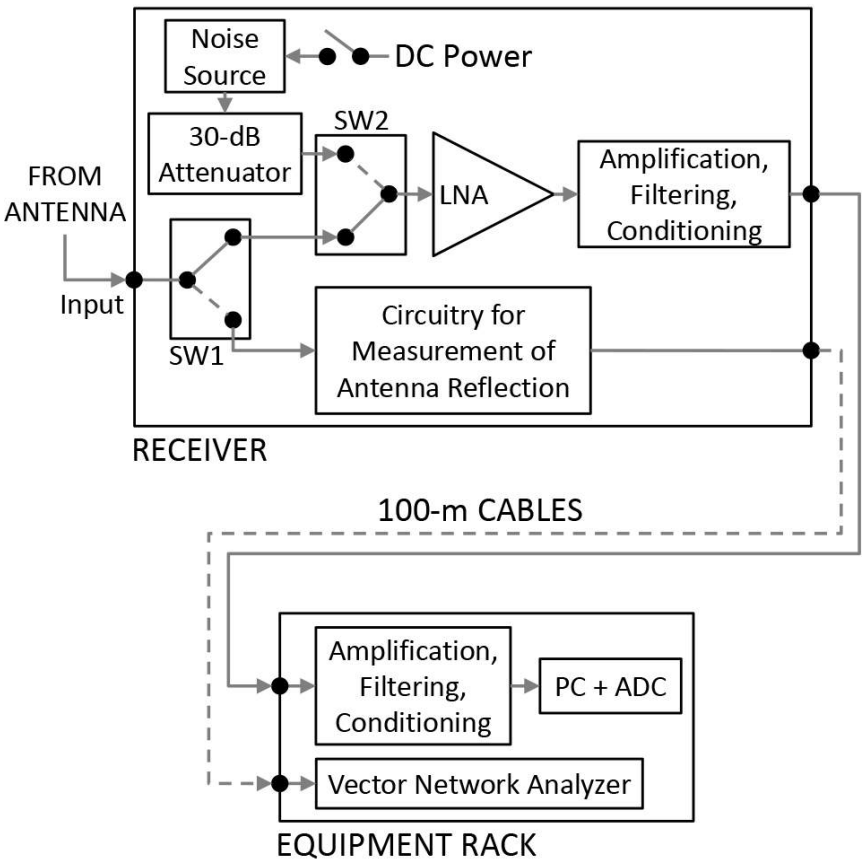

Figure 1.11: EDGES receiver and backend signal paths diagram. Included in the design is a four position switch that connects a VNA port on the receiver to either the antenna or three calibration standards (Open Short Load) which enables the S11 of the antenna to be measured in the field (Monsalve et al., 2017a)

.

There are seven parameters that need to be computed, and these are obtained by measuring the S11 of the receiver, the S11 of the four loads while attached to the receiver, and several hours of recorded spectra and temperature data. All of this is done while regulating the receiver at one of three temperatures: 15, 25, and 35 °C. The loads are not temperature regulated, but exposed to the ambient temperature of the lab (∼24 °C) Each full calibration at one of the temperatures takes 9-10 days to complete.

While the spectra of a load is being recorded, its temperature is logged via a thermistor and a logging resistance meter. The S11 of each load is measured at the

completion of spectra recording via the receiver's internal four (4) position switch that connects a separate Vector Network Analyzer (VNA) port on the receiver to either (1) the antenna or (2-4) any of three calibration standards: Open, Short, and Load (OSL), which are attached directly on the switch. The four position switch needs to be calibrated itself, and this is done by measuring the S11 of the three OSL standards via the VNA port and by measuring the OSL standards attached to the receiver input while the 4 position switch is in the "antenna" position. The S11 of the receiver is typically measured at the beginning, middle, and at the end of the calibration process to reduce the uncertainty in the measurement.

The calibration that can be done in the field is a remote measurement of the antenna's reflection coefficient. This is done to check for changes in the antenna's electrical properties. The other calibration reading is the one that is done with every 39 second spectra recording of the sky, where the ambient noise source, the hot noise source, and the antenna reading are each recorded for approximately 13 seconds each.

1.4.5 Present Instrument Description Summary

We have deployed two versions of the instrument which span neighboring frequency bands of 50-100 MHz and 90-190 MHz. As of July 2017, there are two lowband and one highband systems deployed although we only operate two instruments at a time (the two lowband systems) due to backend equipment limitations. Each instrument consists of a single dipole-based antenna and receiver. Extensive modeling and simulation is performed on all components, along with calibration measurements conducted both in the laboratory prior to deployment and on site following deployment, in order to meet the low systematic instrumental error requirements for redshifted 21 cm observations (Rogers & Bowman, 2012). Throughout this thesis, all results and studies are done with the high-band instrument.

The high-band instrument employs a single broadband "blade" dipole antenna sensitive to wavelengths in the range $3.3 \geq \lambda \geq 1.6$ m ($90 \leq \nu \leq 190$ MHz). The antenna is ground-based and zenith pointing and the excitation axis is aligned NS with a 5° counterclockwise rotation. The antenna consists of two rectangular planar panels that are each 63×48 cm^2 and are placed 52 cm above a ground plane. The metallic ground plane is formed using a solid 5.35×5.35 m^2 aluminum plate, with four wire mesh extensions (2×5 m^2) that combine to form a "plus" shape.

The antenna uses a Roberts Balun (Roberts, 1957), which consists of two 0.5 inch outside diameter brass tubes connected to the ground plane on the bottom and each to an antenna panel on the top. A copper plated brass rod runs inside one of the tubes and connects to the center pin of the receiver's input below the ground plane and on top connects to a rectangular copper plate that connects to the panel on the opposite side. There is a short rectangular shield around the tubes near the base to block possible vertical currents that might develop.

The blade antenna replaces the older "fourpoint" antenna design used in prior EDGES studies because it has better chromatic performance (introduces less spectral structure into the measurement) and it also has a superior reflection coefficient. The blade design also has the advantages of using only one tuning capacitor on top of the balun tubes above the antenna and the rectangular shape of the antenna can be simulated with fewer mesh cells in CST's Time Domain solver giving us higher confidence in the simulation results. The full-width half-maximum beamwidth of the antenna at 150 MHz is 72° parallel to the axis of excitation and 110° perpendicular to the axis.

The input of the front-end receiver connects to a low-noise amplifier (LNA) whose input cycles between the antenna, an ambient load reference temperature, and a hotter load reference temperature. The output of the LNA is amplified and filtered before

being sent to the backend via an underground 100 m coax cable. The signal is digitized and Fourier transformed into frequency components between 90 and 190 MHz in bins of 6.1 kHz wide and the data stored on a computer (see Figs. 1.10 and 1.11).

1.5 Thesis Focus

The focus of the EDGES II project was to reduce the systematic error of the instrument by working on its multiple sources. Much of the early work was focused on studying the antenna beam directivity through CST simulations and removing or accounting for those sources of variability. Some of these sources include simulation accuracy, symmetry of the antenna beam from factors such as tuning capacitors, electronics boxes near the antenna, and the use of finite ground planes. The appendices document two examples of that effort.

Removal of the foreground spectra without removing the EoR signal is a critical step in data analysis. In chapter 2 we investigate the effect of beam chromaticity on foreground removal through computer modeling and the use of the sky foreground maps. The directivity of the antenna beam is not constant with frequency (chromaticity) and the sky foreground has spatial structure. Thus at each frequency, the antenna will uniquely under or over-weigh regions in the sky which leads to different antenna temperatures that can make it difficult to remove the sky foreground cleanly, which obscures the real EoR signal. The analysis also resulted in recommendations for maximizing the signal to noise ratio (SNR) when removing the sky foreground and the quantification of the superiority of a new antenna design over the previous design, which led to the adoption of the new antenna design.

In chapter 3 we analyze several months of data to measure the spectral index of the diffuse radio sky as a function of LST as viewed from $-26.7°$ S with a wide-field antenna. This is valuable scientific knowledge on its own, but it also demonstrated

the accuracy and stability of the EDGES instrument over a long deployment in the field. It also validates the calibration process of the instrument and the removal of the foreground with polynomials.

Chapter 4 analyzes EDGES data to carry out a main goal of the project, namely to set experimental limits on theoretical models of the EoR. For this study we chose a model presented by Kaurov & Gnedin (2016), called the Self-consistent EoR model from the Cosmic Reionization on Computers project. We find the model to be incompatible with the data with a significance of 1.9σ, but small modifications to the model could remove the incompatibility claim.

In the conclusion section we recap the progress we have made in this thesis and outline efforts that can continue to improve the sensitivity of the EDGES instrument that would enable tighter constraints on theoretical EoR models.

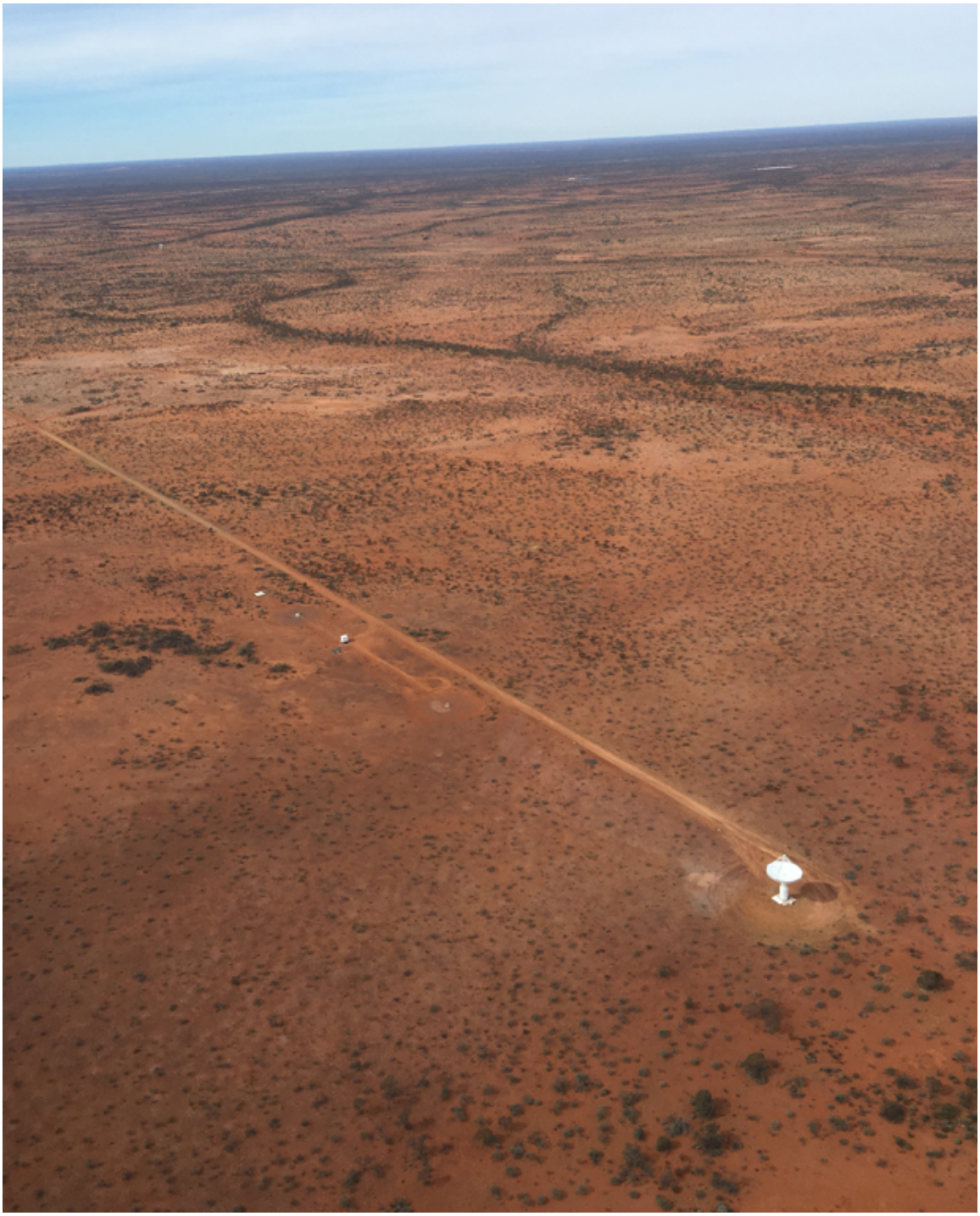

Figure 1.12: Aerial view of the current EDGES installation. The highband antenna is on the far left (100 m from the equipment hut) and the Lowband-1 antenna is between the equipment hut and the highband antenna. The lowband-2 antenna is on the right (also 100 m from the hut) between the hut and the ASKAP radio dish which is in the lower right hand corner of the picture. The road runs approximately EW. Photo courtesy of Lou and Sue Pals.

Chapter 2

LIMITS ON FOREGROUND SUBTRACTION FROM CHROMATIC BEAM EFFECTS IN GLOBAL REDSHIFTED 21 CM MEASUREMENTS

This chapter is a reprint from the published paper: "Limits on Foreground Subtraction from Chromatic Beam Effects in Global Redshifted 21 cm Measurements," Mozdzen T. J., Bowman J.D., Monsalve R. A., Rogers A. E. E., 2016, MNRAS, 455, 3890.

The main findings in this paper are 1) quantification of the degradation of the removal of the diffuse radio sky foreground due to chromaticity in the antenna beam pattern; 2) determination that a 5 term polynomial provides the maximum signal to noise ratio when removing the sky foreground from the measured sky spectrum, while preserving the Epoch of Reionization (EoR) signal; and 3) showing that a blade shaped antenna is significantly less chromatic than a fourpoint shaped antenna.

2.1 Introduction

The epoch of reionisation (EoR) is the focus of significant theoretical and observational research efforts due to its importance in the understanding of cosmic evolution. The time of its onset and duration are related to fundamental information about the first stars, galaxies, and accreting black holes, including mass, radiative output, and composition (Furlanetto, Oh, & Briggs, 2006). Theoretical models place the EoR between redshifts of $20 \gtrsim z \gtrsim 6$, after which the intergalactic medium (IGM) is observed to be fully ionised (Bromm, 2004; Fan et al., 2004; Malhotra & Rhoads, 2004). The duration of the EoR is difficult to predict theoretically (Pritchard &

Loeb, 2010; Mesinger, Ferrara, & Spiegel, 2013) and observational constraints are just beginning to emerge (Bowman & Rogers, 2010b; Zahn et al., 2012; Robertson et al., 2013; Parsons et al., 2014; Ali, 2015; Pober et al., 2015).

At radio wavelengths, the 21 cm hyperfine transition of neutral hydrogen (rest frequency of 1420 MHz) provides a versatile signal for studying the epochs of Cosmic Dawn and Reionization by probing the temperature and ionisation state fraction of neutral hydrogen gas in the IGM. The detectable brightness temperature due to redshifted 21 cm emission or absorption from the early IGM is given by (Madau, Meiksin, & Rees, 1997; Fan, Carilli, & Keating, 2006; Furlanetto, Oh, & Briggs, 2006; Pritchard & Loeb, 2008, 2012)

$$T_{\rm b}(z) \approx 27 x_{\rm HI} \left(\frac{1+z}{10}\right)^{\frac{1}{2}} \left(1 - \frac{T_{\rm CMB}}{T_{\rm S}}\right) {\rm mK}, \tag{2.1}$$

where $x_{\rm HI}$ is the neutral fraction of the gas, $T_{\rm S}$ is the spin temperature that describes the relative populations of the ground and the hyperfine excited states, and $T_{\rm CMB}$ is the temperature of the cosmic microwave background (CMB) radiation, all of which depend upon z implicitly.

The spin temperature amplitude is affected by UV radiation via the Wouthuysen-Field mechanism (Wouthuysen, 1952; Field, 1958), collisions with IGM gas, and interactions with CMB photons. Thus $T_{\rm b}$ can be either positive or negative depending upon the spin temperature relative to the CMB temperature. The shape of the $T_{\rm b}$ vs redshift curve indicates the relative strength and timing of the early processes mentioned above and theoretical studies have varied the model parameters to produce families of resultant curves (see e.g. Furlanetto 2006; Furlanetto, Oh, & Briggs 2006; Natarajan & Schwarz 2009; Pritchard & Loeb 2010; Morandi & Barkana 2012; Mesinger, Ferrara, & Spiegel 2013).

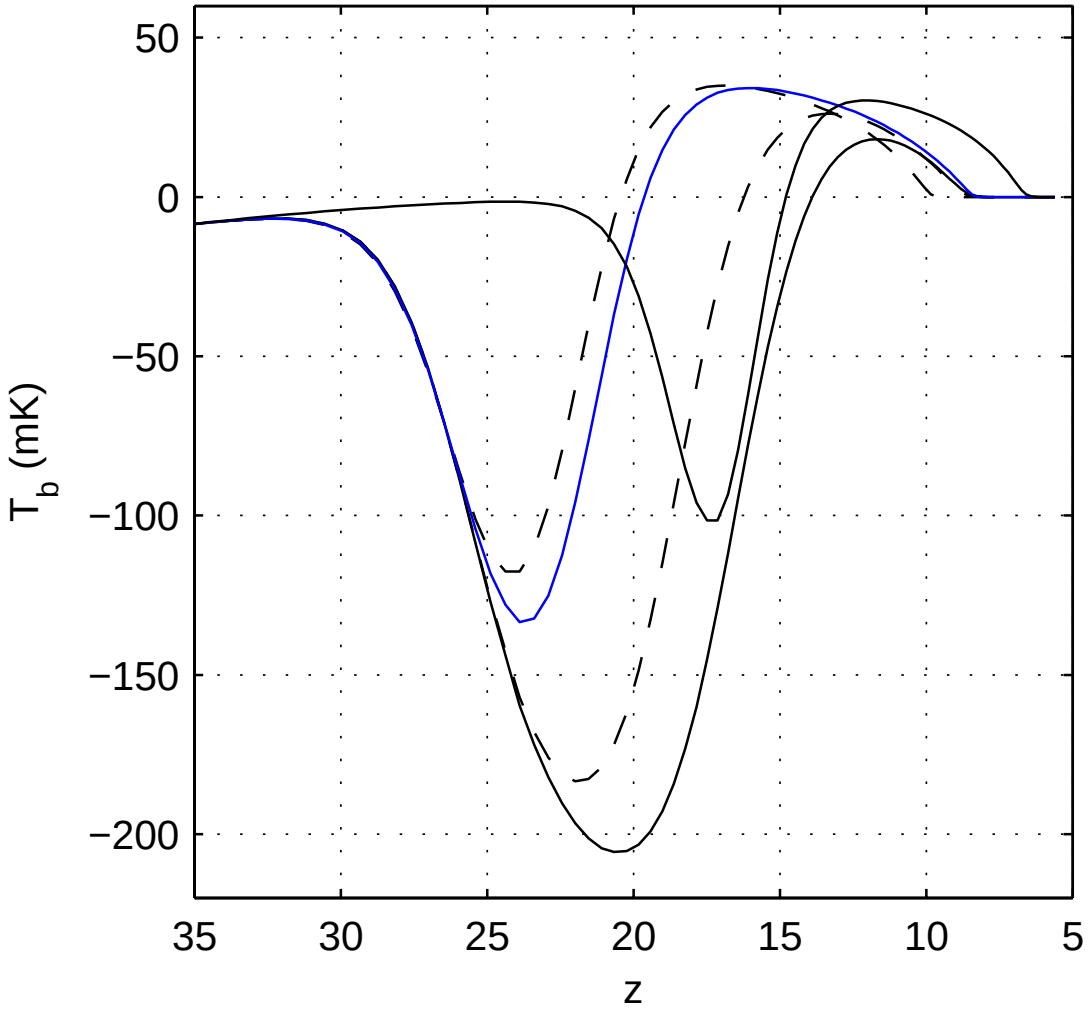

Figure 2.1: A sample of theoretical models for the 21 cm brightness temperature with various values for model parameters (courtesy Mesinger, Ferrara, & Spiegel 2013). The models predict the magnitude of the 21 cm signal to peak between 15 and 40 mK in the interval between redshifts 6 and 20.

There are two main approaches to studying the EoR at radio wavelengths. The first method attempts to detect the EoR statistically, primarily through the redshifted 21 cm fluctuation power spectrum, and eventually to image large structures directly. Efforts such as the Low-Frequency Array for Radio astronomy (LOFAR[1], Zaroubi et al. 2012; van Haarlem et al. 2013), the Precision Array to Probe the Epoch of Re-ionization (PAPER[2], Ali 2015; Pober et al. 2015), the Murchison Widefield Array (MWA[3], Bowman et al. 2013; Tingay 2013), the Square Kilometer Array (SKA[4], Mellema et al. 2013), and the Hydrogen Epoch of Reionization Arrays (HERA[5]) are radio interferometers currently operating or in development that aim to recover the redshifted 21 cm power spectrum.

The second method aims to detect the global 21 cm signal through full sky observations using a single antenna. A global signal antenna will respond to a range of frequencies and $T_{\rm b}(z)$ will correspond to the frequency range of redshifted 21 cm emissions. The predicted spectral signature is broadband between 50 and 200 MHz ($30 \leq z \leq 6$), with a peak absolute amplitude between 10 and 200 mK dependent upon particular star formation model parameters chosen (see Fig. 2.1, data from Mesinger, Ferrara, & Spiegel 2013). Galactic and extragalactic continuum foregrounds from synchrotron and free-free emission are approximately four orders of magnitude larger, with typical sky temperatures of 250 K at 150 MHz away from the Galactic Centre. The foregrounds generally exhibit smooth, power-law-like spectra that must be subtracted from observations to reveal the 21 cm signal.

[1] www.lofar.org

[2] http://eor.berkeley.edu/

[3] www.mwatelescope.org

[4] www.skatelescope.org

[5] http://reionization.org/

Several global 21 cm experiments are in progress using various radio receiver architectures and antenna design styles. The major efforts include the Experiment to Detect the Global EoR Signature (EDGES) (Bowman & Rogers, 2010b), Dark Ages Radio Explorer (DARE) (Burns et al., 2012), Broadband Instrument for Global Hydrogen Reionisation Signal (BIGHORNS) (Sokolowski et al., 2015a), Shaped Antenna measurement of background Radio Spectrum (SARAS) (Patra et al., 2013; Singh et al., 2015), Large-aperture Experiment to detect the Dark Age (LEDA) (Bernardi, McQuinn, & Greenhill, 2015), and Sonda Cosmológica de las Islas para la Detección de Hidrógeno Neutro (SCI-HI) (Voytek et al., 2014). Several studies have addressed experimental calibration issues (Rogers & Bowman, 2012; Patra et al., 2013; Bernardi, McQuinn, & Greenhill, 2015) as well as the frequency dependence of the antenna beams (Raghunathan, Shankar, & Subrahmanyan, 2013; Vedantham et al., 2014; Bernardi, McQuinn, & Greenhill, 2015).

In this study we focus on antenna beam effects in the detection of the global 21 cm signature in the range of $13.2 > z > 6.4$ ($100 < \nu < 190$ MHz) across sky position in right ascension and declination, which we map to the local sidereal time (LST) and latitude of the experiment deployment site. The antenna is a critical element of the EDGES system and since it is not embedded in an array, its beam cannot be readily calibrated as part of the observing program (see Bernardi, McQuinn, & Greenhill 2015). The antenna must be designed carefully and modeled accurately *a priori* to compensate for its characteristics during observations.

The primary design objective for the antenna beam is a directivity pattern that varies smoothly in frequency. Chromatic antenna beams are undesirable because they can couple the relatively large angular fluctuations in the Galactic foreground into spectral structures that may confuse global 21 cm signatures.

Vedantham et al. (2014) have evaluated the chromatic effects of the ionosphere with the LOFAR low frequency antenna beam, and Bernardi, McQuinn, & Greenhill (2015) investigated the chromatic effects of a detailed sky foreground model with analytical forms of the LEDA dipole beam. Here, we compare the chromatic effects of two dipole-based antennas and an idealized reference antenna, over deployment latitude and LST, in the context of the EDGES project. We isolate the effects of the antenna beams by ignoring ionospheric effects and by adopting a power-law model for the foreground emission. In Section 2.2 we describe the antennas and the method used to calculate their response. In Section 2.3 we discuss the results of our simulations and conclude in Section 2.4 with a summary of key findings and a discussion of implications and potential future investigation paths.

2.2 Methods

We base the instrument model in our simulations on the EDGES project (Rogers & Bowman 2008; Bowman, Rogers, & Hewitt 2008; Bowman & Rogers 2010b; Rogers & Bowman 2012). It employs a broadband dipole-like antenna sensitive to wavelengths between 3 and 1.6 meters (100 - 190 MHz). The antenna is connected to a radio receiver that amplifies and conditions the signal before passing it to a digital spectrometer that samples the spectrum with 6 kHz resolution. The receiver utilizes laboratory calibration prior to deployment, augmented with a three-position hot/cold calibration switching scheme during operations (Rogers & Bowman, 2012), to achieve an accuracy of $\sim$0.01 % in measured antenna temperature as a function of wavelength. The impedance match of the antenna connection to the receiver is measured *in situ* by periodically switching a Vector Network Analyzer (VNA) into the electrical path. Although the EDGES calibration scheme is sufficient to correct for undesirable electronic effects in the measured spectrum, it does not compensate for chromatic beam effects.

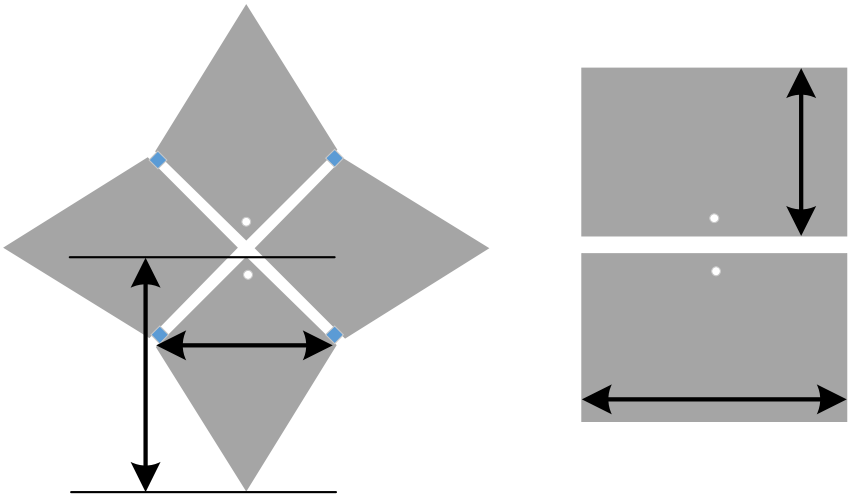

Figure 2.2: Fourpoint antenna (left) and blade antenna (right) are shown in a top view with dimension-indicating arrows to denote the individual panel widths and lengths listed in Table 3.1.

2.2.1 Antennas

In this study, we analyse three horizontal planar dipole-like antennas placed over a ground plane. Each antenna is tuned to respond in the EDGES band. The three antenna types are: 1) The EDGES "fourpoint" antenna deployed to date, which is based on the fourpoint design of Suh et al. (2004); 2) a "blade" design that shows superior beam qualities in simulations and is being considered as a potential successor to the fourpoint design; and 3) an analytic $1/2$-λ wire dipole, which is included as an analytic comparison. The fourpoint and blade antennas are shown in Figs. 2.2 - 2.3 and Table 2.1 summarizes the design and model parameters of the antennas.

Numerical time-domain electromagnetic simulations were performed using CST (Computer Simulation Technology) Microwave Studio for the fourpoint and blade antennas. All of the antenna components were simulated except for fiberglass sup-

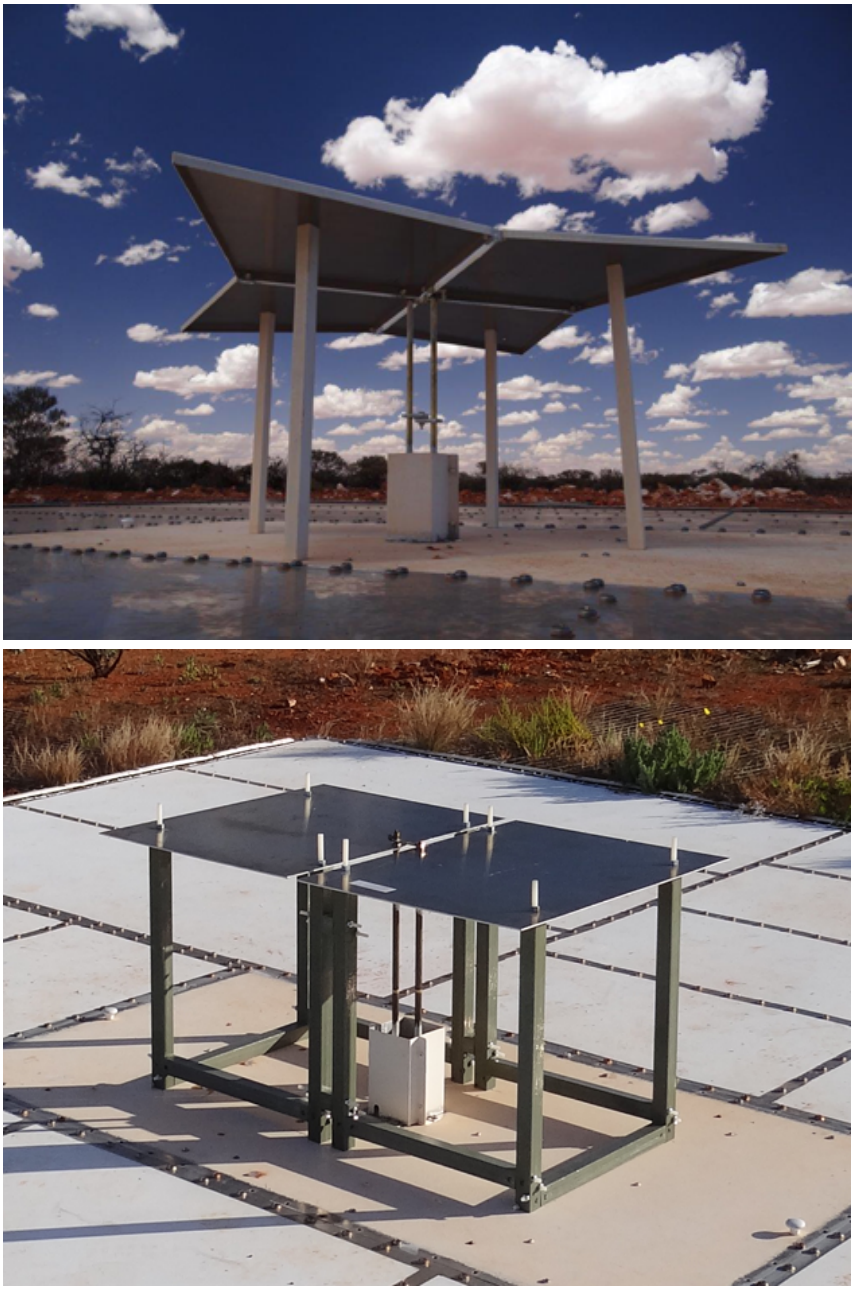

Figure 2.3: (top) Photograph of the fourpoint antenna as deployed by EDGES in 2015. The fourpoint design has a downward pointing rim (1.8 cm) on the perimeter of each panel and uses discrete capacitors between the panels at the outer edge as well as a tuning capacitor half-way up the tubes which are part of the Roberts balun. (bottom) Photograph of the blade antenna which does not use inter-panel capacitors, a balun tuning capacitor, nor a perimeter rim. (common) Both designs use fiberglass support tubes, four for the fourpoint and eight for the blade. Both antennas use a tuning capacitor on the top of the panels between the balun tubes to improve impedance matching. Surrounding the tubes at the base, a short rectangular enclosure shields against vertical currents in the tubes.

port legs and cable connectors. Metal structures were modeled with their actual dimensions and thicknesses, but ground planes were modeled as infinite metal sheets. We found that the choice of CST settings can affect the chromaticity of the modeled beams by introducing numerical artifacts from rounding and precision errors. In particular, we needed to carefully select transient power dissipation thresholds and mesh grid resolutions in order to minimize such artifacts while maintaining efficient processing times. To fine-tune our CST settings, we performed a convergence study in which we perturbed the physical antenna dimensions (by of order 1%) in our CST models while adjusting simulator settings until the resulting outputs converged to small variations. We found this test for convergence of results, using nearly identical antenna models, to be a good probe of the level of numerical artifacts in the antenna simulations.

Our final antenna simulations were performed using CST settings that led to no more than 0.02 dB variations in reflection coefficients between perturbed antenna models over the frequency range of interest and yielded no more than 1.5 mK variations in foreground-subtracted residuals using a 5-term polynomial fit after our full analysis for antennas modeled at -26 degrees latitude with LST of 4 h. The mesh cell counts were 13 million cells for the fourpoint antenna and 6 million cells for the blade antenna. Simulations required approximately 20 min. for the blade and 40 min. for the fourpoint antenna when using an NVIDIA M2090 GPU accelerator. Peak memory requirements were modest at less than 8 GB. We briefly describe each antenna below.

Fourpoint antenna: The fourpoint antenna uses four diamond-shaped panels arranged in a planar structure. One pair of opposing panels is electrically active, while the other pair serves as a parasitic capacitance via a vertical rim along the panel's perimeter, to enhance both the beam's symmetry and the antenna's impedance match

Table 2.1: Antenna Features (refer to Figs. 2.2-2.3)

Antenna	3 dB Beamwidth at 150 MHz		Height above ground plane	Panel Width ⊥ to excitation axis	Panel Length ∥ to excitation axis
	ϕ=0°	ϕ=90°	(cm)	(cm)	(cm)
1/2-λ wire dipole	70°	111°	42.5	N/A	84.9[a]
Fourpoint	66°	105°	51.8	53.0	69.7
Blade	72°	110°	52.0	62.6	48.2

[a]dipole full length

to the receiver (Fig. 2.3). A Roberts transmission-line balun (Roberts, 1957) is used to transition from the panels to the receiver. Discrete tuning capacitors located at roughly the middle of the Roberts balun and near the edges of the panels, along with a capacitive top plate above the central region of the antenna, improve the impedance match of the antenna to the receiver.

EDGES has deployed this style of antenna at the Murchison Radio-astronomy Observatory (MRO) in Western Australia for several observing seasons. A version of this style without the Roberts balun provided the data used to set a lower limit on the duration of the reionisation epoch (Bowman & Rogers, 2010b).

Blade antenna: The blade-shaped antenna is simpler than the fourpoint design, because it uses two flat rectangular panels (no rim on the perimeter), a top capacitor, the Roberts Balun, and a small shield at the bottom (Fig. 2.3). There are no inter-panel tuning capacitors nor a balun tuning capacitor. The beam has less variation with frequency than the fourpoint design as can be seen in Fig. 2.4. The ground plane consists of a 5 m $\times$ 5 m solid aluminum plate underneath the antenna, with

four wire mesh extensions (each 2 m × 5 m) which form a 'plus-shaped' ground plane. This antenna was deployed in the field for the first time in July 2015.

Ideal ½-λ wire antenna: The theoretical reference beam in our study is that of an infinitesimally thin ½-λ horizontal wire dipole antenna placed a quarter wavelength, at a reference wavelength λ_0, above an infinite ground plane. It has a near ideal beam shape that will be explained in subsequent sections. The equation for the beam can be derived from the finite vertical dipole wire antenna (Balanis, 2005) rotated on its side with a ground plane serving as the array factor and is given by:

$$B_{1/2\text{-}\lambda} = \left[\frac{\cos(\frac{\pi L}{\lambda}\cos\theta') - \cos(\frac{\pi L}{\lambda})}{\sin\theta'}\right]^2 \sin^2\left(2\pi h\cos\theta\right), \tag{2.2}$$

where $\theta' = \cos^{-1}(\sin\theta\sin\phi)$, θ and ϕ are the spherical angle coordinates with $\theta = 0$ aligned to principal axis orthogonal to the ground plane and $\phi = 0$ aligned to the active excitation axis of the antenna, L is the full length of the antenna, and h is the height of the antenna above the ground plane in reference wavelengths.

Figure 2.4 shows the beam pattern variation of each antenna model with frequency for $\phi = 0°$ and 90° and illustrates the frequency-dependent variations in these antennas over the wide range of operating frequencies as well as the angular variation with elevation. As common to most dipole-based antennas, all three antennas have large primary beams (fields of view) that span up to ∼110° FHWM. The beam patterns of the antennas vary smoothly with respect to angle and with respect to frequency as viewed in Fig. 2.4, but for global 21 cm measurements, smaller features that vary by less than 1% that are not readily apparent in the figure, can cause undesirable chromatic effects.

When the height of an antenna above the ground plane becomes larger than a quarter wavelength, structures in the beam near the zenith and sidelobes begin to form at that frequency. To avoid this unwanted structure, one would ideally place the

antenna at a quarter wavelength above the ground plane for the highest frequency (shortest wavelength), ensuring that the height remains under a quarter wavelength for all frequencies. However, the height of the fourpoint antenna is chosen as a compromise to optimize the impedance match while keeping the beam shape smooth. For the fourpoint and blade antennas, we use a height above the ground plane that is equivalent to a quarter wavelength at 150 MHz. This produces a minor (< 0.2 dB) local minimum at the zenith for frequencies above 150 MHz. The theoretical $1/2$-λ wire antenna was placed slightly lower above the ground plane, comparable to a quarter wavelength at 176.7 MHz, in order to create local minima of similar amplitude to those from the fourpoint antenna.

2.2.2 Sky Model

The sky foreground model in our simulations is based on the Haslam et al. (1981) map at 408 MHz as shown in Figure 2.5 with approximately 0.6° angular resolution. We model $T_{\rm sky}$ as a simple power law by scaling the sky temperature as a function of frequency according to:

$$T_{\rm sky}(\nu, \boldsymbol{\zeta}) = T_{\rm Haslam}(\boldsymbol{\zeta}) \left(\frac{\nu}{408\,\mathrm{MHz}}\right)^{-\beta}, \tag{2.3}$$

where ν is frequency, $\boldsymbol{\zeta}$ is the sky coordinate vector, and β is the power law spectral index which we set to 2.5 (Rogers & Bowman, 2008). Our sky model does not contain the EoR signal, nor does it include ionospheric distortions (see Vedantham et al. 2014; Datta et al. 2016; Rogers et al. 2015 for a discussion of ionospheric effects). Earlier studies have used 3-parameter sky models (de Oliveira-Costa et al., 2008), and more recently have considered complex sky models of up to $6^{\rm th}$ order (7 terms) (Bernardi, McQuinn, & Greenhill, 2015). We have not included this structure in our sky model in order to maintain simplicity. Using a simple spectral model is sufficient here because

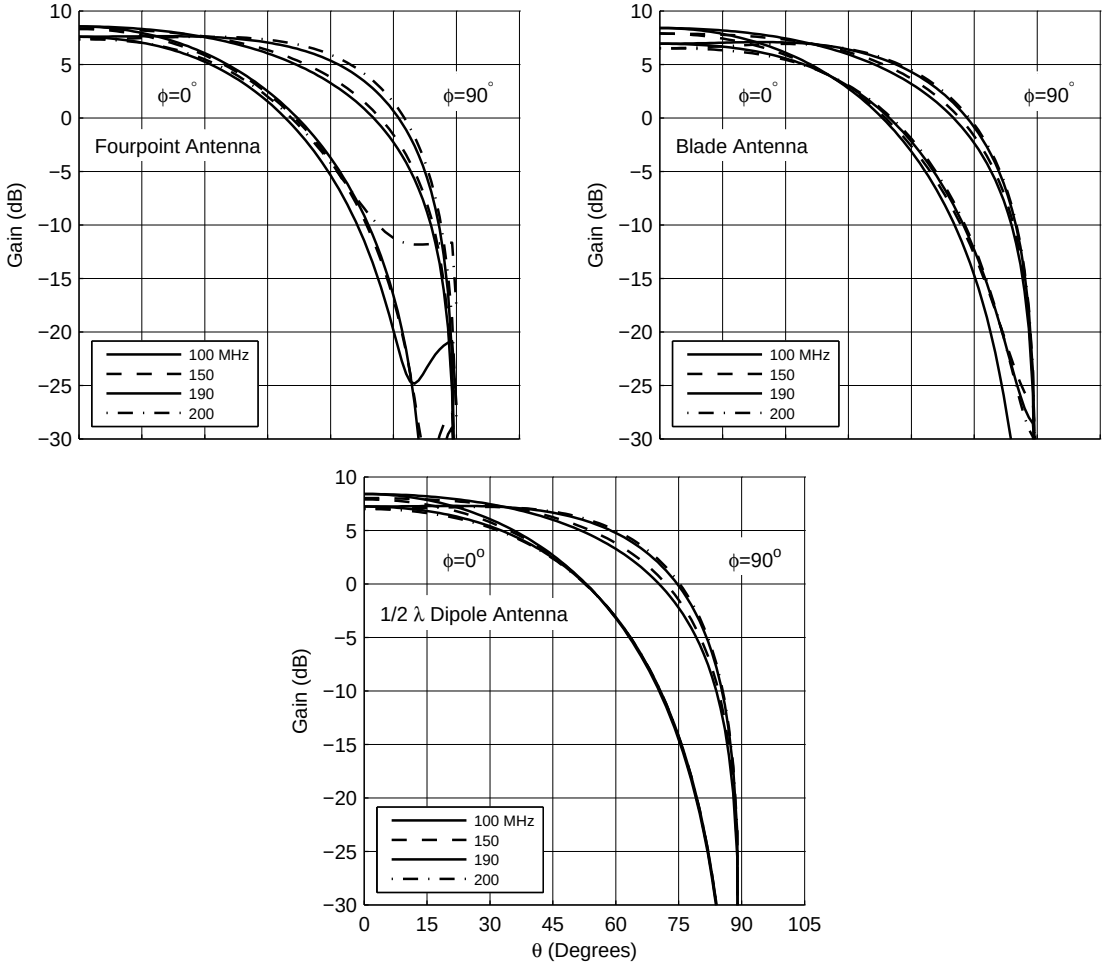

Figure 2.4: Cross-sections of simulated beam patterns for the fourpoint antenna (top left) , the blade antenna (top right) , and the analytic ½-λ wire antenna (bottom) at $\phi = 0°$ (E-plane) and 90° (H-plane) for various frequencies. The active excitation axis of each antenna is defined as $\phi = 0°$. The horizon response ($\theta \approx 90°$) is generally largest and most frequency-dependent for the fourpoint. Non-smooth beam changes are not visible at these scales and are best detected with derivative plots discussed in section 2.3.4.

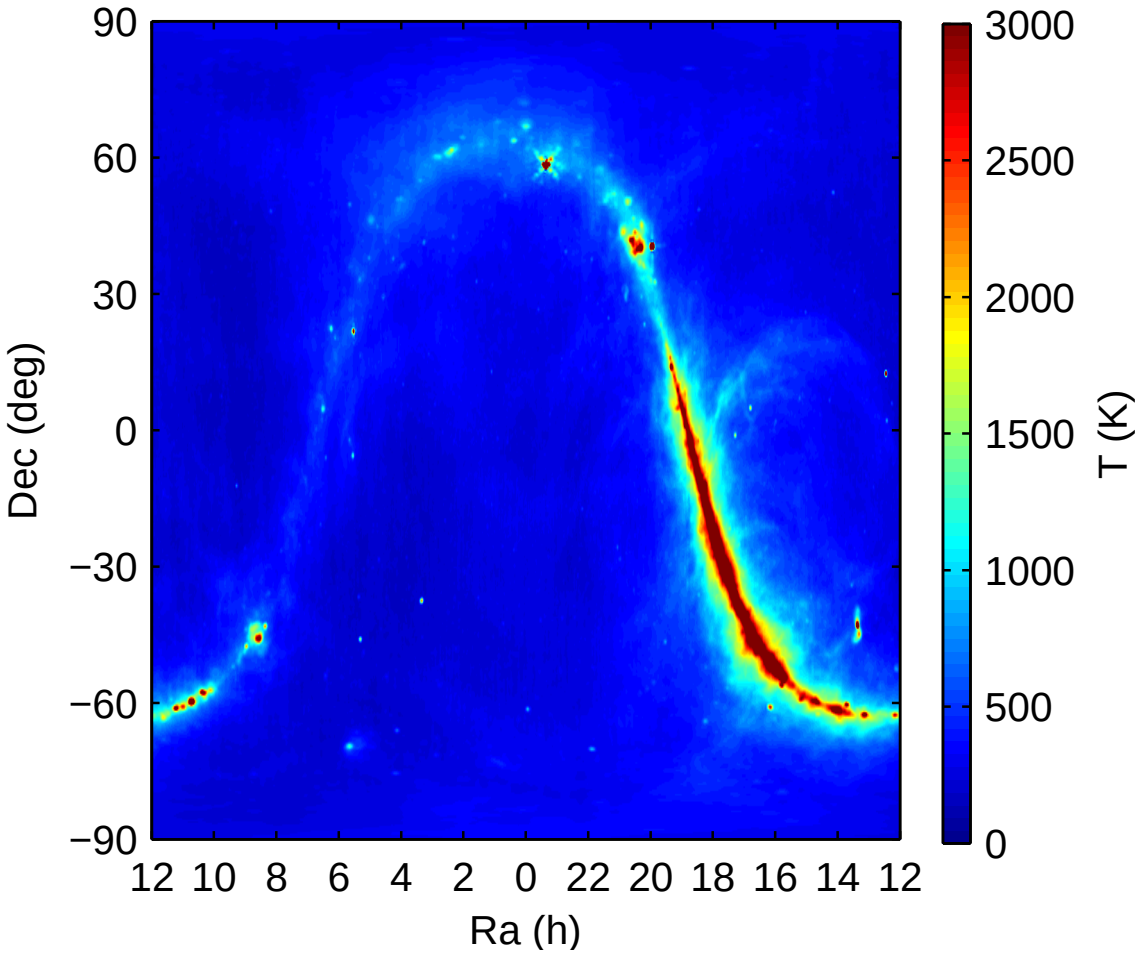

Figure 2.5: Sky model at 150 MHz extrapolated from the 408 MHz sky map of Haslam et al. 1981.

we find (discussed in detail below) that the chromatic effects of our modeled antenna beams produce a larger magnitude of spectral structure at high-orders and, hence, will require similarly high-order model fits. We assume that any complicated spectral structure inherent to the sky will be removed along with the chromatic beam effects.

2.2.3 Measurement Equation

Assuming an ideal receiver, we calculate the simulated antenna temperature using:

$$T_{\rm ant}(\nu, \hat{\boldsymbol{n}}) = \int_{\Omega} T_{\rm sky}(\nu, \boldsymbol{\zeta}) B(\nu, \boldsymbol{\zeta}, \hat{\boldsymbol{n}}) {\rm d}\Omega, \tag{2.4}$$

where $\hat{\boldsymbol{n}}(\alpha, \delta, \psi)$ is the antenna pointing vector and is a function of the right ascension and declination (α, δ) of the primary beam axis that is perpendicular to the antenna ground plane. The orientation of the antenna along its third degree of freedom is specified by the angle of the active antenna axis east of north and is labeled ψ. $B(\nu, \boldsymbol{\zeta}, \hat{\boldsymbol{n}})$ is the chromatic beam for a given antenna, pointing, and orientation, and is normalized to a unit integral at each frequency.

For an antenna on the surface of the Earth pointed toward zenith, the pointing declination of its primary axis corresponds to the latitude of the antenna's deployment site, and the pointing right ascension corresponds to the LST at the site. As the earth rotates, the antenna pointing changes direction, altering the mapping of its beam pattern onto sky coordinates.

2.2.4 Figure of Merit

We define the figure of merit (FoM) for assessing the significance of chromatic beam effects as the RMS residuals to a least squares best fit model:

$${\rm FoM}(\hat{\boldsymbol{n}}) = \sqrt{\left\langle \left[T_{\rm ant}(\nu, \hat{\boldsymbol{n}}) - T_{\rm model}(\nu, \hat{\boldsymbol{n}}) \right]^2 \right\rangle_{\nu}}. \tag{2.5}$$

Chromatic antenna beams that couple little structure into the measured spectrum will produce small FoM values. A good antenna for the global redshifted 21 cm measurement would yield residuals well below the expected 21 cm signal strength of 10 - 40 mK in the frequency range of 100 - 190 MHz while minimizing the number of

free parameters in the model. For our model equation, we use an N-term power-law polynomial given by:

$$T_{\rm model} = \sum_{i=0}^{N-1} a_i \left(\frac{\nu}{\nu_0}\right)^{-2.5+i}. \tag{2.6}$$

This polynomial form generally produces good fits at low-orders in existing EDGES measurements. The antenna temperature produced by our sky model and an ideal beam that is invariant with frequency could be fit exactly with only one term: $T_{\rm model} = a_0\nu^{-2.5}$, but as we will show, realistic antennas require that N≈5.

In order to simultaneously remove the foreground and estimate the global 21 cm signal, the number of terms in $T_{\rm model}$ would have to be augmented with at least one more term to solve for the global 21 cm signature. With a 21 cm model term added to the fitting equation, we define the signal to noise ratio (SNR) to be

$$SNR = \frac{T_{peak}}{[(\sigma_{rms}^2 + \sigma_T^2)(\mathbf{X}^t\mathbf{X})^{-1}_{21\ cm}]^{1/2}}, \tag{2.7}$$

where $T_{peak} = 20$ mK is a nominal value of the global 21 cm peak signal strength, $\sigma_{_T}$ is the typical thermal noise expected from averaging multiple observations, σ_{rms} = FoM is the rms error of the residuals to the fit, and $\sigma_{rms}^2(\mathbf{X}^t\mathbf{X})^{-1}_{21\ cm}$ is the 21 cm auto-covariance term in the covariance matrix. The design matrix $\mathbf{X}$ has N columns (equal to the number of terms in the fitting equation) and one row for every discrete frequency (91 in our case).

We choose a Gaussian shaped 21 cm fitting term inspired by the emission and absorption signatures in Fig. 2.1 in the form of

$$T_{21} = a_{_{N+1}} e^{-\frac{(\nu-\nu_0)^2}{2\sigma^2}}, \tag{2.8}$$

where $\nu_0 = 150$ MHz and σ is related to the Full Width Half Maximum (FWHM) by $\sigma = \text{FWHM}/(2\sqrt{2\ln 2})$. The noise estimate is based upon averaging a week of

observation data using spectral channels of 1.0 MHz and assumes the noise is Gaussian and spectrally flat. Typical values are under 3 mK.

Properly accounting for the effects of covariance between the chromatic foregrounds and the signal parameters requires one to marginalize over foreground parameters. We use the SNR as defined in Eq. 2.7 as an approximate method to account for degeneracies arising from covariance between foreground and signal parameters. Using a higher-order foreground model lowers the RMS error, but raises the covariance of the 21 cm signal estimate which lowers the SNR value, indicating there should also be an upper limit to the number of terms one should use to remove the foreground and this will be explored in Section 4.3. Since $(\mathbf{X}^t\mathbf{X})^{-1}_{21\ cm}$ depends only upon the design matrix X, which is not a function of the antenna, the antenna location, or the antenna pointing, we will focus on our FoM in Section 3 as a sufficient metric for analyzing differences between antennas and pointings.

2.3 Results

In this section we present the FoM for each of the three antenna beam models. We investigate antenna pointings spanning the entire sky in right ascension and declination. In order to facilitate interpretation for ground-based drift-scan experiments, where the pointing parameters are typically dictated by site location and observing time, we label the plots in this section with latitude (declination) and LST (right ascension), although we note that the results are equally valid for proposed space-based experiments such as the Dark Ages Radio Explorer (DARE, Burns et al. 2012) that would more naturally label the pointings with right ascension and declination.

Figure 2.6 shows the FoM as a function of latitude and LST for all three antennas using N=6 polynomial terms. The resolution of the map is 1° in latitude and 4 minutes in LST, yielding a (181×360) data array. As evident in the figure, the

fourpoint antenna yields the worst performance with typical FoM values ranging between 20 and 100 mK. Nevertheless, there are regions of the sky where the FoM reaches 4 mK and observations with a fourpoint antenna can still enable the global redshifted 21 cm measurement. The blade antenna, on the other hand, yields FoM values less than 1 mK over most of the sky, easily facilitating measurement of the global 21 cm signal. The analytic $1/2$-λ wire antenna model produces the best results of all three antennas, with sub-mK residuals. In all three cases, the FoM tends to reach its largest (worst) values when the Galactic plane and/or Galactic Centre is at or above the horizon.

2.3.1 Antenna Orientation

For each antenna model and pointing we investigated two antenna orientations: north-south (NS) aligned and east-west (EW) aligned excitation axis. Orientation of the excitation axis is not a major factor if averaged over the entire latitude-LST range, but for a given latitude, one orientation may prove to have lower FoM values over a particular LST range. For the EDGES deployment, we find that a NS orientation is marginally superior at the deployment latitude of $-26°$ (see Fig. 2.6).

2.3.2 Deployment Latitude

Several sites have been considered and used for global redshifted 21 cm experiments. Latitude 26°S is approximately the latitude of the two SKA sites (in South Africa and Australia). EDGES and BIGHORNS are both currently deployed at the MRO, which is the SKA site in Western Australia. DARE has tested prototype equipment at the MRO, as well as at the Greenbank observatory at latitude 38°N. SCI-HI is deployed at Guadalupe Island off the western coast of Mexico at 29°2'N and is considering deployment at either Isla Socorro (18°48'N) or Isla Clarión (18°22'N).

Two other remote islands that are of interest to global 21 cm projects are Kiritimati (Christmas Island) located 2000 km due south of Hawaii in the middle of the Pacific Ocean near the equator at 1°52N and Tristan da Cunha in the southern Atlantic Ocean between the southern tip of Africa and South America at 37°4S.

The number of terms needed in the $T_{\rm model}$ power-law polynomial fit to remove the chromatic beam and foreground to a certain RMS error level at a specific latitude and LST is dependent upon the type of antenna chosen. We have calculated the FoM for polynomials of length N=3 to 7 and have examined the results. The FoM values decrease as the number of terms in the polynomial increases, resulting in an increase in the number of points with sub-mK level FoM values. The histograms in Fig. 2.7 quantify this trend for N=5 and N=6 for the three antennas. The counts are the number of latitude-LST grid points of the NS orientation of Fig. 2.6 that fall into FoM bins. The histogram plots indicate that the foreground can be removed in more Lat/LST locations with a given polynomial length using the blade antenna than using the fourpoint antenna.

For a given latitude of deployment, we take a cut through the plots of Fig. 2.6 for the blade antenna at latitudes 26°S and 38°N with a NS aligned excitation axis and display the results in Fig. 2.8, which shows the FoM for the blade as a function of LST for polynomial lengths between N=3 and 7. As expected, the FoM improves significantly as the number of polynomial terms is increased. At N=5, the FoM falls below the expected 21-cm signal strength across all LSTs. The fourpoint and analytic $1/2$-λ wire antennas yield similar progressions, but with different overall amplitudes (not shown). Table 2.2 lists the FoM values for polynomials of length 3 through 7 terms for the antennas discussed at latitude $-26°$ at a relatively low FoM region near 4 h and at a relatively high FoM region near 17 h. For this latitude, Table 2.2 indicates that the blade and fourpoint antenna are comparable for low values of N near regions

of low FoM, but the blade performs better for higher values of N and especially for regions of high FoM. All three antenna types listed can remove the sky foreground if six polynomial terms are used, and all but the fourpoint antenna are still acceptable with a 5 term polynomial. For 5-term fits and higher, the FoM performance between each of the three antennas improves by approximately an order of magnitude from the best-case $1/2$-λ dipole, to the blade, to the fourpoint design.

2.3.3 Global 21 cm Signal Detectability

While the above FoM anlysis establishes the relative performance between the antennas and for different pointings, we turn now to the SNR as defined in Eq. 7 to characterize the absolute performance of the antennas. Referring to Table 2.3, a global 21 cm signal with a 20 MHz FWHM parameter is detectable with all 3 antennas using either 5 or 6 polynomial terms in the foreground fitting equation. However, a global 21 cm signal with a 40 MHz FWHM parameter is not detectable (SNR < 2) for any of the antennas when a 6 term polynomial is used, given the assumed noise levels and the given latitude. The low FoM values of the blade antenna for a 5 term fit raises the SNR to 4.6 and 6.7, when the thermal noise is 3 mK and 2 mK respectively, and enables a global 21 cm signal detection even when it has a 40 MHz FWHM.

2.3.4 Spectral Derivative of Antenna Directivity

During antenna design and simulation, visually examining beam plots of directivity vs elevation angle, θ, or even 3D plots at various frequencies will not reveal chromatic issues with the beam, because the magnitude of the relevant beam features are on the order of 0.1 to 1.0 percent. To examine the frequency structure at these small levels of change, we take the derivative of the beam directivity with respect to frequency. Figure 2.9 shows the beam derivative with respect to frequency vs. zenith

Table 2.2: FoM for polynomial lengths between 3 and 7 terms at latitude $-26°$ and two LST values

Antenna	FoM (mK) (LST = 4 h, $-26°$)				
Terms	3	4	5	6	7
Fourpoint	143	19.5	8.20	3.93	3.86
Blade	162	22.2	0.67	0.53	0.07
$1/2$-λ wire dipole	3.45	0.16	0.06	0.01	<0.01
	FoM (mK) (LST = 17 h, $-26°$)				
Fourpoint	2200	219	96.6	33.8	7.44
Blade	999	121	6.60	3.88	0.53
$1/2$-λ wire dipole	118	7.60	0.24	<0.01	<0.01

angle for values of ϕ at $0°$ and $90°$ for the three antennas. Excessive variation (rapid variation or multiple inflection points) in the beam derivative plot will indicate that the antenna will not perform well for 21 cm observations (high FoM values).

Referring to the plots in Fig. 2.9, all antennas show a decrease near the zenith with increasing frequency, consistent with the beginning of structure due to the height above the ground plane becoming a higher fraction of wavelengths as discussed in section 2.2.1. The fourpoint antenna shows greater magnitude changes and additional structure both at the zenith and in other locations compared to the other two antennas. The blade antenna is more similar in amplitude and features to the analytic reference antenna than the fourpoint antenna, and correspondingly, the FoM values of the blade antenna are superior to those of the fourpoint antenna, i.e., the amount of beam structure correlates with FoM values. The more complex shape of the fourpoint antenna, as compared to the blade antenna, may lead to more significant changes in

Table 2.3: SNR for polynomial lengths between 3 and 7 terms at latitude $-26°$ with the Galactic Centre below the horizon. Assumed spectral noise of 2-3 mK achieved by several nights of observational data averaging. One additional Gaussian 21 cm term added to the polynomial terms of the fit equation with FWHM of 20 MHz and 40 MHz.

Antenna	SNR (FWHM = 20 MHz, Noise = 3 mK)				
Poly Terms	3	4	5	6	7
Fourpoint	0.5	2.4	7.8	5.3	5.4
Blade	0.5	1.8	12	7.0	7.0
$1/2$-λ wire dipole	14	13	12	7.0	7.0
	SNR (FWHM = 40 MHz, Noise = 3 mK)				
Fourpoint	0.6	1.1	3.4	0.9	0.9
Blade	0.6	0.8	4.6	1.1	1.1
$1/2$-λ wire dipole	13	5.1	4.7	1.1	1.1
	SNR (FWHM = 20 MHz, Noise = 2 mK)				
Fourpoint	0.5	2.4	8.8	6.4	6.6
Blade	0.5	1.8	17	11	11
$1/2$-λ wire dipole	17	19	18	11	11
	SNR (FWHM = 40 MHz, Noise = 2 mK)				
Fourpoint	0.6	1.1	4.0	1.0	1.1
Blade	0.6	0.8	6.7	1.6	1.7
$1/2$-λ wire dipole	18	7.7	7.0	1.7	1.7

the current flow pattern with frequency and consequently a larger change in beam shape with frequency.

2.4 Conclusion

We evaluated two dipole-based antennas used by EDGES and one idealized reference antenna to assess the effects of frequency-dependent beam shapes on the ability to remove the foreground from global redshifted 21 cm measurements and detect the redshifted global 21 cm signal. Across the full latitude-LST space we found that the fourpoint antenna produced sub 10 mK FoM values in 3% and 12% of the locations for foreground fits using polynomials with 5 and 6 terms respectively, while the FoM values of the blade antenna were below 10 mK in over 99% of the locations for both fits. Furthermore, FoM values of foreground fitting for the blade antenna were below 1 mK in 25 % and 72 % of the locations for 5 and 6 term fits respectively. We note that the optimum choice of E-W or N-S excitation axis orientation depends upon specific deployment location as one orientation was not always better than the other. The fourpoint antenna is only suitable at a few restricted locations on the sky using a 5 or 6 term fit, while the blade antenna provides adequate FoM performance across the entire sky when using a 5 or 6 term polynomial to remove the foreground.

In our simulations, a narrow 21 cm signal corresponding to a rapid reionization over 20 MHz was detectable for all antennas assuming 3 mK of thermal noise. The SNR values indicate detection is favorable for either a 5 or 6 term foreground removal fit. For a 5 term fit, the SNR values of the blade and analytical dipole are nearly the same ranging from 12 to 18, and the fourpoint values range between 7.8 and 8.8. For a 6 term fit, the SNR values of the blade and analytical dipole are the same ranging from 7 to 11, and the fourpoint values range between 5.3 and 6.4 depending upon the thermal noise.

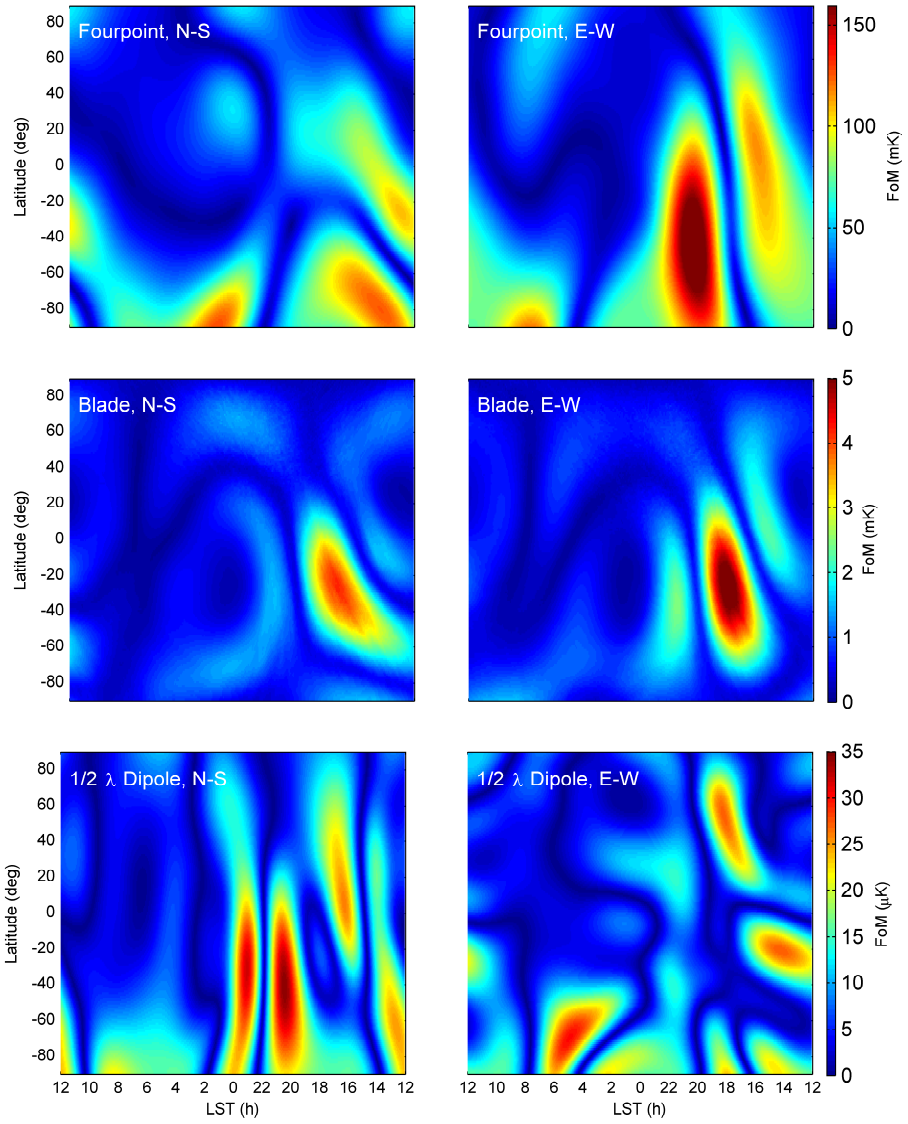

Figure 2.6: FoM as a function of latitude (declination) and LST (right ascension) for the three antennas using a six term polynomial. From top to bottom, the panels show the fourpoint, blade, and analytic dipole models. The excitation axis orientation is NS for the left column and EW for the right column. The colour scale indicates the FoM magnitude and spans a different range for each antenna but is kept constant across the rows. The fourpoint performs the worst and yields acceptably low FoM values (below ∼10 mK) only in a few areas of the sky (dark-blue regions in the top panel). The blade antenna performs well with the FoM below 10 mK across the entire sky. The $1/2$-λ analytic wire dipole model performs the best with sub-mK residuals. The alignment does not greatly affect the distribution of FoM values, but for specific latitudes, one orientation may be better than another, suggesting that orientation choice must be evaluated for both the type of antenna used and the target deployment latitude. In all cases, the performance is best when the Galactic plane is below the horizon and generally worst when the Galactic plane and/or Centre (17 h 45 m LST, $-29°$ dec) are visible near the horizon or at moderate zenith angles.

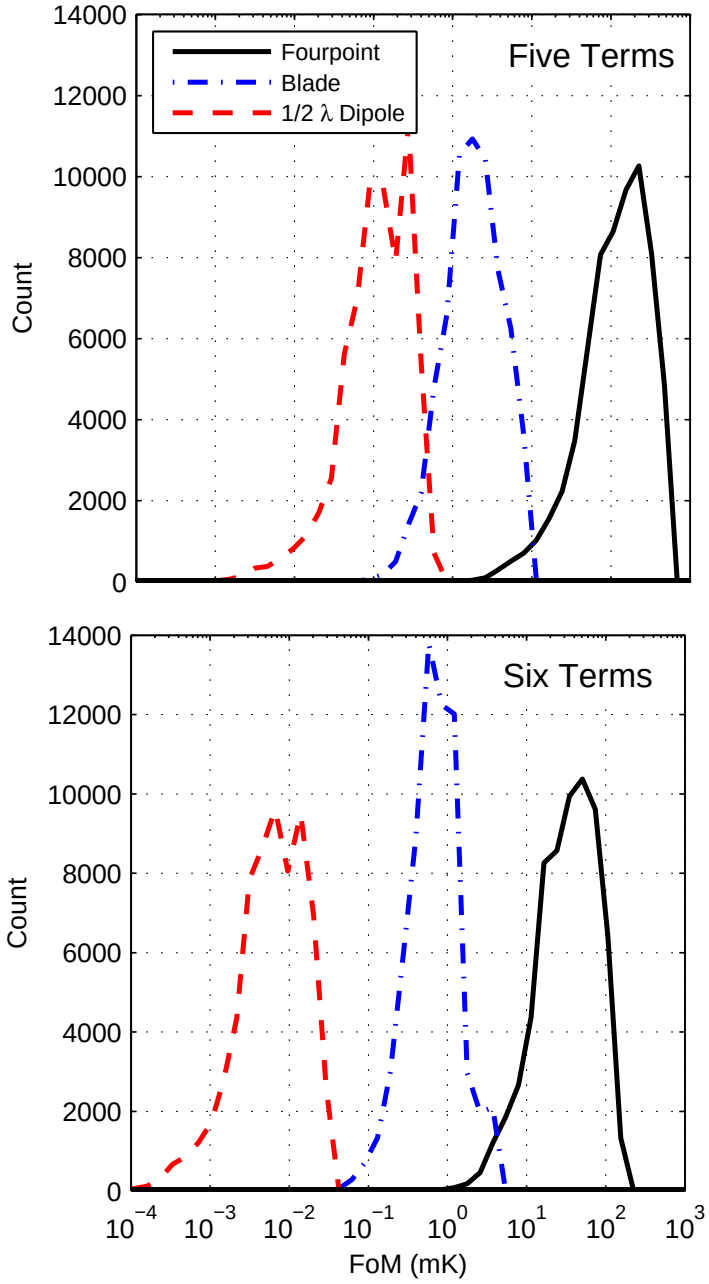

Figure 2.7: Plots of the FoM distribution for the fourpoint, blade, and analytic 1/2-λ wire dipole antennas with a NS orientation for fits to (top) a five term polynomial and (bottom) a six term polynomial. The counts are the number of latitude and LST grid points that fall into FoM bins. The trend towards lower FoM values with increasing polynomial terms is evident as well as the relative performance of the three antennas. The fourpoint FoM is below 10 mK for 3% of the data points using a 5 term fit and 12% for a 6 term fit, while the blade is below 10 mK for 99.7 % of the data points. The blade FoM is an order of magnitude better as the FoM is below 1 mK for 25% of the data points using a 5 term fit and 73% for a 6 term fit.

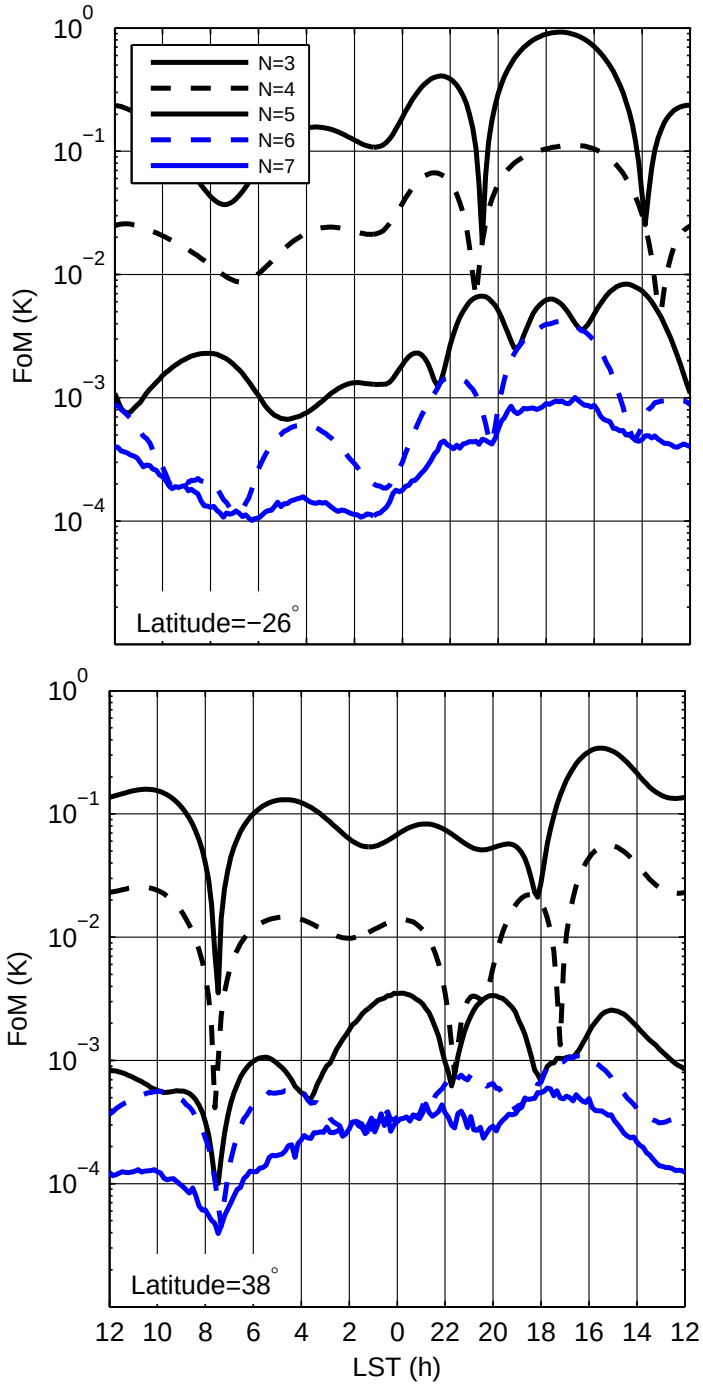

Figure 2.8: Blade FoM vs LST at latitude −26° (top) and latitude 38° (bottom), which correspond approximately to the latitude of the SKA sites in South Africa and Australia, as well as the EDGES fourpoint location, and to the latitude of the Greenbank Observatory respectively. The antenna excitation axis is aligned NS. The curves illustrate the effects of varying the number of polynomial terms in the $T_{\rm model}$ fit, from N=3 (top) to N=7 (bottom). For this antenna, acceptable FoMs were achieved with as few as 5 polynomial terms. The fourpoint and analytic $1/2$-λ wire antennas show similar progressions, but with different relative amplitudes.

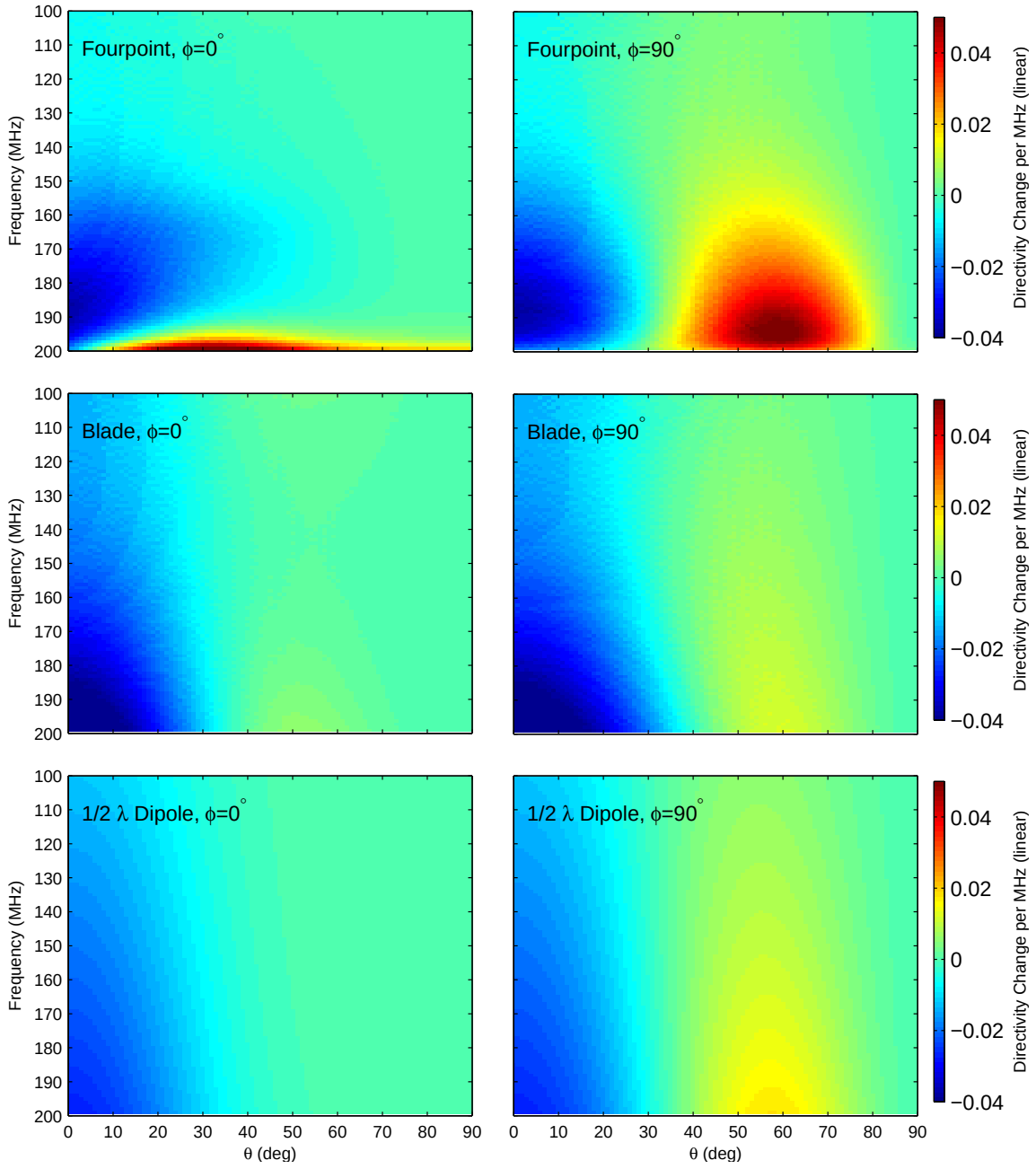

Figure 2.9: Derivatives of beam linear directivity values vs frequency at (left) ϕ=0° and (right) ϕ=90° for the (top) fourpoint, (middle) blade, (bottom) analytic $^1/_2$-λ wire dipole antennas. Viewing these plots can quickly identify problems with the antenna beam that typical beam plots (see Fig. 2.4) do not show. All antennas show a decrease near the zenith with increasing frequency consistent with the beginning of structure due to the ground plane. The fourpoint antenna shows greater magnitude changes and additional structure both at the zenith and in other locations compared to the other antennas, while the blade antenna is more similar to the analytic reference.

A slower reionization over 40 MHz is not detectable with any of our antennas when the foreground is fitted with a 6 term polynomial as the SNR is no greater than 1.7. When a five term polynomial is used the SNR increases and the detection is again favorable. The SNR for the blade antenna is between 4.6 and 6.7, between 3.4 and 4.0 for the fourpoint, and between 4.7 and 7.0 for the analytical dipole, again depending upon thermal noise. Based upon this analysis we conclude that the blade antenna using a five term polynomial with thermal noise averaged down to < 3 mK is capable of detecting or placing meaningful limits on the global 21 cm signal during reionization.

During antenna design the beam derivative with respect to frequency plot is a convenient tool to quickly assess the frequency structure in the beam and thus the ensuing effectiveness of foreground removal. This method can reveal problems quickly and requires little computing power.

Although we studied the frequency range 100 - 190 MHz, the results we have reported can be applied to other frequency ranges since the properties of an antenna scale linearly in wavelength with the physical size of the antenna. For example, global 21 cm experiments targeting the First Light signal between 50 and 100 MHz can also use these results by scaling the antenna design by a factor of two and halving the frequency. The FoM scales as $\nu^{-2.5}$.

A variety of non-dipole antenna designs have been considered for global 21 cm experiments, such as log-dipole and horn antennas. Most of these antennas have considerably more structure than simple dipole antennas and can be expected to exhibit even larger chromatic effects. Detailed investigation of other antennas is left for future work.

Acknowledgments

This work was supported by the NSF through research awards for the Experiment to Detect the Global EoR Signature (AST-0905990 and AST-1207761) and by NASA through Cooperative Agreements for the Lunar University Network for Astrophysics (NNA09DB30A) and the Nancy Grace Roman Technology Fellowship (NNX12AI17G). EDGES is located at the Murchison Radio-astronomy Observatory. We acknowledge the Wajarri Yamatji people as the traditional owners of the Observatory site.

Chapter 3

IMPROVED MEASUREMENT OF THE SPECTRAL INDEX OF THE DIFFUSE RADIO BACKGROUND BETWEEN 90 AND 190 MHZ

The material in this section is a reproduction of the published paper: "Improved Measurement of the Spectral Index of the Diffuse Radio Background Between 90 and 190 MHz," Mozdzen T. J., Bowman J.D., Monsalve R. A., Rogers A. E. E., 2017, MNRAS, 464, 4995.

The main results of the paper are 1) The spectral index of the diffuse radio sky is computed across the full range of LST hours as seen by a wide-field beam antenna located near the Murchison Radio-astronomy Observatory at $-26.7°$ $116°$ over a span of 240 nights; 2) The stability of the instrument's calibration is demonstrated over this period; and 3) the comparison of the measured spectral index compared against computed values using published sky models shows different levels of agreement.

3.1 Introduction

The low-frequency radio sky spectrum between 50 and 200 MHz is a key area of interest because experiments seeking to detect redshifted 21 cm radiation from neutral hydrogen gas during the Epoch of Reionization (EoR) and earlier eras of First Light and X-ray heating must subtract astrophysical foregrounds in these frequencies to high-precision. At these frequencies, the sky is mostly dominated by Galactic synchrotron radiation but also contains contributions from supernova remnants and extragalactic radio sources.

There are two approaches to detecting the redshifted 21 cm signal. The first approach is targeted by interferometeric arrays, such as the Murchison Widefield Array (MWA; Bowman et al. 2013; Tingay 2013), the Precision Array to Probe the Epoch of Reionization (PAPER; Ali 2015), the Hydrogen Epoch of Reionization Array (HERA; Pober et al. 2015), the Low-Frequency Array (LOFAR; van Haarlem et al. 2013), and the Low-frequency Aperture Array component of the Square Kilometer Array (SKA; Mellema et al. 2013). These arrays aim to measure spatial fluctuations in the sky brightness temperature on arcminute and degree scales resulting from variations in the density, ionisation, and temperature of the intergalactic medium (IGM) above redshift $z > 6$ (below 200 MHz).

The second approach, on the other hand, exploits the bulk properties of the high-redshift IGM that yield a global (monopole) contribution of redshifted 21 cm signal to the all-sky radio background. This approach is being pursued by the Experiment to Detect the Global EoR Signature (EDGES; Bowman, Rogers, & Hewitt 2008; Bowman & Rogers 2010b), Broadband Instrument for Global Hydrogen Reionisation Signal (BIGHORNS Sokolowski et al. 2015a), Sonda Cosmológica de las Islas para la Detección de Hidrógeno Neutro (SCI-HI Voytek et al. 2014), Large-aperture Experiment to detect the Dark Age (LEDA Bernardi, McQuinn, & Greenhill 2015), Shaped Antenna measurement of background Radio Spectrum (SARAS Patra et al. 2013; Singh et al. 2015), and the Dark Ages Radio Explorer (DARE; Burns et al. 2012). Both methods require careful and accurate subtraction of the sky foreground since the 21 cm signal is three to five orders of magnitude below the foreground.

Although observations of the low-frequency radio sky were among the earliest in radio astronomy (Turtle et al., 1962; Bridle, 1967), detailed knowledge of the spectral properties of diffuse emission remains lacking. The Haslam et al. (1981, 1982) all-sky map at 408 MHz, which was compiled from data taken in the 1960s and 1970s, is

still the cornerstone for foreground templates extrapolated across many frequencies in cosmic microwave background (CMB) and redshifted 21 cm analyses. Improvements to the map have occurred throughout the years, including efforts by Davies et al. (1996); Bennett et al. (2003a,b); Platania et al. (2003), and Remazeilles et al. (2015) that focused on removing point sources and destriping the original data. de Oliveira-Costa et al. (2008) combined the Haslam 408 MHz map and several other surveys between 10 MHz and 94 GHz to build a Global Sky Model (GSM), which provides spectral properties of the diffuse emission of the entire sky. In this model at 150 MHz, the spectral index outside the Galactic plane is ~ -2.6 and in the Galactic plane (in a narrow band) increases to ~ -2.5 with peaks as high as ~ -2.3. Both the Haslam map and the GSM have become widely used and cited in both simulations and data reduction pipelines for redshifted 21 cm observations (Bowman, Morales, & Hewitt, 2009; Patra et al., 2013; Subrahmanyan & Cowsik, 2013; Thyagarajan et al., 2015; Bernardi et al., 2016).

Guzmán et al. 2011 created an all-sky temperature map at 45 MHz based upon the surveys of Alverez et al. (1997) and Maeda et al. (1999). In addition, they produced an all-sky Galactic spectral index map based upon two frequency points by using their 45 MHz and the Haslam 408 MHz map after corrections for zero-level, extragalactic non-thermal emission, and CMB factors.

At higher frequencies, observations of Galactic radio emission between 3 and 90 GHz have been made by the Absolute Radiometer for Cosmology, Astrophysics, and Diffuse Emission I and II (ARCADE I and II) sky surveys (Fixsen et al., 2011; Kogut et al., 2011; Seiffert et al., 2011). This survey constrained models of extragalactic emission and suggested that models of electric dipole emission from spinning dust particles were a possible explanation for excess emission seen at 1 cm wavelengths. They find that, at most, three parameters (reference brightness temperature, spectral

index, and curvature) are necessary to model their wide-band data combined with external radio measurements between 22 MHz and 1.4 GHz, and from WMAP at 23 GHz (Kogut, 2012).

Recently, the new redshifted 21 cm arrays have begun yielding the first large, multi-spectral maps sensitive to diffuse structures in the low-frequency sky, including recent surveys by MWA GLEAM (Wayth et al., 2015) and LOFAR (Heald et al., 2015). GLEAM will scan the entire sky south of $\delta \sim +25^{\circ}$ between 72 and 231 MHz, and the LOFAR survey will scan 100 sq degrees in the northern sky centred on $(15^h, 69^{\circ})_{\rm J2000}$ between 30 and 160 MHz. The LOFAR survey's primary purpose is to enable automated processing by providing an *a priori* sky model, which also serves as an aid to foreground removal for EoR detection. Similarly, GLEAM's survey will serve a myriad of uses, one of which again will be foreground removal in EoR searches.

The EDGES instrument is able to provide a unique measurement of the absolute sky brightness temperature averaged over large spatial scales on the sky due to its wide beam. Rogers & Bowman (2008) found that the spectral index, $\beta_{100-200}$, of diffuse emission, defined as $T_{\rm sky} \propto \nu^{\beta}$, was -2.5 ± 0.1 at high-Galactic latitudes in the frequency range 100-200 MHz. Those measurements were taken using three days of data; two of which used a N-S orientation of the antenna's excitation axis and one with an E-W orientation. By combining their results with the Haslam sky map at 408 MHz, they were able to show that $\beta_{150-408} = -2.52 \pm 0.04$ at high Galactic latitudes.

In this paper we present new observations taken over a span of 240 nights from July 2015 through March 2016 with the latest version of the EDGES instrument that deploys an improved antenna with better chromatic performance and a new high-precision receiver calibration approach. These advancements enable us to improve on our earlier measurements of the spectral index of the diffuse low-frequency radio

emission and extend our coverage to all sidereal times at a constant declination of $-26.7°$.

The paper is organized in the following manner. In Section 2 we describe the instrument and calibration details. In Section 3 we present details of the data collected and chromatic beam corrections. Section 4 presents and discusses the spectral index results and comparisons to values predicted by relevant sky models.

3.2 EDGES Instrument

The EDGES experiment is deployed at the Murchison Radio-astronomy Observatory (MRO) in Western Australia (-26.7°, +116.6°). The experiment consists of two scaled-replica instruments spanning neighboring frequency bands of 50-100 MHz and 90-190 MHz. Each instrument consists of a single dipole-based antenna and receiver. Extensive modeling and simulation is performed on all instrument components, along with calibration measurements conducted both in the laboratory prior to instrument deployment and on site following deployment, in order to meet the low systematic instrumental error requirements for redshifted 21 cm observations (Rogers & Bowman, 2012). For the results reported here, we used the high-band instrument, hence we focus our discussion on that instrument. In this section, we review the instrument and the primary calibration steps.

3.2.1 Antenna and Receiver

The high-band instrument employs a single broadband "blade" dipole antenna sensitive to wavelengths in the range $3.3 \geq \lambda \geq 1.6$ m ($90 \leq \nu \leq 190$ MHz). The antenna is ground-based and zenith pointing. The antenna consists of two rectangular planar panels that are each 63×48 cm^2 and are placed 52 cm above a ground plane. The metallic ground plane is formed using a 5.35×5.35 m^2 aluminum plate

underneath the antenna, with four wire mesh extensions (each 2×5 m^2) that combine to form a "plus" shape. The antenna uses a Roberts Balun (Roberts, 1957) with a small shield at the bottom (Fig. 3.1). The blade antenna replaces the older "fourpoint" antenna design used in prior EDGES studies and yields better chromatic performance by introducing less spectral structure into the measurement (Mozdzen et al., 2016). The full width at half maximum beamwidth of the antenna at 150 MHz is 72° parallel to the axis of excitation and 110° perpendicular to the axis. The features of the antenna are summarized in Table 3.1.

The antenna is connected to a receiver placed underneath the ground plane in a temperature-regulated enclosure kept at 25°C. The receiver amplifies and conditions the signal before passing it through a 100 m cable to a backend unit that further amplifies it and sends it to a PC-based 14-bit 400-MS/s analog to digital converter (Fig. 3.2). Blocks of 65536 voltage samples are then Fourier transformed to obtain spectra of 32768 points below 200 MHz with 6.1 kHz resolution.

3.2.2 Calibration and Corrections

The receiver utilizes laboratory calibration prior to deployment, augmented with a three-position hot/cold/antenna calibration switching scheme for stability in the frontend during operation, to achieve an absolute accuracy of $\leq 0.1\%$ in measured antenna temperature (Monsalve et al., 2016). The calibration quantities are measured as a function of both temperature and frequency. The impedance match of the antenna can be measured *in situ* by switching a Vector Network Analyzer (VNA) into the electrical path.

To propagate the calibration to the sky temperature measurement, we must apply several corrections for losses that occur in the antenna before the receiver. The losses include ground plane loss, balun loss, and antenna panel loss. We also make an

Table 3.1: Blade Antenna Features (refer to Fig. 3.1)

Parameter	Value
3 dB Beamwidth ϕ= 0° at 150 MHz	72°
3 dB Beamwidth ϕ=90° at 150 MHz	110°
Height above ground plane	52 cm
Panel Width	63 cm
Panel Length	48 cm
Solid ground plane	5.35×5.35 m^2
Mesh ground plane extensions	2×5 m^2

estimate and correct for the actual temperature of the low-noise amplifier (LNA) which may deviate from the nominal 25°C due to temperature gradients.

Ground plane loss originates from our finite ground plane, allowing a small amount of signal ($\leq$ 1%) from below the horizon to be received from the antenna. These losses are modeled through CST (Computer Simulation Technology) Microwave Studio and through FEKO (FEldberechnung für Köper mit beliebiger Oberfläche) E&M simulations. The balun loss is due to minor resistive impedance in the brass and copper-plated balun hardware and also to the resistivity and dielectric properties of the connector to the receiver. This effect is estimated from analytical models. Finally, losses in the antenna panels are due to finite conductivity and estimated with FEKO. Adjustments are made to the measured spectrum to counteract these effects in processing.

Figure 3.1: Photograph of the high-band blade antenna with fiberglass support tubes and a tuning capacitor on the top of the panels between the balun tubes to improve impedance matching. Surrounding the balun tubes at the base, a short rectangular enclosure shields against vertical currents in the tubes.

3.3 Data and Processing

We measured the sky temperature using EDGES over a period of 240 days starting with day 207 (July 26) of 2015. We determined the spectral index by fitting the calibrated data to the two parameter equation

$$T_{\rm sky} = T_{150} \left(\frac{\nu}{\nu_0} \right)^{+\beta} + T_{\rm CMB}, \tag{3.1}$$

where the two fitting parameters, β and T_{150}, are the spectral index and the brightness temperature at 150 MHz less $T_{\rm CMB}$, respectively. The CMB temperature, $T_{\rm CMB}$, is

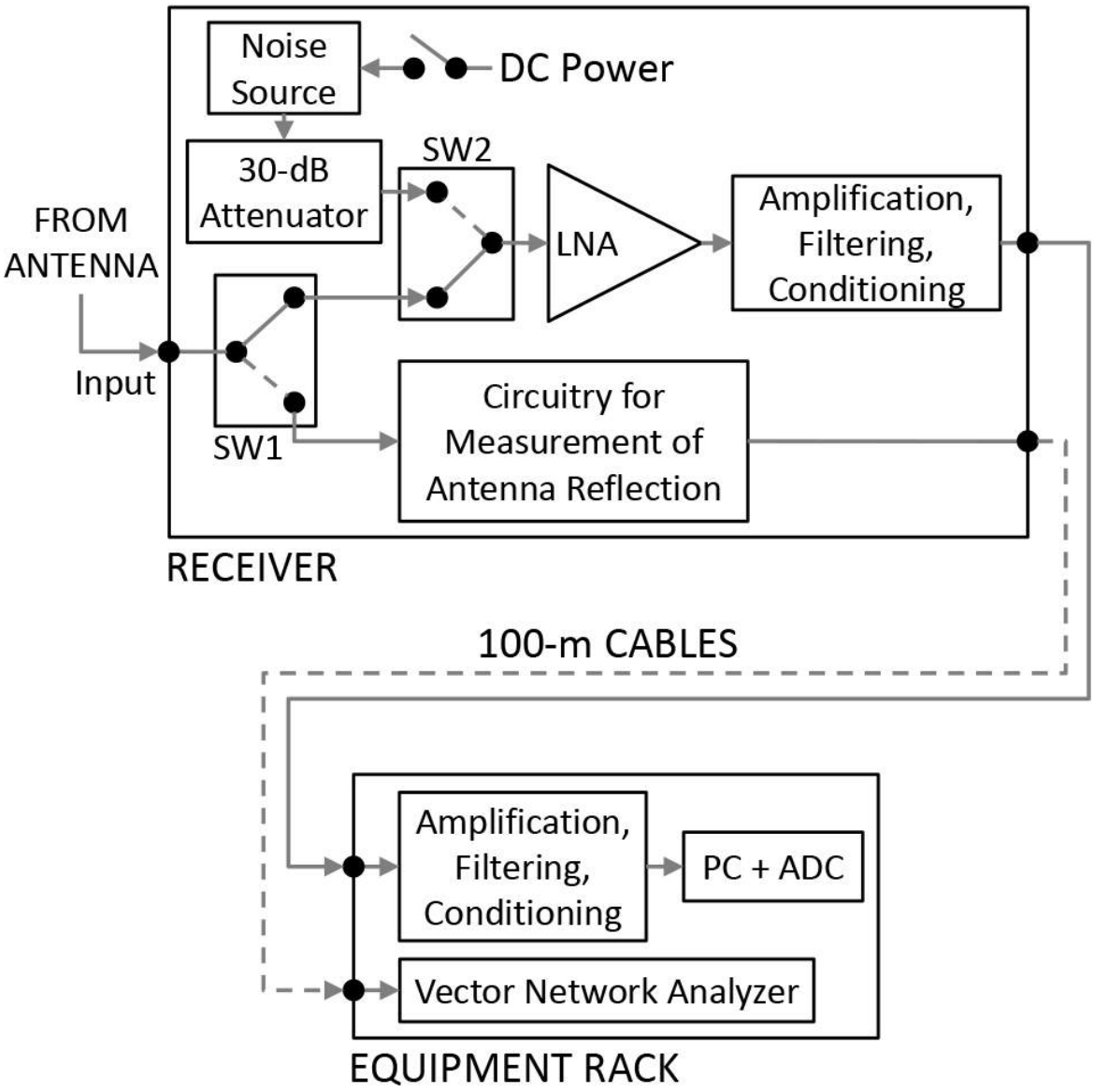

Figure 3.2: Block diagram of the EDGES instrument

2.725 K, and ν_0 is 150 MHz. We find that this equation yields lower RMS fitting errors than the log form of the equation:

$$\ln(T_{\rm sky} - T_{\rm CMB}) = \ln(T_{150}) + \beta \ln\left(\frac{\nu}{\nu_0}\right). \tag{3.2}$$

Data collection was occasionally interrupted due to a variety of factors such as power outages and inclement weather (Table 3.2). We exclude daytime data since effects from the Sun and the ionosphere (Rogers et al., 2015) can interfere with the observation of the astronomical sky foreground. Sporadic data points affected by radio-frequency interference (RFI) are flagged and excised. The data are averaged and binned into 72 timeslots of 20 minutes in LST and into 250 frequency bins of 400 kHz from 90 to 190 MHz.

For an antenna on the surface of the Earth pointed toward zenith, the pointing declination of its primary axis corresponds to the latitude of the antenna's deployment site, and the pointing right ascension corresponds to the LST at the site. As the earth rotates, the antenna pointing changes direction, altering the mapping of its beam pattern onto sky coordinates. Because the antenna's beamwidth is wide by design, we sample the average sky temperature weighted by the beam (see Figs. 3.3 - 3.4).

At low frequencies, the Earth's ionosphere can distort the appearance of the astronomical sky and, in principle, provide an additional chromatic effect. Vedantham et al. (2014) used the LOFAR low frequency antenna beam to evaluate the chromatic effects of the ionosphere, in particular due to refraction. To minimize these effects, we restrict our data analysis to times when ionospheric perturbations are minimal by excluding data when the Sun's elevation is -10° or higher.

Table 3.2: Days of omitted data between day 207 of 2015 and day 82 of 2016. Out of 240 observing days, 29 days did not capture usable nighttime data.

Day Numbers	Year	Span
208 to 209	2015	2
212 to 214		3
244		1
246 to 249		4
263 to 264		2
290		1
342		1
303 to 309		7
20 to 26	2016	7
54	2016	1
Total Days		29

3.3.1 Adjustment for Beam Chromaticity

In the context of measurements of the sky spectrum, an ideal antenna beam would be independent of frequency. However, as shown in Bernardi, McQuinn, & Greenhill (2015); Mozdzen et al. (2016), realistic antennas suffer chromatic (frequency-dependent) effects that couple angular structure in the sky to spectral structure in the measurement. Thus, before we can analyze the spectral properties of the radio sky to high-precision, we must correct for the chromatic effects of the EDGES antenna.

Fig. 3.3 shows a snapshot of the beam's directivity at 150 MHz projected upon the Haslam sky map when located at -26.7 latitude and pointed towards the zenith at LST = 13 h. When the directivity of the beam changes at other frequencies, affected locations in the sky will contribute stronger or weaker to the antenna temperature.

These chromatic beam effects are significant especially with the Galactic Centre overhead where the RMS fitting errors to a two parameter equation can exceed 9 K for an uncorrected spectrum. Rogers & Bowman (2008) chose to report the spectral index using a region in the sky which would minimize chromatic beam effects and chose LST = 2.5 h. Fig. 3.4 shows that this is true for the present blade beam, but even in this region, beam effects must be taken into account. Compared to other antenna choices, we have significantly reduced this effect by using the blade design, which has the benefits of minimal chromaticity and is conducive to precision beam modeling through simulations (Mozdzen et al., 2016).

To further reduce the chromatic beam effect in measured spectra, we use simulated beam maps, along with a sky model, to generate a chromaticity correction factor for the beam, which can reduce the RMS fitting errors to under 5 K. We model the antenna from 90 to 190 MHz in steps of 1 MHz with numerical time-domain electromagnetic simulations using CST Microwave Studio. We then use these beam models, along with the Haslam 408 MHz map, to compute a correction factor as a function of frequency for each LST in our observations. To scale the Haslam map from 408 MHz to our frequency range, we first subtract the $T_{\rm CMB}$ temperature from the map, scale its brightness temperature to 150 MHz using a constant spectral index of $\beta = -2.5$ and then add $T_{\rm CMB}$ back in. We convolve the scaled Haslam map with the beam directivity at each frequency modeled. The beam factor ratio is formed by dividing the modeled antenna temperature at each frequency by the antenna temperature at 150 MHz. We implicitly assume that the spectral index does not vary significantly from its value at 150 MHz in our frequency range of 90 to 190 MHz. The beam correction factor is given by:

$$B_{\rm factor}(\nu) = \frac{\int_\Omega T_{\rm sky}(\nu_{150}, \Omega) B(\nu, \Omega) {\rm d}\Omega}{\int_\Omega T_{\rm sky}(\nu_{150}, \Omega) B(\nu_{150}, \Omega) {\rm d}\Omega}, \tag{3.3}$$

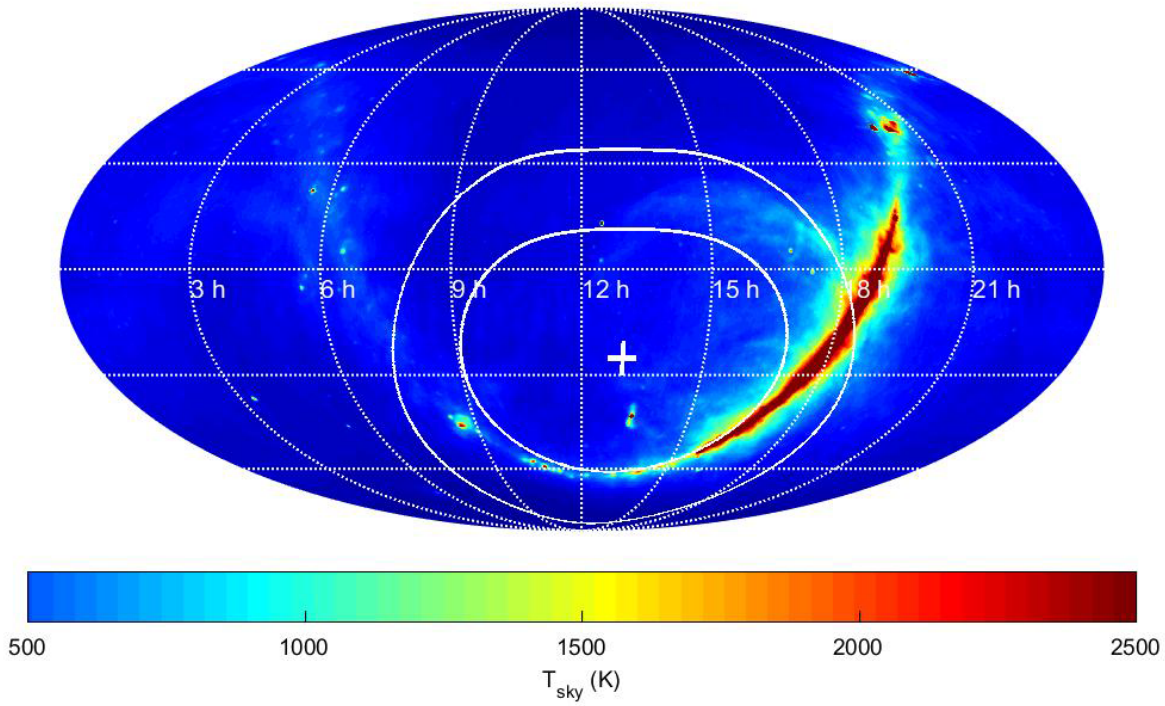

Figure 3.3: The EDGES beam at -3 and -10 dB projected onto the Haslam Sky map scaled to 150 MHz in celestial coordinates when located at -26.7° latitude with the zenith at 13 h LST. The beam is purposefully wide to capture the sky averaged global EoR signal.

where

$$T_{\rm sky}(\nu_{150},\Omega) = [T_{\rm Haslam}(\Omega) - T_{\rm CMB}] \left(\frac{150}{408}\right)^{-2.5} + T_{\rm CMB}, \tag{3.4}$$

$B(\nu,\Omega)$ is the beam directivity, $T_{\rm Haslam}(\Omega)$ is the Haslam sky map, $T_{\rm CMB}$ is 2.725 K, and ν is the frequency. This ratio is the chromatic beam factor that we apply to the measured spectrum as a divisor to counteract the under or over response to the sky. We repeat this for all 72 time steps in LST to form a two-dimensional beam factor array (see Fig. 3.5).

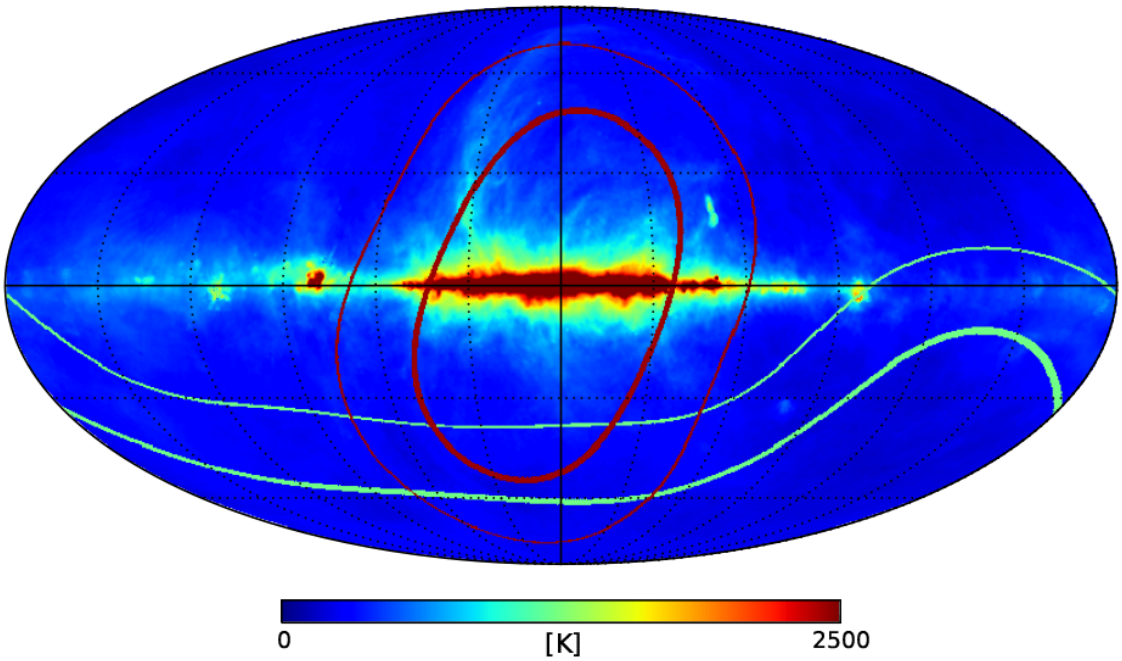

Figure 3.4: The EDGES beam at -3 and -10 dB projected onto the Haslam Sky map scaled to 150 MHz in galactic coordinates when located at -26.7° latitude shown for LST values of 18 h and 2.5 h (dark trace and light blue trace respectively). The beam at 18 h LST captures much of the central region the Galactic plane, which is high in spatial structure, while at 2.5 h it captures mostly structureless sky, minimizing chromatic beam effects.

3.4 Results

3.4.1 Spectral Index

From day number 207 in 2015 to day 82 in 2016, data were fit separately per day for each LST interval. The parameters T_{150}, β, and the RMS error to the fit were extracted using equation (3.1). The spectra were fit for the two cases of using or not using beam chromaticity correction.

The values of T_{150}, β, and the RMS error show excellent stability over time as can be seen in the waterfall plots of Figs. 3.6-3.7 and confirmed by the low standard devi-

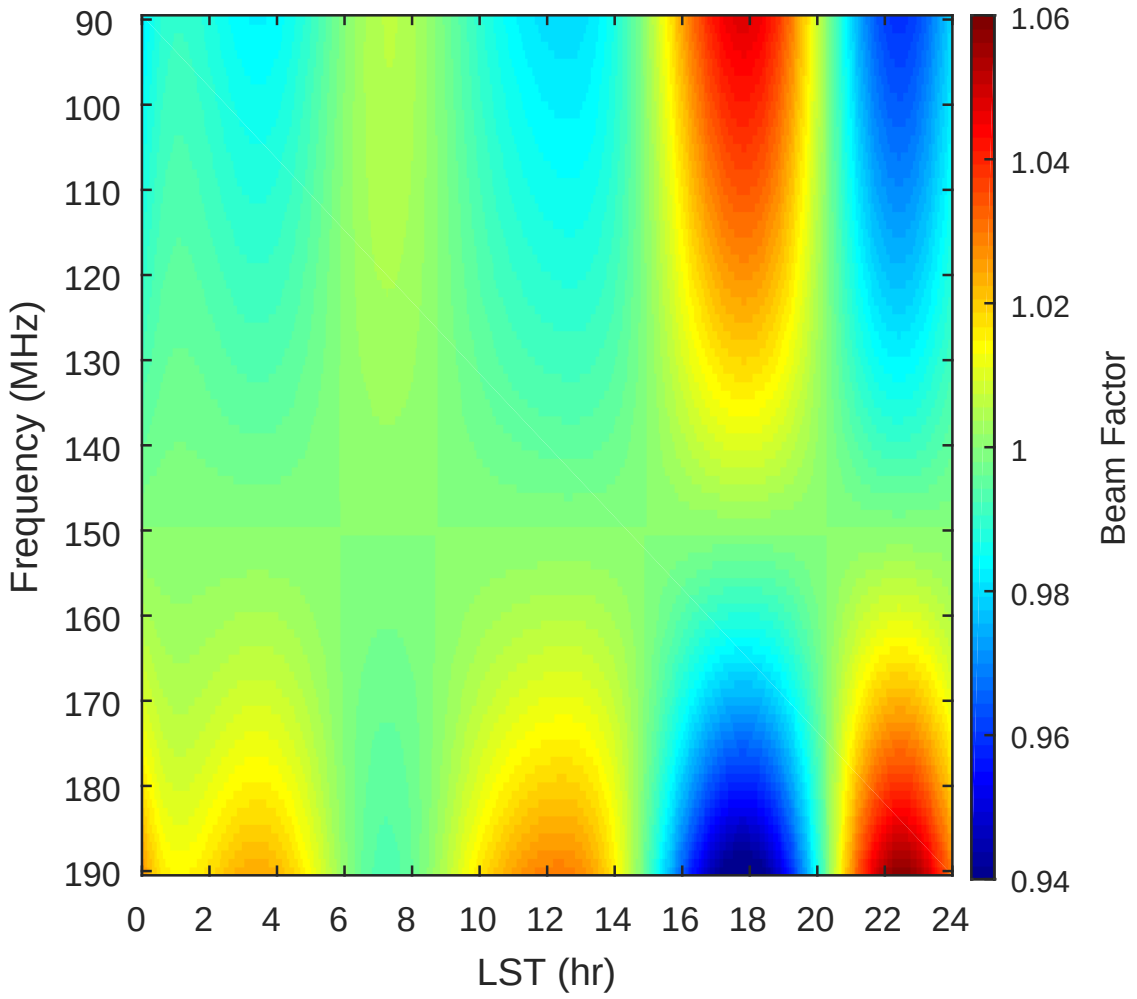

Figure 3.5: Simulated beam chromatic correction factor for the EDGES blade antenna. For a given LST, the beam factor is created by dividing the simulated convolution of the chromatic beam with the sky at 150 MHz, by the simulated convolution of both the beam and the sky at 150 MHz. This ratio gives the amount of over or under antenna temperature as compared to the antenna temperature if the beam were not chromatic and had a directivity pattern of the beam at 150 MHz. The magnitude of the beam factor is greatest when there is angular structure in the sky as is the case near LST 18 h when the Galaxy is overhead.

ation in data scatter as seen in the β and T_{150} averages of Fig. 3.8, where $\sigma_\beta < 0.003$ and $\sigma_{T_{150}} < 5$ K. T_{150} is also insensitive to beam chromaticity as the average beam corrected and uncorrected values differ by no more than 0.2% due to the low chromaticity of the blade beam. The daytime data (Sun above $-10°$ elevation) are not shown, yielding the blank band in the plot.

The importance of including the beam correction factor is most apparent in the average β plot of Fig. 3.8. With the correction applied, we find $-2.60 > \beta > -2.62$ for LST values between 0 and 12 h. Between 12 and 24 h it features a flattening that peaks at -2.50 at 17.7 h. It is clear in Fig. 3.8 that beam correction has a significant impact on the recovered spectral index. Without correction, the beam effects mask the flattening that is expected near the Galactic Centre (de Oliveira-Costa et al., 2008; Guzmán et al., 2011).

We also investigated fitting the spectra to a three parameter model, adding γ as a third term

$$\ln(T_{\rm sky} - T_{\rm CMB}) = \ln(T_{150}) + \beta \ln\left(\frac{\nu}{\nu_0}\right) + \gamma\left[\ln\left(\frac{\nu}{\nu_0}\right)\right]^2. \tag{3.5}$$

Although the RMS fitting errors were smaller and $|\gamma|$ was typically relatively small, < 0.1, we conservatively assume that the uncertainty on gamma due to systematic effects dominates fitted values. Hence, we save further three parameter analysis to future work.

3.4.2 Systematic Error Estimation

We evaluate and correct for sources of systematic errors to the calibration process: LNA temperature gradients, ground loss, antenna loss, and beam correction uncertainty. We maintain the receiver at 25°C with forced airflow and active cooling/heating, but the temperature of the LNA's electronic components may differ

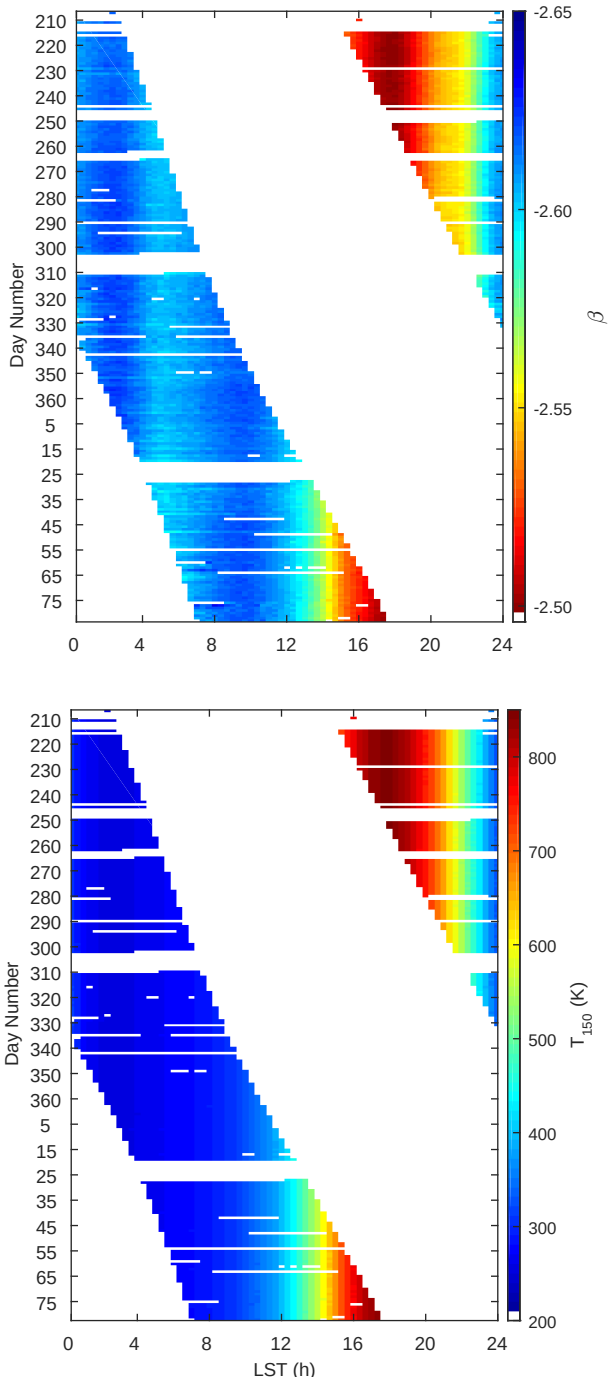

Figure 3.6: Waterfall graphs of (top) the spectral index β and (bottom) the sky temperature at ν_0=150 MHz, T_{150}. RFI and other spurious signals were purged from the spectra before performing a fit to equation 3.1. The data were binned into 400 kHz wide bins from 90 to 190 MHz and the beam adjustment factor was applied. Both the β and the T_{150} graphs show excellent stability from day to day as the data collection ran for 240 days from day 207 2015 to day 82 2016.

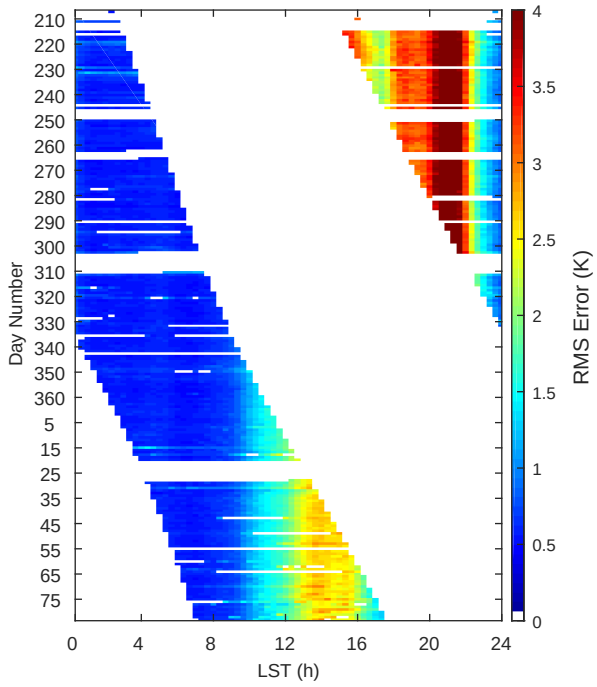

Figure 3.7: Waterfall graph of the RMS fitting error to equation (3.1). RFI and other spurious signals were purged from the spectra before performing the fit. The data were binned into 400 kHz wide bins from 90 to 190 MHz and the beam adjustment factor was applied. The RMS error also shows excellent stability from day to day as the data collection ran for 240 days from day 207 2015 to day 82 2016.

slightly from the reading at the main temperature sensor. A second sensor is used to capture potential gradients, which remain below 1°C during operation. This temperature difference has a small effect on the calibration values that are used to adjust the antenna spectrum. Simulations showed the impact on β to be no more than 0.005 if we did not include the adjustment.

In the field, we use a 5.35 $\times$ 5.35 m^2 solid metallic ground plane made from a central square of solid aluminum augmented by 2 $\times$ 5 m^2 sheets of wire mesh. The imperfect ground of the earth serves as the ground plane where there is no metal. Given the limited size of the metal ground plane, a small fraction of the antenna beam will pickup the temperature of the ground. The effect of the finite ground

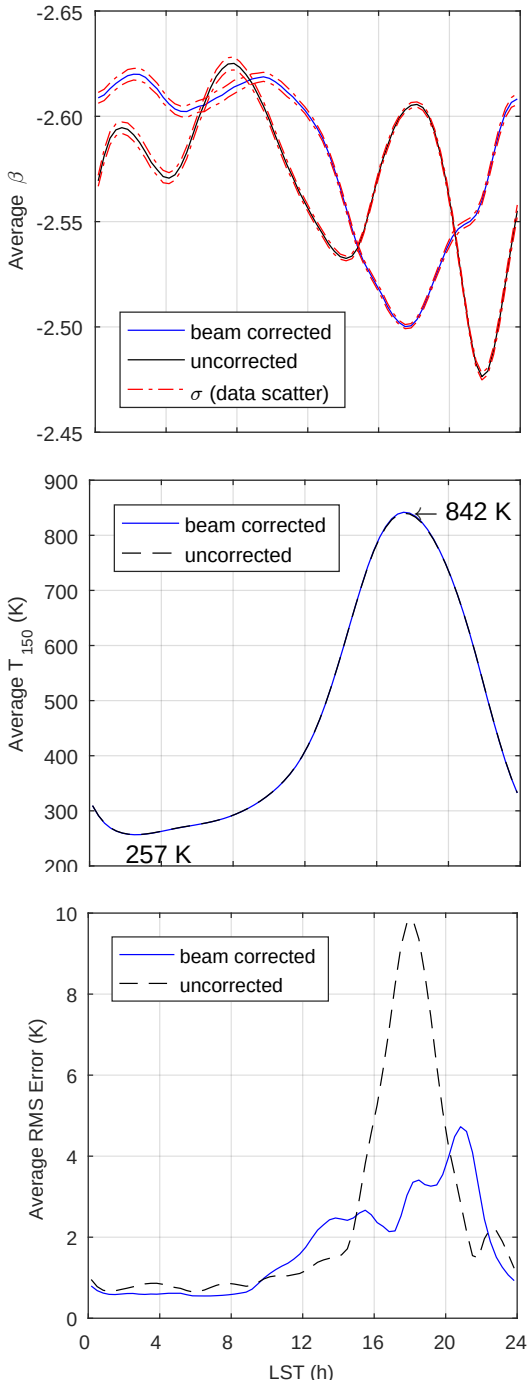

Figure 3.8: Averages of β, T_{150}, and RMS error for each LST value taken over days for which nighttime data was available. Averages are shown for the processing done with and without beam correction. Beam correction reveals the dip in β near the Galactic Centre, where the variations of β without beam correction are dominated by the chromatic beam effects. The small data scatter in β further confirms the uniformity from day to day seen in the waterfall graphs. T_{150} min and max values, 257 K and 842 K, are annotated on the chart.

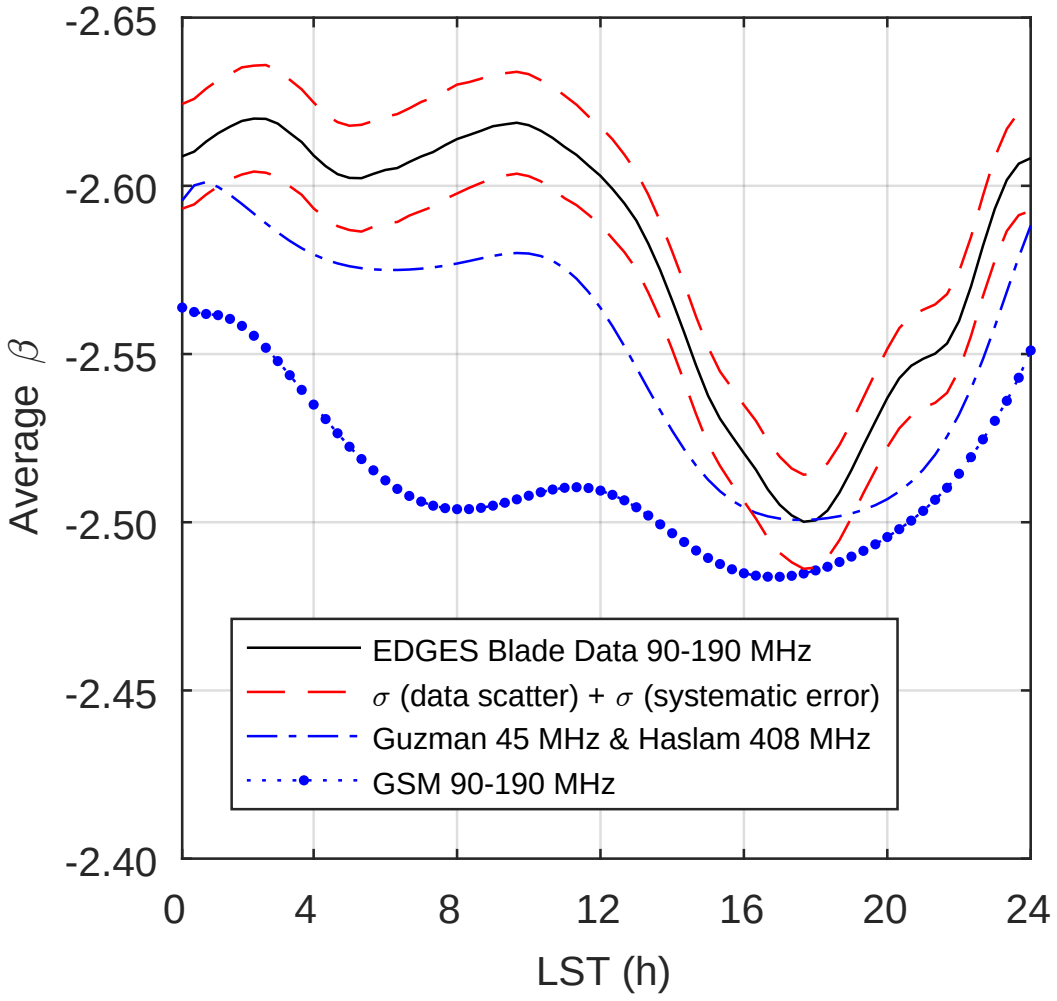

Figure 3.9: Spectral index derived from EDGES measurements including the total one-sigma uncertainty, which consists of 0.012 for systematic uncertainty and the LST dependent data scatter. Also plotted are the simulated spectral index results when using the GSM between 90 and 190 MHz and by the combination of the Guzmán (45 MHz) and Haslam (408 MHz) maps. The two simulated spectral index curves show similar structure in β as compared to the measurement derived curve, but the Guzmán curve matches the measured data more closely.

plane on ground pickup/loss was simulated in FEKO and CST. In FEKO we used a Greens function to implement a finite ground plane modeled over the soil. We used values for the dielectric constant of 3.5 and conductivity of 0.02 S/m because they are based upon the soil measurements made at the MRO for dry conditions reported by Sutinjo et al. (2015). In CST we modeled the finite ground plane as a finite sheet in free space. Both simulations resulted in losses $< 1.0\%$ but with opposite frequency dependence trends. CST results varied between 0.4 and 1.0%, with the larger loss at lower frequencies, while FEKO varied between 0.2 and 1.0% with larger loss at high frequencies. The effects are small in both cases and, considering the simulation uncertainties, it is not clear which model is more appropriate. Hence, we took the approximate average of the two simulations as a constant 0.5% loss, indepdendent of frequency. Correcting for 0.5% frequency-independent ground loss caused β to become more positive by up to 0.003 for 0 h $<$ LST $<$ 12 h and become more positive by 0.003-0.006 for 12 h $<$ LST $<$ 24 h as compared to no ground loss correction.

The antenna losses arise from the balun resistance, the connection to the receiver, and the resistance of the antenna panels. The balun of the EDGES system includes two brass tubes (outer diameter 0.5") with a copper-plated brass rod running up one of the tubes and a teflon-dielectric connector to the receiver. When we account for the impedance in the balun structure and its connection to the receiver in the calibration process (parameters obtained via transmission line models and lab measurements), we see an effect on β no greater than 0.015. There is a very minor effect on β from the panel resistance of 0.001.

When we use CST and FEKO to compute the beam correction factor, the difference in the spectral index between methods is 0.016. This considers different choices of including or subtracting the CMB as well as different scalings of the Haslam 408 MHz map to 150 MHz assuming realistic spectral indices. To assess the impact of spatial

variations in the spectral index on our beam correction factor, we used the frequency dependent GSM instead of the spatially flat scaled Haslam map. The results show that the GSM-derived beam correction factor differs from our default method by 0.3% at most. The effect upon the spectral index causes a difference of ±0.003 for all LST values except from 20 to 23 h where it rises to +0.005. Hence, the main component of chromaticity originates from the beam and not spectral index spatial variations.

We now combine the sources of systematic uncertainty. If we assume our adjustments have a standard error of half of the magnitude of the effect (with vs. without or method 1 vs method 2), and combine the sources of system error in quadrature: temperature gradients 0.005, finite ground plane effects 0.006; antenna balun 0.015; finite panel resistance 0.001; and beam correction factor 0.016, we arrive at a systematic uncertainty on β of $0.023/2 = 0.012$. Adding the maximum data scatter value of 0.003 directly to the systematic uncertainty, as opposed to in quadrature, the total maximum uncertainty in β becomes 0.015. Based on this value we conservatively report a total one-sigma uncertainty of $\sigma_{\beta_{\text{Total}}} = 0.02$. This uncertainty improves upon the uncertainties reported in Rogers & Bowman (2008) of $\sigma_{\beta_{100\text{-}200}} = 0.1$ considering only EDGES data and $\sigma_{\beta_{150\text{-}408}} = 0.04$ when including Haslam skymap data. Additionally, we measure data over a significantly longer time period and include the LST dependence of the spectral index. The final measurement with the full uncertainty range is shown in Fig. 3.9.

3.4.3 Simulated Spectral Index From Sky Maps

We compare our measured results for the spectral index to simulated results by using publicly available sky maps: the de Oliveira-Costa GSM; the Haslam 408 MHz map; and the Guzmán 45 MHz map. We simulate the antenna temperature that EDGES is expected to observe using the GSM from 90 to 190 MHz in steps of 1 MHz

as a function of LST, by convolving the sky model (less $T_{\rm CMB}$) with the simulated EDGES blade beam (fixed at 150 MHz to compare to the beam-corrected measurements). We then fit the simulated antenna temperature to equation (3.1) to obtain the spectral index vs. LST. Because the Haslam and Guzmán sky maps are only available at 408 MHz and 45 MHz, respectively, we calculate the spectral index with the closed form expression

$$\beta = \ln\left(\frac{T_{\rm ant}^{'}(\nu_{45})}{T_{\rm ant}^{'}(\nu_{408})}\right) \Big/ \ln\left(\frac{\nu_{45}}{\nu_{408}}\right), \tag{3.6}$$

where $T_{\rm ant}^{'}(\nu)$ is

$$T_{\rm ant}^{'}(\nu) = \int_{\Omega} T_{\rm sky}^{'}(\nu,\Omega) B(\nu_{150},\Omega) {\rm d}\Omega, \tag{3.7}$$

$B(\nu_{150},\Omega)$ is the achromatic beam for a given pointing and orientation, ν is frequency, and $T_{\rm sky}^{'}(\nu,\Omega)$ is the sky model in use. $B(\nu_{150},\Omega)$ is normalized to a unit integral at each frequency. In this manner, we generate spectral index values across 24 hours of LST. The results of these two simulations along with our result from measured data are shown in Fig. 3.9.

We find that the GSM-derived spectral indices tend to over-predict (GSM less negative) the spectral index of the observations at high-Galactic latitudes (low LST). The GSM-derived spectral indices differ from our measurements by $0.05 < \Delta_\beta = \beta_{\rm GSM} - \beta_{\rm EDGES} < 0.12$ (3 to 7.5 sigma) away from the Galactic Centre and $\Delta_\beta = 0.01$ (1 sigma) near the centre. The Guzmán-Haslam (GH) derived spectral indices, on the other hand, are a closer match. The GH indices only differ from our measurements by $0.01 < \Delta_\beta < 0.05$ (1 to 3 sigma) away from the Galactic Centre and agree well at 18 h LST. One possible cause for the better agreement to the data by the GH model compared to the GSM is the higher sky temperatures reported in the Guzmán map as compared to the GSM at 45 MHz. Away from the Galactic Centre, the Guzmán map is 1100 K higher than the GSM in much of the sky. If the GSM had higher

temperatures away from the Galactic Centre, the simulated spectral index using the GSM maps would decrease for the lower values of LST, giving better agreement with our measurements. Based on these results, we caution that the GSM likely underpredicts the sky temperature at high-Galactic latitudes below 200 MHz.

If we make a direct comparison against Rogers & Bowman (2008) where their EDGES-only spectral index result was -2.5 ± 0.1 at LST = 2.5 h, we report -2.62 ± 0.02, which is consistent with the 2008 results. To compare against their $\beta_{150-408}$ value, we must use our T_{150} measurement values at LST = 2.5 h coupled with the T_{408} values as computed using the Haslam sky map with our antenna beam. In this case, we compute $\beta_{150-408} = -2.63 \pm 0.01$ as compared to their result of $\beta_{150-408} = -2.52 \pm 0.04$. The disagreement in these two values arise from differences in T_{408} and T_{150} values. T_{408} values differ by 0.7 K, which is most likely due to different antenna beam models in use (due to different antenna designs) and results in 33 % of the disagreement. T_{150} values differ by twice the 2008 stated uncertainty in T_{150} ($\sigma_{T_{150}} = 10$ K), which we believe is due to accuracy of the Rogers & Bowman (2008) measurement and accounts for the remainder of the difference.

3.5 Conclusion

We measured the sky brightness temperature as a function of frequency and derived the spectral index β as a function of sidereal time by fitting to a two parameter model over a span of 240 days using 211 days of nighttime data acquired from July 2015 to March 2016. Instrument calibration, including corrections for temperature gradients, ground loss, antenna losses, and beam chromaticity, has been applied to deliver instrument stability of over several months as demonstrated by spectral index standard deviation values $\sigma_\beta < 0.003$.

We have presented results of extensive measurements of the diffuse radio sky between the frequencies of 90-190 MHz. We find that the spectral index β is in the range $-2.60 > \beta > -2.62 \pm 0.02$ in the lower LST values, but increases to -2.50 with the Galaxy overhead. The GSM tends to over-predict the strength of the variation in the spectral index in the range $0.05 < \Delta_\beta < 0.12$ for low LST. However, comparison with the spectral index as computed using the Guzmán sky map at 45 MHz and the Haslam Sky map at 408 MHz is a closer match and differs by $0.01 < \Delta_\beta < 0.05$ away from the centre. At the Galactic Centre both models agree with our measurements of the spectral index to within one sigma.

Future work is planned to investigate the criteria needed to fit to a three-parameter spectral equation. Updates to sky models will be used to simulate spectral index across LST using the EDGES blade antenna. We also plan to measure the spectral index in the $50 - 100$ MHz range with the low-band EDGES blade antenna.

Acknowledgments

The authors would like to thank Adam Beardsley for useful inputs and discussions. This work was supported by the NSF through research awards for the Experiment to Detect the Global EoR Signature (AST-0905990 and AST-1207761) and by NASA through Cooperative Agreements for the Lunar University Network for Astrophysics (NNA09DB30A) and the Nancy Grace Roman Technology Fellowship (NNX12AI17G). Raul Monsalve acknowledges support from the NASA Ames Research Center (NNX16AF59G). EDGES is located at the Murchison Radio-astronomy Observatory. We acknowledge the Wajarri Yamatji people as the traditional owners of the Observatory site. We thank CSIRO for providing site infrastructure and support.

Chapter 4

RESULTS FROM EDGES HIGH-BAND: 2. TEST OF THE COSMIC REIONIZATION ON COMPUTERS (CROC) STRUCTURE FORMATION SIMULATION

The main finding in this paper is that the reionization model postulated by Kaurov & Gnedin (2016) is not compatible (significance metric of 1.9σ) with the EDGES highband data collected on 40 nights of observing at its location near the Murchison Radio-Astronomy Observatory (-26.7° S). If the model were shifted 5 MHz to lower frequencies, we would not be able to claim incompatibility.

4.1 Introduction

The Experiment to Detect the Global EoR Signature (EDGES) instrument has improved from its earliest deployment in both the quantity of data collected and in its accuracy. The initial EDGES based constraints placed on the global redshifted 21 cm signal reported by (Bowman, Rogers, & Hewitt, 2008; Bowman & Rogers, 2010b) were based upon a previously used calibration scheme. Due to recently improved calibration methods developed in Rogers & Bowman (2012); Monsalve et al. (2017a) we have improved our measurement of the spectral index of the diffuse radio background to now cover the entire sky and with more accuracy (Mozdzen et al., 2017) than previous EDGES measurements (Rogers & Bowman, 2008). The enhanced performance of the EDGES instrument also makes it possible to evaluate various cosmological model scenarios with measured data in the highband range of $90 \leq \nu \leq 190$ MHz. In Monsalve et al. (2017b) we are able to consider constraints on the general model features

of Gaussian absorption troughs and hyperbolic tangent emission in $T_{\rm b}$. EDGES has recently expanded its frequency sensitivity range by installing two lowband systems ($50 \leq \nu \leq 100$ MHz) which will increase the confidence levels of model rejections or detections. This paper will focus solely on highband data.

In addition to the EDGES project, other global redshifted 21 cm teams, operating in several frequency bands, are now reporting their results and are able to estimate the likelihood of specific features in the shape of $T_{\rm b}$. SCH-HI operates in the range $60 - 88$ MHz and has collected data with 4.4 h of integration time over a 2 week period (Voytek et al., 2014). LEDA is also a lower band system ($40 \leq \nu \leq 85$ MHz) and has collected 19 minutes of effective data over a two night period (Bernardi et al., 2016). SARAS2 operates in the highband range of $110 \leq \nu \leq 200$ MHz and has collected data over a 4 h period (Singh et al., 2017). Work continues with the DARE program to observe from the backside of the moon (Burns et al., 2012, 2017).

The redshifted global 21 cm signal, $T_{\rm b}$, can be used as a probe of the history of the IGM due to the complex interactions between the neutral hydrogen gas of the IGM, the 21 cm spin temperature, the CMB, and X-ray and UV heating. Details of these interactions and the effect upon $T_{\rm b}$ is well covered by Madau, Meiksin, & Rees (1997); Barkana & Loeb (2001); Gnedin & Shaver (2004); Furlanetto (2006); Pritchard & Loeb (2008, 2012); Mesinger, Ferrara, & Spiegel (2013); Kaurov & Gnedin (2016). The salient features of $T_{\rm b}$, pertinent to the residuals of the EDGES data after subtracting the diffuse foreground and the CMB, are a Gaussian shaped absorption trough, usually at $z \geq 15$, and an emission phase beginning near $z = 13$ that decays to zero by $z = 6$.

In this paper we analyze EDGES highband data with the goal of detecting the $T_{\rm b}$ model developed in the the Cosmic Reionization on Computers (CROC) structure formation simulation by Kaurov & Gnedin (2016), which we will refer to as the KG

model. The EDGES data consists of 40 nights (defined by the Sun's declination being lower than $-10°$) of highband data collected from day numbers 250 through 289 (2015) ($0.6 \leq \text{LST} \leq 6.6$ h), which represent over 30 h of integration time on the sky after filtering and data cuts.

In Section 4.2, we describe the the EDGES instrument and data, CROC model, the fitting, and the compatibility criteria and metrics. In Section 4.3, we discuss the results of the data fitting, the compatibility metric, and their implications. We then summarize our findings and conclusions in Section 4.4.

4.2 Methodology

In this section we briefly describe the EDGES instrument, the data collected, the KG model, and the model fitting strategy to search for the model within the measured data.

4.2.1 EDGES Instrument and Data

The EDGES highband system consists of a blade antenna ($90 \leq \nu \leq 190$ MHz) and a receiver which is calibrated in the lab over the temperature range of 15 °C to 35 °C. In the field the receiver is maintained at 25 °C with active temperature control. The antenna is located in a radio-quiet environment in Western Australia at the Murchison Radio-astronomy Observatory (MRO) (Bowman & Rogers, 2010a; Offringa et al., 2015). The system is described in greater detail in Monsalve et al. (2017a); Mozdzen et al. (2016); Monsalve et al. (2017b).

The data was collected in 2015 over a period of 40 nights from day numbers 250 through 289 (Sept 7 to Oct 26, 2015). Nighttime was defined as the time when the Sun's declination was lower than $-10°$, and the corresponding viewable nighttime LST range was $0.26 \leq \text{LST} \leq 4.5$ h on day 250 with it gradually extending to

$0.26 \leq \mathrm{LST} \leq 6.6$ h by the last day of operation. As can be seen in Mozdzen et al. (2017), the diffuse foreground was very steady in this region.

The raw data was processed in several steps as described in Monsalve et al. (2017b), which we recount here for convenience. The first phase processed the data in units of one day, keeping daily results separate. First, the spectra of each 39 s data set was calibrated and then averaged with all of the spectra for that day. Then, the average daily spectra were placed into 390.6 kHz wide frequency bins (64 6.1 kHz channels combined into one bin). Excision of RFI and inclement weather disturbances was done both before and after binning and on small and large time scales (from 39 s to 6 h).

Then we remove the foreground individually from each of the 40 daily averages using a five term polynomial

$$T_{\mathrm{fg}}(\nu) = \sum_{i=0}^{4} a_i \nu^{i-2.5} \tag{4.1}$$

The resulting average fitting error of the 40 individual days is 56 mK. Next, we average all days into one spectrum and repeat the binning and RFI and inclement weather anomalous spectra excision as before. This results in a spectrum with an RMS fitting error of only 17 mK (see Fig.4.2). Comparing the channel to channel differences above 108 MHz tells us that the RMS of the thermal noise is 6 mK and slightly higher below 108 MHz due to the increased RFI excision. The total effective integration time of this master spectrum is more than 30 h. It is speculated that the 20 MHz sinusoidal feature in the residuals, whose magnitude decreases with frequency, is the result of the impedance mismatch between the antenna and the receiver, but future studies are needed to confirm this hypothesis.

4.2.2 Brief Overview of The Kaurov - Gnedin (KG) Global Redshifted 21 cm Brightness Temperature Model

The computation model presented in Kaurov & Gnedin (2016) is developed with two simulation sets: three 40 h^{-1} Mpc runs and one 80 h^{-1} Mpc run to create a grid of 21 cm brightness temperatures at each simulation snapshot (2D sky $\times$ 1D frequency). The Cosmic Reionization on Computers (CROC) simulations include full 3D radiative transfer effects, which create data points of the spatially and temporally resolved radiation spectrum, from which $T_{\rm b}(z)$ can be computed. The KG $T_{\rm b}(z)$ model we use in this paper is the variation Kaurov & Gnedin (2016) describe as the Self-consistent model, which is characterized by a very shallow negative pre-reionization absorption dip of 18.4 mK (z=11.7) and an EoR emission peak of 17.8 mK (z=8.5).

The peak values are relatively low compared to other models and imply that a detection maybe harder than previous thought. The absorption trough is shallower and occurs later than in other models such as Pritchard & Loeb (2008, 2012) but consistent with the previous results of Gnedin & Shaver (2004). The higher accuracy CROC simulations were rerun to validate their earlier result and these new simulations. The findings were that the interaction between the coupling of the Lyα background radiation to the gas temperature and the CMB and the heating by X-rays is confirmed as stated in Pritchard & Loeb (2008), and that the difference between their studies is in the assumptions of the timing and strength of the two factors. In Kaurov & Gnedin (2016), the resulting global redshifted 21 cm EoR model is the product of their most accurate and most realistic set of assumptions. This is the model we analyze in this paper.

We search for the presence of the self consistent KG model in our calibrated measured data by fitting the data to a 5 term polynomial, whose purpose is to remove

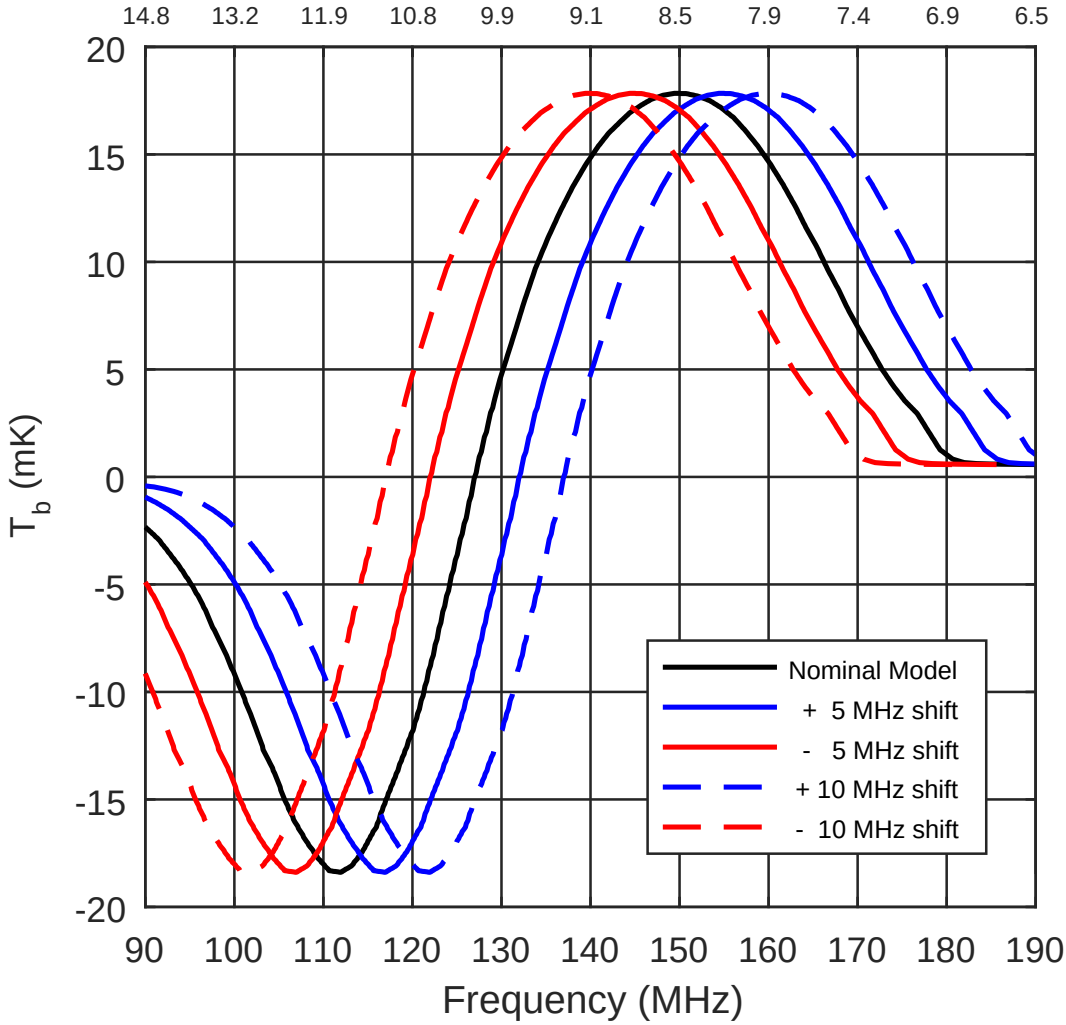

Figure 4.1: The Kaurov-Gnedin EoR model with frequency shift variations. The nominal model is the black line and the model extrema are 17.8 mK and -18.4 mK

the diffuse radio foreground, and a normalized function that represents the KG model. We analyze the model exactly as given to us, but we also explore sensitivity to small shifts of the model in frequency space (see Fig. 4.1).

4.2.3 Data Fitting and Metrics

After subtracting the constant $T_{\rm CMB}$ term (2.725 K) from the calibrated EDGES highband antenna temperature data to a 5 term power-law polynomial and the EoR model term given by:

$$T_{\rm ant}(\nu) = \sum_{i=0}^{N-1} a_i \left(\frac{\nu}{\nu_0}\right)^{i+\beta} + \ A_{21} \cdot KG^{\rm model}_{\rm normed}(\nu) \tag{4.2}$$

$$KG^{\rm model}_{\rm normed}(\nu) = KG^{\rm model}(\nu)/{\rm Max}(KG^{\rm model}(\nu)) \tag{4.3}$$

where ν ranges from 90 to 190 MHz, $\nu_0 = 150$ MHz, $\beta = -2.60$ is the spectral index, ${\rm Max}(KG^{\rm model}(\nu)) \ = \ 17.8$ mK, and A_{21} is the fitting coefficient of the EoR term. This equation (without the EoR term) was introduced in Mozdzen et al. (2016) as an efficient way to subtract the sky foreground. Typical residuals (RMS fitting error ~ 17 mK) and the KG model are shown in Fig. 4.2.

We introduce the model scaling parameter $T_{\rm ref}$

$$KG^{\rm model}_{\rm scaled}(\nu) = T_{\rm ref} \cdot KG^{\rm model}_{\rm normed}(\nu) \tag{4.4}$$

so that we can analyze hypothetical scenarios where the magnitude of the KG model can vary. In the standard KG model $T_{\rm ref} = 17.8$ mK. To declare a model incompatible with the data at a significance of 1σ, the fitting parameter, A_{21}, must be different from the model peak, $T_{\rm ref}$, by $1\sigma_{21}$. The criteria and metric for incompatibility are summarized as:

$$1\sigma \text{ incompatibility:} \qquad A_{21} + 1\sigma_{21} \ < \ T_{\rm ref} \ < \ A_{21} - 1\sigma_{21} \tag{4.5}$$

$$2\sigma \text{ incompatibility:} \qquad A_{21} + 2\sigma_{21} \ < \ T_{\rm ref} \ < \ A_{21} - 2\sigma_{21} \tag{4.6}$$

$$\text{Significance Metric:} \qquad \left| \frac{T_{\rm ref} - A_{21}}{\sigma_{21}} \right| \tag{4.7}$$

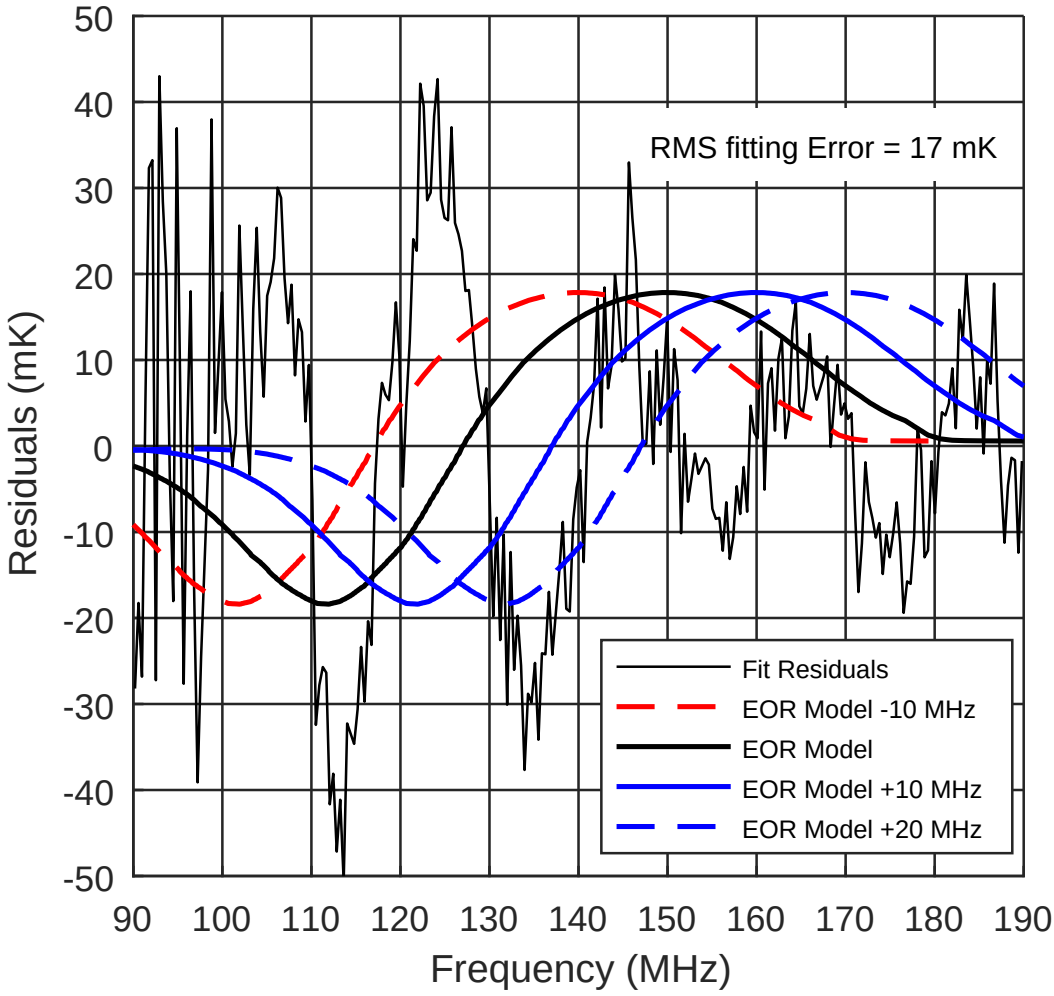

Figure 4.2: Residuals to a 5 term polynomial with a constant $T_{\rm CMB}$ term and the normalized KG model. The RMS error to the is 17 mK. Also shown is the KG EoR model with two versions shifted ± 10 MHz in frequency.

Note that T_{ref} does not affect any of the fitting parameters because the normalized KG model is used in the fitting equation and A_{21} reflects the amount of the model recovered by the fitting. T_{ref} is used after fitting is complete to determine the fraction of the KG model recovered and the significance of an incompatibility claim. However, the fitting parameters, σ_{21} and A_{21}, will be affected when we modify the lower and upper frequency ranges of the fitting equation or shift the KG model higher or lower in frequency. These changes will have an effect upon the significance metric.

4.3 Results

4.3.1 Nominal KG Model Fitting

Using Eq. 4.2 with the full range of data from 90 to 190 MHz without shifting the KG model, we obtain the results shown in Table 4.1 and graphed in Fig. 4.3. We find that the nominal KG model is not compatible with the measured data with a significance metric of 1.9. The peak value of the KG model would have to be below 13 mK to reduce the compatibility metric below 1σ. By modifying the range of fitting we see only moderate effects except for the case of eliminating the lower 10 MHz of the fit (100-190 MHz). The data in the lowest 10 MHz is thus quite important to the fitting as the standard deviation of the A_{21} term becomes quite large without including this data. We conclude that it is best to use the full range of data in the analysis.

4.3.2 KG Model Frequency Shifted

In addition to modifying the fitting range, we shifted the KG model in frequency from -20 to +20 MHz to investigate sensitivities to small model offsets in frequency. The results of the fittings are tabulated in Table 4.2 and shown graphically in Fig. 4.4.

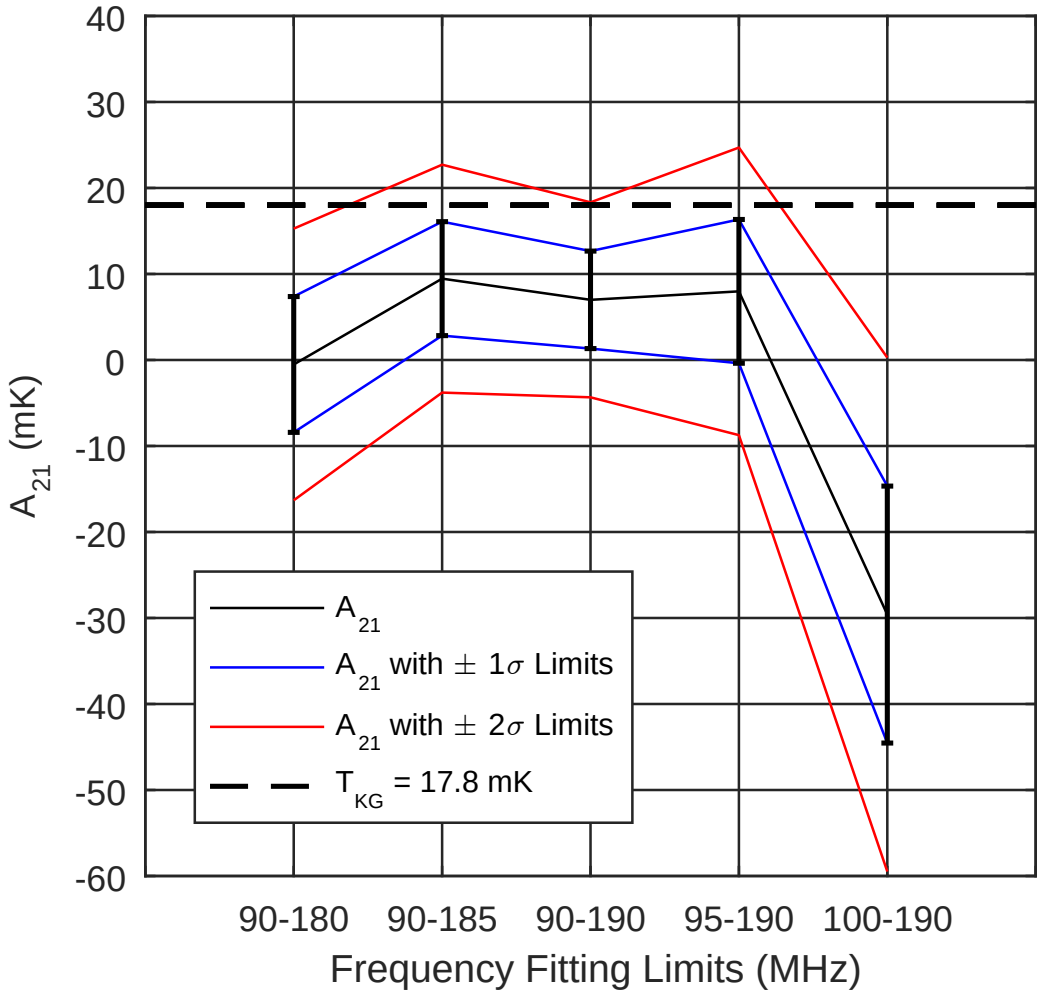

Figure 4.3: Fitting results with varied frequency limits. The dashed reference temperature of the KG model is plotted along with the values $A_{21} + \sigma_{21}$ and $A_{21} + 2\sigma_{21}$. The blue lines outline a region that would be judged to be incompatible by a metric value of less than 1σ were the EoR model to have a T_{ref} value inside this boundary, while the red lines outline the 2σ region. We see that the T_{KG} model is near the 2σ for most of the scenarios simulated.

Table 4.1: Fitting Results for different fitting ranges. The values $A_{21} + \sigma_{21}$ and $A_{21} + 2\sigma_{21}$ are the $T_{\rm ref}$ values required for the EoR model to be incompatible at the 1σ and 2σ significance levels respectively (see Eq. 4.7).

Fit Range (MHz)	A_{21} (mK)	σ_{21} (mK)	$A_{21} + \sigma_{21}$ (mK)	$A_{21} + 2\sigma_{21}$ (mK)
90-180	-0.5	7.9	7.4	15.0
90-185	9.5	6.6	16.0	23.0
90-190	7.0	5.7	13.0	18.0[a]
95-190	8.0	8.4	16.0	25.0
100-190	-30.0	15.0	-15.0	0.3

[a]Nominal Kaurov-Gnedin EoR model

Fig. 4.4 shows the results of the fitting and the ranges for a 1σ or 2σ level incompatibility metric. Qualitatively, the KG model becomes more incompatible when shifted to higher frequencies, up to +20 MHz, but becomes more compatible if shifted to lower frequencies down to -5 MHz. At a shift of -10 MHz, the recovered model coefficient becomes higher than it should, which again makes it incompatible for recovering more of the signal than should be present. At a negative frequency shift of -5 MHz, the model is most compatible with the measured data.

It is possible that the KG EoR model is partially fitting to the sinusoidal feature in the residuals. In order to lower the magnitude of the residuals and subsequently obtain a lower covariance on the fitting parameter a_{21}, the foreground has to be subtracted more cleanly. Future studies are needed to determine the best method to eliminate the sinusoidal structure.

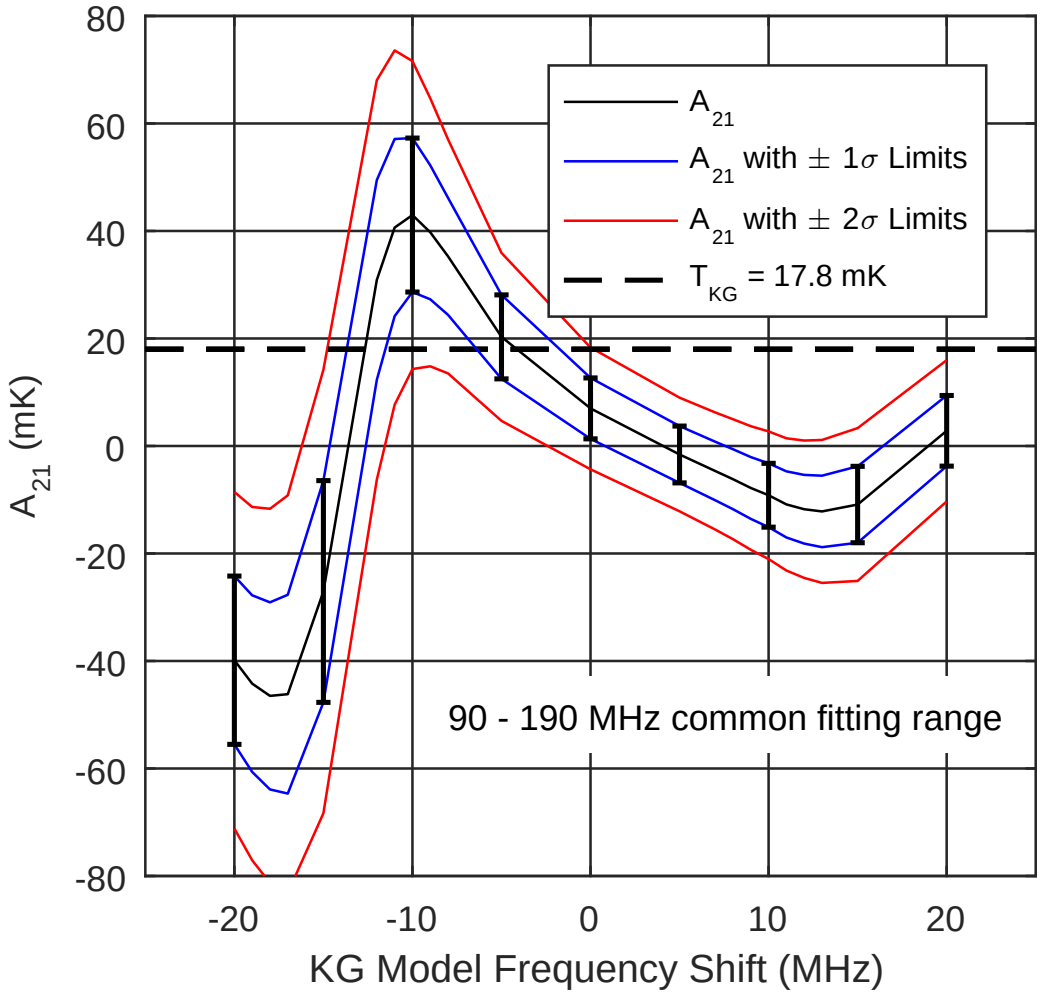

Figure 4.4: The KG model becomes more incompatible when shifted to higher frequencies, up to +20 MHz, but becomes more compatible if shifted to lower frequencies down to -5 MHz. At a shift of -10 MHz, the recovered model coefficient becomes higher than it should, which again makes it incompatible for a different reason. At a negative frequency shift of -5 MHz, the model is most compatible with the measured data.

Table 4.2: Fitting Results for different EoR model frequency shifts. The values $A_{21} + \sigma_{21}$ and $A_{21} + 2\sigma_{21}$ are the $T_{\rm ref}$ values required for the EoR model to be incompatible at the 1σ and 2σ significance levels respectively (see Eq. 4.7). In this case, the KG model intersects the regions between $\pm 1\sigma$ near negative frequency shifts of -5 MHz and -12 MHz, weakening the claim of incompatibility in these regions.

Fit Range (MHz)	A_{21} (mK)	σ_{21} (mK)	$A_{21} + \sigma_{21}$ (mK)	$A_{21} + 2\sigma_{21}$ (mK)
-20	-40.0	16.0	-24.0	-8.5
-15	-27.0	21.0	-6.4	14.0
-10	43.0	14.0	57.0	72.0
-5	20.0	7.8	28.0	36.0
0	7.0	5.7	13.0	18.0[a]
5	-1.6	5.3	3.7	9.0
10	-9.2	5.9	-3.2	2.7
15	-11.0	7.1	-3.8	3.3
20	2.8	6.6	9.4	16.0

[a]Nominal Kaurov-Gnedin EoR model

4.4 Conclusions

We conclude that the Kaurov-Gnedin CROC global redshifted 21 cm cosmology model is not consistent with the data at the 1.9σ significance level. Clipping the frequency range of the fitting had a minimal effect, with the noted exception of excluding the lowest frequency decade of data ($90 - 100$ MHz) which caused the standard deviation to increase significantly while the fitting coefficient on the KG model became large and negative (-29 mK). This emphasizes the importance of the full data range, and suggests that data even lower than 90 MHz should be collected and added to the data set. EDGES has a low band ($50 - 100$ MHz) instrument

deployed in the field and data collection is underway, but should be included in future analysis.

Shifting the frequency range in a positive direction made it more unlikely that the model is contained in the data, while a small negative shift of -5 MHz had the lowest incompatibility metric of any fitting at 0.3σ. We conclude that this is a very difficult model to firmly claim incompatibility due to its low peak values. We put constraints on the possibility that the model might be located at higher or lower frequencies, with the conclusion that it could in the future shift to slightly lower frequencies without disagreeing with the EDGES measured data, but that shifts positive would increasing become more unlikely. Elimination of the sinusoidal feature of the residuals would increase the confidence of model rejections and is a task for future investigations. The lowest frequency decade is very important as the fitting is more stable when this data is included, and that future work should incorporate data below 90 MHz from the EDGES lowband instruments.

4.5 Acknowledgments

We thank Alexander Kaurov and Nickolay Gnedin for use of their model for the global redshifted 21 cm signal which was developed in their CROC project.

This work was supported by the NSF through research awards for the Experiment to Detect the Global EoR Signature (AST-0905990 and AST-1207761) and by NASA through Cooperative Agreements for the Lunar University Network for Astrophysics (NNA09DB30A) and the Nancy Grace Roman Technology Fellowship (NNX12AI17G). Raul Monsalve acknowledges support from the NASA Ames Research Center (NNX16AF59G). EDGES is located at the Murchison Radio-astronomy Observatory. We acknowledge the Wajarri Yamatji people as the traditional owners of the Observatory site. We thank CSIRO for providing site infrastructure and support.

Chapter 5

CONCLUSION

The first focus area of the EDGES project at Arizona State University was to reduce systematic errors in the instrument, which meant we had to first identify the sources of variations and uncertainties, quantify them, and reduce as many of these sources of errors as possible. There were many signs that EDGES was pushing the envelope of accuracy that most other projects ignore. One example was the need to make the reflection coefficient of the antenna stable to within 0.01 dB with a nominal level of -20 dB. This in turn required knowledge of the DC resistance of the VNA calibration match standard to within 0.01 ohms and to know its value as a function of temperature. The stability of the coax cable, which connects the antenna to the VNA, became an issue too, because the dielectric constant of teflon has hysteresis with a critical temperature point near 22 °C (Czuba & Sikora, 2011). The solution to the cable problem was to bury it underground where the temperature doesn't fluctuate as much. Thus began our efforts to address various sources of error in the instrument. The first focus area of this thesis was to address the error introduced by the chromaticity of the EDGES antenna's beam pattern.

5.1 Chromatic Beams in Global 21 cm Measurements

In Mozdzen et al. (2016) we evaluated two dipole-based antennas used by EDGES and one idealized reference antenna to assess the effects of frequency-dependent beam shapes on the ability to remove the foreground from global redshifted 21 cm measurements and detect the redshifted global 21 cm signal. Across the full latitude-LST

space we found that the fourpoint antenna produced sub 10 mK Figure of Merit (FoM) values in 3% and 12% of the locations for foreground fits using polynomials with 5 and 6 terms respectively, while the FoM values of the blade antenna were below 10 mK in over 99% of the locations for both fits. Furthermore, FoM values of foreground fitting for the blade antenna were below 1 mK in 25 % and 72 % of the locations for 5 and 6 term fits respectively. We note that the optimum choice of E-W or N-S excitation axis orientation depends upon specific deployment location as one orientation was not always better than the other. The fourpoint antenna is only suitable at a few restricted locations on the sky using a 5 or 6 term fit, while the blade antenna provides adequate FoM performance across the entire sky when using a 5 or 6 term polynomial to remove the foreground.

In our simulations, a narrow 21 cm signal corresponding to a rapid reionization over 20 MHz was detectable for all antennas assuming 3 mK of thermal noise. The SNR values indicate detection is favorable for either a 5 or 6 term foreground removal fit. For a 5 term fit, the SNR values of the blade and analytical dipole are similar, ranging from 12 to 18, and the fourpoint values range between 7.8 and 8.8. For a 6 term fit, the SNR values of the blade and analytical dipole are the same ranging from 7 to 11, and the fourpoint values range between 5.3 and 6.4 depending upon the thermal noise.

A slower reionization over 40 MHz is not detectable with any of our antennas when the foreground is fitted with a 6 term polynomial as the SNR is no greater than 1.7. When a five term polynomial is used the SNR increases and the detection is again favorable. The SNR for the blade antenna is between 4.6 and 6.7, between 3.4 and 4.0 for the fourpoint, and between 4.7 and 7.0 for the analytical dipole, again depending upon thermal noise. Based upon this analysis we conclude that the blade antenna, using a five term polynomial with thermal noise averaged down to < 3 mK,

is capable of detecting or placing meaningful limits on the global 21 cm signal during reionization.

A variety of non-dipole antenna designs have been considered for global 21 cm experiments, such as log-dipole and horn antennas. Most of these antennas have considerably more structure than simple dipole antennas and can be expected to exhibit even larger chromatic effects. During the antenna design phase the beam derivative with respect to frequency plot is a convenient tool to quickly assess the frequency structure in the beam and thus the ensuing effectiveness of foreground removal.

5.2 Spectral Index Measurements with EDGES

In Mozdzen et al. (2017) we measured the sky brightness temperature as a function of frequency and derived the spectral index β as a function of sidereal time by fitting the data to a two parameter model over a span of 240 days using 211 days of nighttime data acquired from July 2015 to March 2016. Instrument calibration, including corrections for temperature gradients, ground loss, antenna losses, and beam chromaticity, was applied to deliver instrument stability over several months as demonstrated by spectral index standard deviation values $\sigma_\beta < 0.003$.

We presented results of extensive measurements of the diffuse radio sky in the frequency range of 90 to 190 MHz and found that the spectral index β is in the range $-2.60 > \beta > -2.62 \pm 0.02$ in the lower LST values, but it increases to -2.50 with the Galaxy overhead. The Global Sky Model of de Oliveira-Costa et al. (2008) tends to over-predict the strength of the variation in the spectral index in the range $0.05 < \Delta_\beta < 0.12$ for low LST. However, comparison with the spectral index as computed using the Guzmán et al. (2011) sky map at 45 MHz and the Haslam Sky map at 408 MHz is a closer match and differs by $0.01 < \Delta_\beta < 0.05$ away from

the center. At the Galactic Center both models agree with our measurements of the spectral index to within one sigma.

5.3 Results From the EDGES Highband Instrument: 2

In Chapter 4, we concluded that the Kaurov-Gnedin CROC global redshifted 21 cm cosmology model is not consistent with our measured data at the 1.9σ significance level. Trimming the frequency range of the fitting had a minimal effect, with the noted exception of excluding the lowest frequency decade of data ($90-100$ MHz), which caused the standard deviation to increase significantly and the fitting coefficient on the KG model became large and negative (-29 mK). This emphasizes the importance of the full data range, and suggests that data even lower than 90 MHz should be collected and added to the data set. EDGES has a low band ($50-100$ MHz) instrument deployed in the field and data collection is underway, which will be included in future analysis.

Shifting the frequency range in a positive direction made it more unlikely that the model is contained in the data, while a small negative shift of -5 MHz had the lowest incompatibility metric of any fitting at 0.3σ. We conclude that the model is just at the threshold of EDGES's ability to constrain. We also put constraints on the possibility that the model might be located at higher or lower frequencies, with the conclusion that it could in the future shift to slightly lower frequencies without disagreeing with the EDGES measured data, but that shifts positive would increasingly become more unlikely. Again, the lowest frequency decade is very important as the fitting is more stable when this data is included, and that future work should incorporate data below 90 MHz from the EDGES lowband instruments.

5.4 Next Steps

5.4.1 Improvements for a More Accurate Spectral Index Measurement

Although the reflection coefficient of the receiver and the ambient calibration load appear to be the largest single sources of systematic error, there are still areas of improvement to the antenna design that would be helpful. The simulated beam correction factor could be better estimated if the ground plane was larger and a more accurate sky map was used in the frequency range of 50 to 200 MHz. A ground plane twice the size of the one in place today for the highband antenna would remove the difficult task of simulating a finite ground plane with soil (composed of uncertain parameters) continuing where the ground plane stops. The infinite ground plane simulation would be closer to reality and the systematic error from ground loss would become insignificant.

Improved versions of the global sky map have been made (Liu & Parsons, 2016; Zheng et al., 2017) and should be used to refine the beam correction factor. With more accurate and detailed sky maps, the uncertainty in the beam correction along with the improved ground plane should reduce the correction factor uncertainty from 0.016 to 0.008. Lower resistance balun components would also be helpful by plating the balun tubes either silver or gold. Assuming the balun loss, the ground loss, and the beam correction uncertainties were able to be reduced by a factor of two, the spectral index uncertainty would decrease from σ=0.016 to 0.009. Spectral index measurements should also be made in the lowband range with the data that is now being collected. Lowband measurements would benefit from the enhancements discussed for the highband instrument.

5.4.2 *Improvements to EoR Model Rejections with the Highband Instrument*

The Kaurov-Gnedin EoR model evaluation resulted in EoR model fitting parameters of $a_{21} = 7.0$ and $\sigma_{21} = 5.7$, which indicated a 1.9σ rejection significance. After fitting to a five term polynomial, the residuals contained a 20 MHz sinusoidal component that decreased in amplitude with increasing frequency and a fitting RMS error of 17 mK. It is possible that some portions of the KG model were fitting to these residuals. To obtain a lower fitting covariance value, the magnitude of the residuals need to be lower. At this point, it is speculated that the residuals are the result of the impedance mismatch between the antenna and the receiver, but future studies are needed to reduce the residuals and lower the covariance of the model fitting parameter, a_{21}. This would enable higher confidence level rejections of EoR models with low peak emission values such as the KG model.

5.4.3 *Focus Shift to the Lowband for EoR Signature Detection*

The most promising and detectable global 21 cm feature is the Cosmic Dawn absorption trough, where the majority of EoR models place it in the range $13 > z > 30$ (50 to 100 MHz). The peak value of this feature is predicted to be at least as great as the EoR emission signal if not possibly 100s of mK. This part of the spectrum is more difficult to access due to increased Galactic synchrotron foreground levels, which are higher by a factor of $2^{2.6} \sim 6$. All of the highband improvements should be applied here such as larger ground planes, lower balun losses, more accurate beam correction factors, and a modified ambient hot calibration load with a better impedance match to the receiver input. In addition to these improvements, multiple lowband antennas should be deployed with EW and NS excitation axis directions as well as one or two redundant installations to confirm EoR signature detections.

REFERENCES

Ali Z. S. et al., 2015, ApJ, 809, 61

Alvarez H., Aparici J., May J., Olmos F., 1997, A&A, 124, 315

Balanis C. A., 2005, Antenna Theory, John Wiley & Sons, Inc., Hoboken, NJ

Barkana R., Loeb A., 2001, PhR, 349, 125

Bennett C. L. et al., 2003, ApJS, 148, 1

Bennett C. L. et al., 2003, ApJS, 148, 97

Bennett C. L. et al., 2013, ApJS, 208, 2

Bernardi G., McQuinn M., Greenhill L. J., 2015, ApJ, 799, 90

Bernardi G. et al., 2016, MNRAS, 461, 3, 2847

Bolton J. S. et al. 2011, MNRAS, 416, L70

Bouwens R. J., 2015, ApJ, 811, 140

Bowman J. D., Rogers A. E. E., Hewitt J., 2008, ApJ, 676, 1

Bowman J. D., Morales M. F., Hewitt J., 2009, ApJ, 695, 183

Bowman J. D., Rogers A. E. E., 2010, RFI Mitigation Workshop, 30

Bowman J. D., Rogers A. E. E., 2010, Nature, 468, 796

Bowman J. D. et al., 2013 PASA 30, e031

Bridle A. H., 1967, MNRAS, 136, 219

Bromm V., 2004, ASPC, 42, 79

Bromm V., Larson R. B., 2004, Annu. Rev. Astron. Astrophys., 42, 79118

Bromm V., Loeb A., 2003, ApJ., 596, 3446

Burns J. et al., 2012, Advances in Space Research, 49.3, 433

Burns J. O. et al., 2017, arXiv:1704.02651

Chiang H. C. et al 2017, internal report, PRIZM

Chornock R. et al. 2013, ApJ, 774, 26

Cohen A., Fialkov A., Barkana R., Lotem M., 2017, ArXiv e-prints, arXiv:1609.02312

Computer Simulation Technology, 2010, White paper on understanding time domain meshing in CST Microwave Studio

Czuba K., Sikora D., 2011, ACTA Phys. Pol. A, 119, 553.

Datta A., Bradley R, Burns J. O., Harker G., Komjathy A., Lazio T. J. W., 2015, ApJ, 831, 6

Davies R. D., Watson R. A., Gutierrez C. M., 1996, MNRAS, 278, 925

de Oliveira-Costa A., Tegmark M., Gaensler B. M., Jonas J., Landecker T. L., Reich, P., 2008, MNRAS, 388, 247

Dunlop J. S., 2013, in Astrophysics and Space Science Library, ed. T. Wiklind, B. Mobasher, V. Bromm (Astrophysics and Space Science Library, Vol. 396; Berlin: Springer), 223

Fan X. et al., 2004, AJ, 128, 515

Fan X., Carilli C. L., Keating B., 2006, Annu. Rev. Astron. Astrophys., 44, 415

Fan X. et al., 2006, AJ, 132, 117

Field G., 1958, Proc. J. R. E. 46 240

Fixsen D. J. et al., 2011, ApJ, 734, 5

Furlanetto S. R., 2006, MNRAS, 371, 867

Furlanetto S. R., Oh P. S., Briggs F. H., 2006, PhR, 433 181

George E. M. et al., 2015, ApJ, 799 177

Gnedin, N. Y., Shaver, P.A., 2004, ApJ, 608, 611

Gnedin, N. Y., 2014, ApJ, 793, 29

Gnedin, N. Y., Kaurov, A. A., 2014, ApJ, 793, 30

Greenhill L. J., Bernardi G., 2012, arXiv:1201.1700v1

Greig B., Mesinger A., 2017, MNRAS, 465, 4838

Guzmán A. E., May J., Alvarez H., Maeda K., 2011, A&A, 525, A138

Haslam C. G. T., Klein U., Salter C. J., Stoffel H., Wilson W. E., Cleary M. N., Cooke D. J., Thomasson P., 1981, A&A, 100, 209

Haslam C. G. T., Salter C.J., Stoffel, H., Wilson W.E., 1982, Astronomy and Astrophysics Supplement Series, 47, 1

Heald G. H. et al., 2015, A&A, 582, A123

Hinshaw D. et al., 2013, ApJS, 208, 19

Kaurov A. A., Gnedin N. Y., 2016, ApJ, 824, 114

Kogut A. et al., 2011, ApJ, 734, 4

Kogut A., 2012, ApJ, 753, 110

Liu A., Parsons A. R., 2016, MNRAS, 457, 1864

Loeb A., Furlanetto S. R., 2013, The First Galaxies in the Universe, ISBN: 9780691144917, Princeton, NJ: Princeton University Press.

Madau P., Meiksin A., Rees M. J., 1997, ApJ., 475, 429

Maeda K., Alvarez H., Aparici J., May J., Reich P., 1999, A&S, 140, 145

Malhotra S., Rhoads J. E., 2004, ApJ, 617, L5

Mather J. C. et al. 1990, ApJL, 354, L37

Mather J. C. et al. 1994, ApJ, 420, 439

McGreer I. D., Mesinger A., D'Odorico V., 2015, MNRAS, 447, 499

Mellema G. et al., 2013, Exp. Astronomy, 36(1-2), 235-318.

Mesinger A., 2010, MNRAS, 407, 1328

Mesinger A., Ferrara A., Spiegel D, 2013, MNRAS, 431, 621

Monsalve R., Rogers A. E. E., Mozdzen T., Bowman J. D., 2016, IEEE Trans on Microwave Theory Techniques, 64, 2631

Monsalve R., Rogers A. E. E., Bowman J. D., Mozdzen T., 2017, ApJ, 835, 49

Monsalve R., Rogers A. E. E., Bowman J. D., Mozdzen T., 2017, preprint arXiv:TBD

Morales M. F., Wyithe J. S. B., 2010, ARA&A, 48, 127

Morandi A., Barkana R., 2012, MNRAS, 424.4, 2551

Mozdzen T. J., Bowman J. D., Monsalve R. A., Rogers A. E. E., 2016, MNRAS, 455, 3890

Mozdzen T. J., Bowman J. D., Monsalve R. A., Rogers A. E. E., 2017, MNRAS, 464, 4995

Natarajan A., Schwarz D., 2009, Phys. Rev. D., 80, 043529

New Worlds, New Horizons in Astronomy and Astrophysics, National Academic Press, 2010, available at: http://www.nap.edu/catalog/12951/new-worlds-new-horizons-in-astronomy-and-astrophysics.

Offringa A. R. et al., 2015, PASA, 32, e008

Parsons A. R. et al., 2014, ApJ, 788, 106

Patra N., Subrahmanyan R., Raghunathan A., Shankar N. U., 2013, Exp. Astronomy, 36, 319

Patra N., Subrahmanyan R., Sethi S., Shankar N. U., Raghunathan A., 2015, ApJ, 801, 138

Pentericci L. et al. 2011, ApJ, 743, 132

Pentericci L. et al. 2014, ApJ, 793, 113

Planck Collaboration I, 2016, A&A, 596, A107

Planck Collaboration XLVII, 2016, A&A, 596, A132

Platania P. et al., 2003, A&A, 410, 847

Pober J. et al., 2015, ApJ, 809, 62

Pritchard J., Loeb A., 2008, Phys. Rev. D, 78, 10

Pritchard J. R., Loeb A., 2010, Phys. Rev. D, 82, 3006

Pritchard J., Loeb A., 2012, Rep. Prog. Phys., 75, 8

Raghunathan A., Shankar N. U., Subrahmanyan R., 2013, IEEE Antennas and Propagation, 61, 7, p. 3411

Remazeilles P., Dickinson, C., Banday, A.J., Bigot-Sazy, M.-A., Ghosh, T., 2015, MNRAS, 451, 4311

Rhoads R. et al., 2013, ApJ, 773, 1

Roberts W. K., 1957, Proc. IRE, 1624

Robertson B. et al., 2013, ApJ, 786, 71

Robertson B. E., Ellis R. S., Furlanetto S. R., Dunlop J. S. 2015, ApJL, 802, L19

Rogers A. E. E., Bowman J. D., 2008, ApJ, 136, 641

Rogers A. E. E., Bowman J. D., 2012, Radio Science, 47.6

Rogers A. E. E., Bowman J. D., Vierinen J., Monsalve R., Mozdzen T., 2015, Radio Science, 50, 130

Rogers A. E. E., 2015, MIT Haystack Observatory EDGES Memorandum, 088

Schenker M. A. et al. 2013, ApJ, 768, 196

Schenker M. A., Ellis R. S., Konidaris N. P., Stark, D. P. 2014, ApJ, 795, 20

Seiffert M. et al, 2011, ApJ, 734, 6

Singh S., Subrahmanyan R., Shankar N. U., Raghunathan A., 2015, ApJ, 815, 88

Singh S., Subrahmanyan R., Shankar N. U., Raghunathan A., 2017, ArXiv 1703.06647

Smoot G. F., 1999, in Microwave Foregrounds, ASP Conf. Ser. 181, ed. A. de Oliveira-Costa & M. Tegmark (San Francisco: ASP), 61

Sokolowski M. et al., 2015, Pub. Ast. Soc. Australia 32, e004

Sokolowski M. et al. 2015, ApJ, 813, 18

Stark D. P., Ellis R. S., Chiu K., Ouchi M., Bunker A. 2010, MNRAS, 408, 1628

Subrahmanyan R., Cowsik R., 2013, ApJ, 776, 42

Suh S. et al., 2004, IEEE 60th VTC, 1

Sutinjo A. T. et al., 2015, IEEE Transactions on Antennas and Propagation, 63, 5433

Taylor G. B. et al, 2012, LWA memo 185, available at http://www.phys.unm.edu/ lwa/memos/memo/lwa0185.pdf

Thyagarajan N. et al., 2015, ApJ, 804, 14

Tingay S. J., 2013, PASA, Vol. 30, e007

Tilvi V. et al. 2014, ApJ, 794, 5

Treu T., Schmidt K. B., Trenti M., Bradley L. D., Stiavelli M., 2013, ApJL, 775, L29

Turtle A. J., Pugh J. F., Kenderdine S., Pauliny-Toth I. I. K., 1962, MNRAS, 124, 297

van Haarlem M. P. et al., 2013, A&A 556, A2

Vedantham H. K. , Koopmans L. V. E., de Bruyn A. G., Wijnholds S. J. , Ciardi B., Brentjens M. A., 2014, MNRAS, 437, 1056

Voytek T. C., Natarajan A., Garcia J. M. J., Peterson J. B., Lopez-Cruz O., 2014, ApJL, 782, L9

Wayth R. B. et al., 2015, PASA, 32, e025

Wouthuysen S. A., 1952, Astronomy J., 57, 31

Wright E. L., 2006, PASP, 118, 1711

Zahn O. et al., 2012, ApJ, 756, 65

Zaroubi S. et al., 2012, MNRAS, 425, 2964

Zaroubi S., 2013, The Epoch of Reionization in Astrophysics and Space Science Library, vol. 396, The First Galaxies, ed. Wiklind T., Mobasher B., & Bromm V., Springer, Berlin, Heidelberg

Zheng H. et al., 2017, MNRAS, 464, 3486

APPENDIX A

EVALUATING THE ACCURACY OF SIMULATED ANTENNA BEAM PATTERNS USING CST'S MICROWAVE STUDIO

A.1 Introduction

The purpose of this study was to optimize the settings for the Computer Simulation Technology's Microwave Studio (CST) simulation software (version 2014), using the Time Domain Solver, so that it would correctly reproduce the beam directivity pattern of a complicated structure like the EDGES antenna. To do this, we chose a reference structure for which the directivity of the beam was known in analytic form and would resemble the behavior of the EDGES antenna. The reference structure is a thin $\frac{1}{2}\lambda$ wire-dipole $\frac{1}{4}\lambda$ above an infinite ground plane. An initial simulation of this structure was promising, but there were irregularities in the beam shape between 90 and 100 MHz. The first part of this study describes what was thought to be a simple fix: 1) either increasing the size of the simulation box surrounding the dipole; or 2) adjusting the dipole's wire diameter or the width of the gap used to excite the two wires. The second part of the study, mesh setting optimization, was conducted when the first study did not produce the results desired. Appropriate metrics were developed in the first part of the study, which proved useful for the second part.

A.2 Part 1: Exploring the Size of the Simulation Box Surrounding the Dipole and the Dimensions of the Wire Dipole.

Since the horizontal $\frac{1}{2}\lambda$ wire dipole is supposed to be infinitely thin and have an infinitely small gap between the two wires, variations on these dimensions were studied to determine the best simulation size to use for these small dimensions. It was also thought that the amount of simulation bounding box volume given to the CST simulator was affecting the low frequency results, and thus we also studied its effect in part 1.

A.2.1 Directivity

The directivity $D(\theta, \phi)$, a unitless quantity, is given by (Balanis, 2005)

$$D(\theta, \phi) = \frac{U(\theta, \phi)}{U_0} = \frac{U(\theta, \phi)}{P_{\text{rad}}^{\text{Total}}/4\pi} \tag{A.1}$$

where $U(\theta, \phi)$ is the radiation intensity in a particular direction in units of W per unit solid angle, U_0 is the radiation intensity of an isotropic source also in W per unit solid angle, but is a single number independent of angle, and $P_{\text{rad}}^{\text{Total}}$ is the total radiation power in W, also a single number. Conceptually, $D(\theta, \phi)$ is the ratio of the radiation intensity in a given angular direction as compared to the intensity averaged over all directions. Stated another way, it is the ratio of the radiation intensity in a given direction over that of an isotropic source. When the directivity is stated as a single number, it refers to the maximum value of the directivity. For antenna beams whose directivity or shape is different at each frequency, the directivity is then a function of frequency, $D(\theta, \phi, \nu)$, and we say the beam is chromatic or has chromaticity. Fig. A.1 shows 3D simulations of the dipole's beam directivity, which is widest (more responsive) perpendicular to the excitation axis and narrowest (less responsive) parallel to the excitation axis.

A.2.2 Metrics

For comparison metrics we use 1) the difference in directivity patterns of the beams, i.e., -3 dB points in the parallel and perpendicular directions to the excitation axis; 2) the RMS error from a polynomial fit to the simulated antenna temperature when pointed at the radio sky derived from a frequency scaled Haslam sky map (Haslam et al., 1981); and 3) the derivative of the beam with respect to frequency. Various cross sections (different azimuth ϕ values) of the beam were made and the zenith angle (θ) values of 3 dB points recorded. The RMS error from fitting

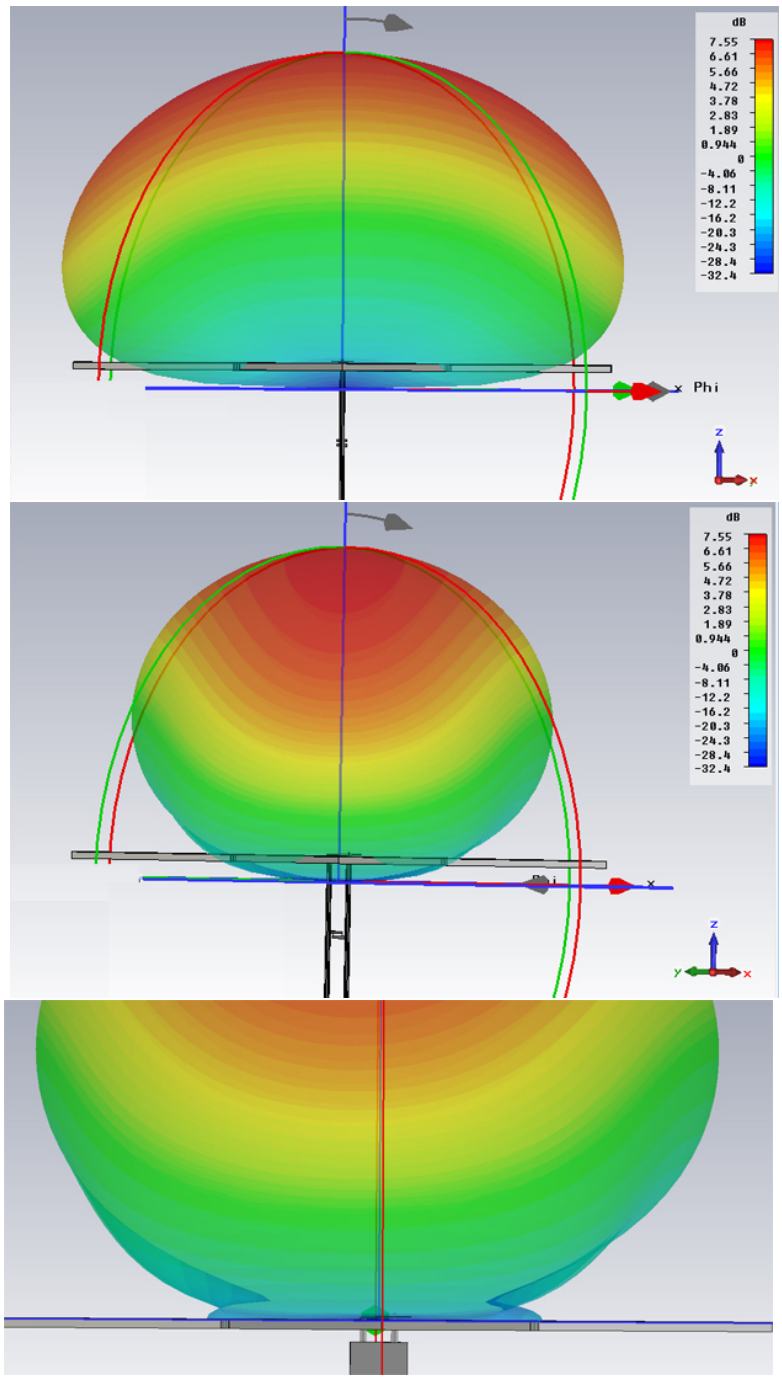

Figure A.1: Beam directivity for the EDGES dipole-like antenna. The top panel is looking perpendicular to the excitation axis and the middle figure is looking parallel to the excitation axis. The lower panel shows the development of sidelobes at higher frequencies as the ground plane becomes electrically further away from the antenna panels than $\frac{1}{4}\lambda_0$.

$\Sigma_{n=0}^{N} \log^n(\nu)$ to the antenna's response (convolution with the sky) using a frequency scaled (spectral index -2.5) Haslam Skymap ($T_{\text{sky}} = T(408\text{ MHz}) \times (\nu/408)^{-2.5}$), which replicates the spectral shape of synchrotron radiation. The frequency range used was 100 to 190 MHz and the order of the fitting polynomial ranged from N = 2 to N = 5 (3 terms to 6 terms). The antenna is located at the Murchison Radio-astronomy Observatory in Western Australia at $\sim -26^\circ$ latitude and the simulations were run for the full range of LST times. Lastly, we developed a tool that uses the derivative of the beam directivity to evaluate its smoothness, which is a contributing factor in isolating the Epic of Reionization (EOR) Signal by cleanly removing the 10^5 times brighter foreground Galactic synchrotron radiation.

A.2.3 Simulation Parameters

In this study, the first set of simulation parameters were 1) the amount of simulation space added to the CST simulations; 2) the wire diameter of the dipole; and 3) the gap distance between the two segments. The second set of parameters focused on optimizing meshing settings. These results are reported in Sections A.3 and A.4.

A.2.4 CST Simulations

We compared the metrics from the simulation results using beams acquired from an analytic expression against beams acquired from CST simulations using the legacy Hex Meshing method of CST 2014. The analytic beam directivity, $Beam(\theta, \phi, \nu)$, was derived assuming a classic infinitely thin $\frac{1}{2}\lambda$ dipole, $\frac{1}{4}\lambda$ over an infinite ground plane and is expressed by

$$Beam(\theta, \phi, \nu) = \left[\frac{\cos(kL/2 \cdot \cos\theta') - \cos(kL/2))}{\sin\theta'}\right]^2 \left[\sin^2\left(\frac{\pi h}{2}\cos\theta\right)\right], \quad \text{(A.2)}$$

$$h = \frac{\nu}{\nu_{\text{height}}} = \frac{\lambda_{\text{height}}}{\lambda}, \quad \text{(A.3)}$$

$$\theta' = \cos^{-1}(\sin\theta \sin\phi), \quad \text{(A.4)}$$

where (θ, ϕ) are spherical coordinates, $\nu_{\text{height}} = 176.7$ MHz ($\lambda_{\text{height}} = 1.696$ m), and the excitation axis of the dipole is aligned with $\phi = 0°$. The frequency dependency is due to the fact that the height above the ground plane can be exactly $\frac{1}{4}\lambda$ only at one frequency. At all other frequencies, the antenna is either higher or lower than $\frac{1}{4}\lambda$ and thus affects the development of side lobes in the beam pattern, which cause distortions to the smoothness of the directivity.

The thin wire dipole was placed above an infinite ground plane at a distance equal to $\frac{1}{4}\lambda$ at 176.7 MHz, chosen to mimic the beam structure near the zenith of the EDGES antenna (see Fig. A.2). Table A.1 lists the common CST parameter settings, and Table A.2 lists the varied parameters of the 19 simulations. Fig. A.3 shows a diagram of the bounding simulation space box and a close up of the dipole gap.

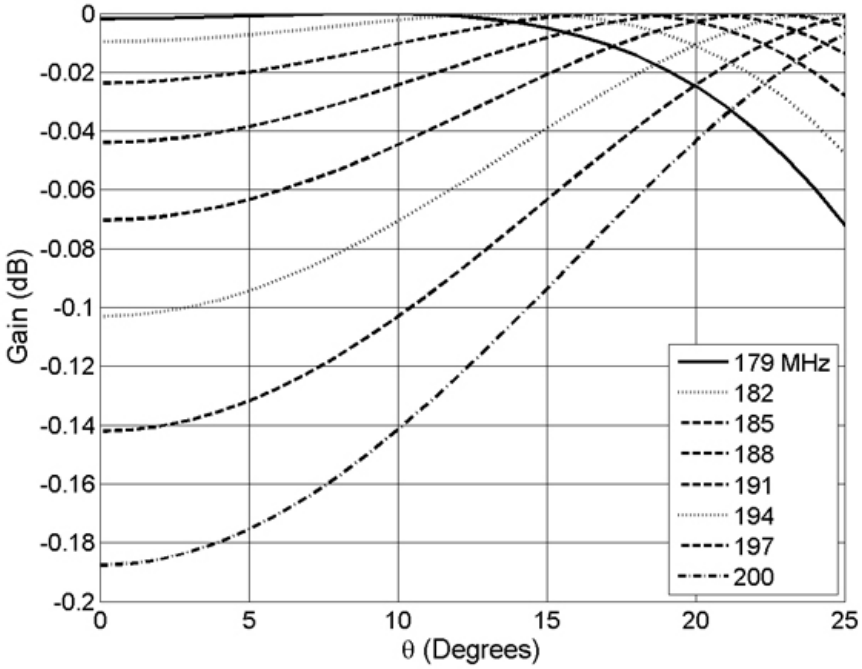

Figure A.2: Directivity variations within an inclination of 25° along the $\phi = 90°$ direction at different frequencies are due to the fact that the antenna height above the ground plane can only be $\frac{1}{4}\lambda$ at one frequency (here 176.7 MHz). Higher frequencies (shorter wavelengths) mean that the electrical distance is higher, which causes sidelobes (multiple directivity peaks and nulls).

A.3 Part 1 Results from Gap, Diameter, and Bounding Box Variations

A.3.1 Beam Directivity Profile and 3 dB Points

We show typical normalized gain profiles of the beam at $\phi = 0°$ and 90° at various frequencies in Fig. A.4. We compare the normalized 3 dB (half power) values of the simulated beams to the analytic beams in Fig. A.5. The values for $\phi = 90°$ match to within $\pm 0.1°$ and are are not strongly frequency dependent, while values for $\phi = 0°$ match to within $\pm 0.15°$, but become worse with higher frequencies, differing by as much as 0.7°. Runs 1 and 2 fall out of this pattern and do not match as closely.

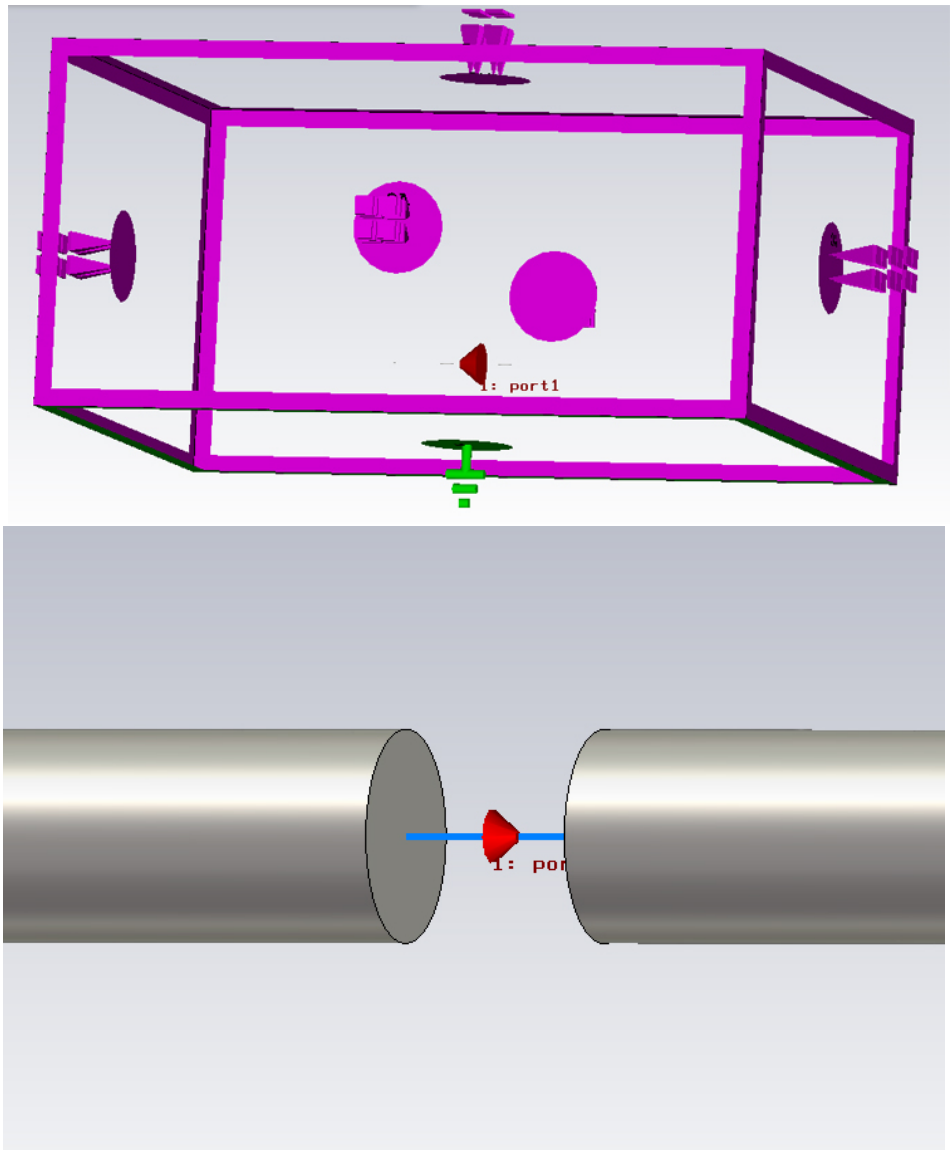

Figure A.3: Simulation boundary box with the bottom boundary set to electrical ground and the other five sides set to "open space" (top). The dipole wire is near the center of the box and is barely visible at this scale. The distance from the dipole to the boundary edges is a simulation parameter. The total length of the wire dipole is 33.42″, and the gap and wire diameter are simulation parameters (bottom). The wire is placed 16.7″ above an infinite ground plane, which is $\frac{1}{4}\lambda$ at 176.7 MHz. Close up view of the gap of the wire dipole. The gap and the wire diameter are very small compared to the length of the dipole.

Table A.1: Common CST 2014 simulation parameters using Legacy Hex Meshing

Parameter	Value
Mesh Type	PBA
Lines per Wavelength	75
Lower Mesh Limit	45
Mesh Ratio Limit	65
Solver Accuracy	-50 dB
Edge Enhancement	85%
Frequency Range of Simulation	80 to 220 MHz
Frequency to Calculate Extra Space	100 MHz
Reflection at Boundaries	1 x 10^{-4}

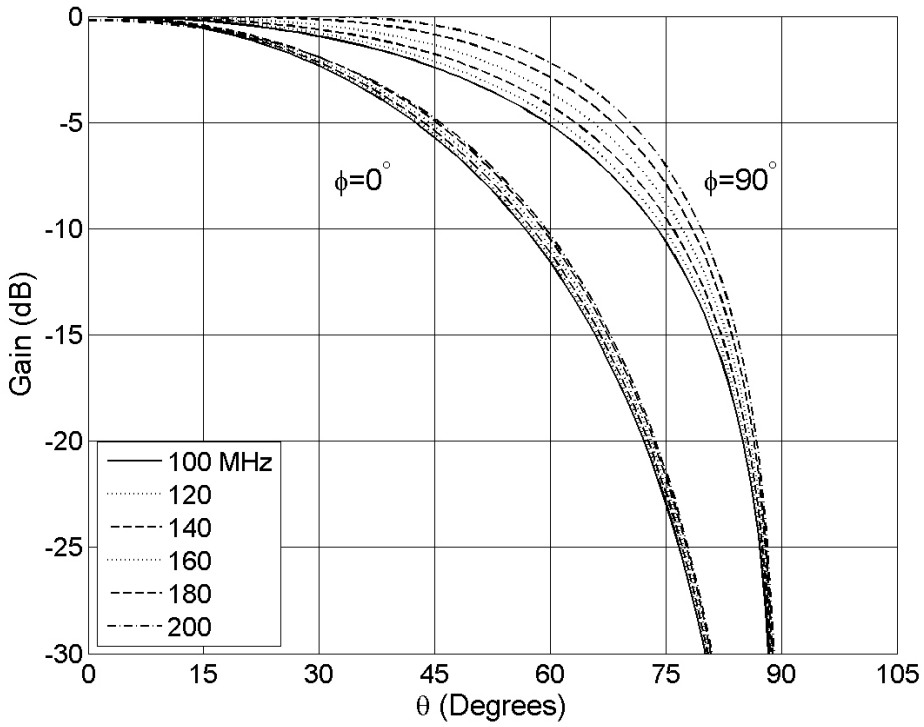

Figure A.4: Typical normalized gain (directivity) profiles at $\phi = 0°$ and 90° for the finite length dipole at several frequencies. Differences between the analytic beam and the simulated beam can not be easily seen at this scale.

Table A.2: Simulation parameters particular to each run and not listed in Table A.1

Simulation Number	Simulation Boundary Distance to Structure (fraction of λ at 100 MHz)	Wire Diameter (inches)	Center Gap (inches)
1	1	0.05	0.50
2	1	0.10	0.50
3	1/2	0.05	0.50
4	1/2	0.10	0.50
5	1/4	0.05	0.50
6	1/4	0.10	0.50
7	1/8	0.05	0.50
8	1/8	0.10	0.50
9	1/16	0.05	0.50
10	1/16	0.10	0.50
11	1/32	0.010	0.010
12	1/32	0.010	0.50
13	1/32	0.025	0.025
14	1/32	0.025	0.500
15	1/32	0.050	0.025
16	1/32	0.050	0.050
17	1/32	0.050	0.100
18	1/32	0.050	0.250
19	1/32	0.050	0.500
20	1/32	0.050	0.750
21	1/32	0.10	0.50

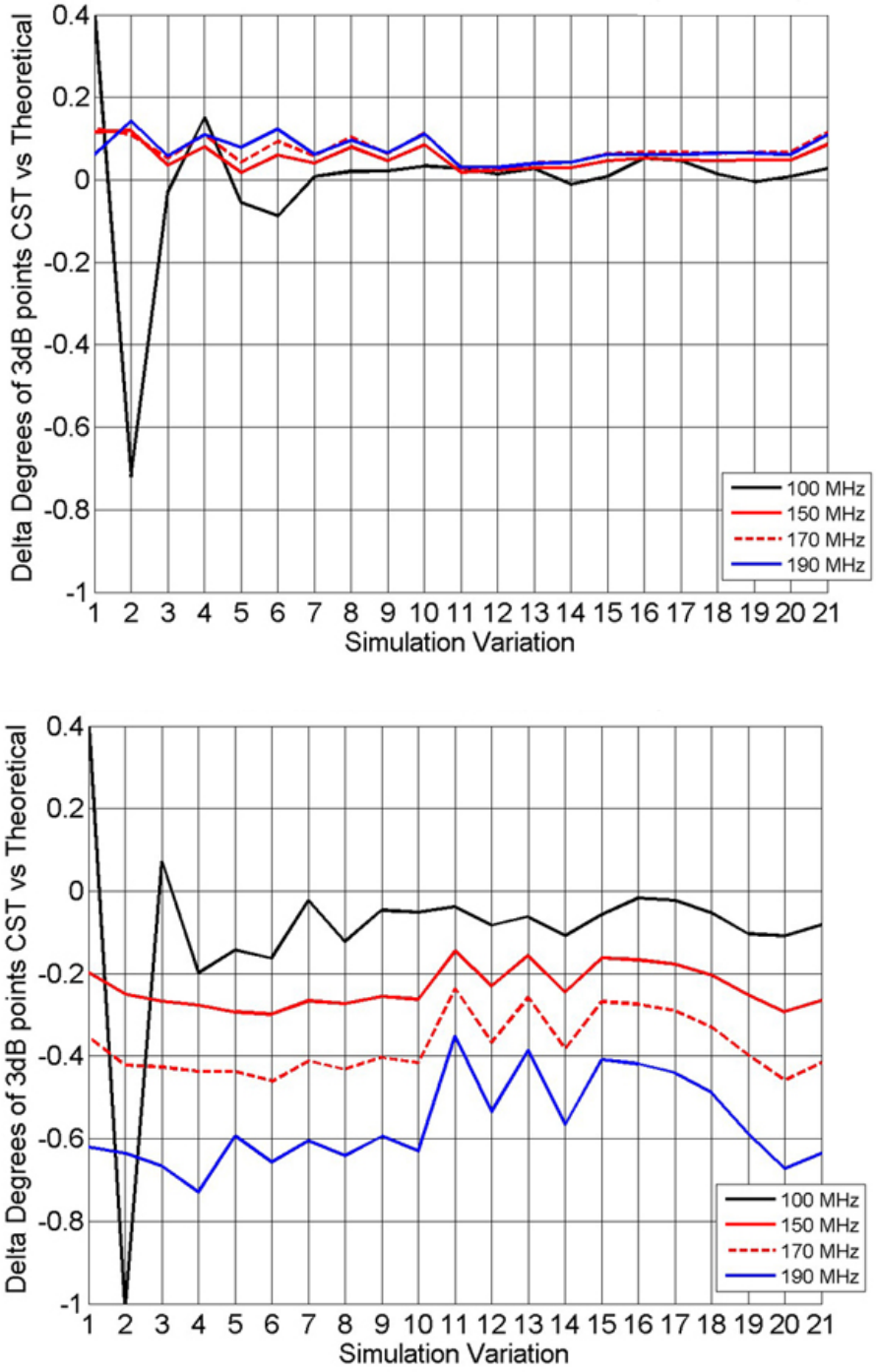

Figure A.5: Differences between the -3 dB points of the analytic beam and the CST simulated beam at azimuthal angles of $\phi = 0°$ (top) and 90° (bottom) for the 21 sets of model parameters.

A.3.2 RMS Error vs LST

Figs. A.6 (runs 3 and 4) and A.7 (runs 19 and 21) illustrate the effect of different wire diameters and different amounts of boundary space. Fig. A.6 forced one-half wavelength of space between the structure and the simulation boundary, and Fig. A.7 used 1/32 of a wavelength (at 100 MHz). The top panels used a wire diameter of of $0.05''$ and the bottom panels used $0.10''$, both used wire gaps of $0.50''$. Since the total wire length is over $33''$, the gap is relatively small and represents less than 2% of the total length. Small changes can be noticed for wire diameter changes, but larger changes can be seen when the amount of simulation space is increased, which is generally detrimental. A possible cause for this could be in rounding errors as the number of mesh cells increases proportional to the volume of simulation area. Run 19 shown in the top panels of A.7, appears to yield the lowest residuals of all of the combinations (gap=0.50", D_{wire}=0.05"). We will next take a closer look at run 19 via the beam derivatives to see why the RMS error does not decrease as rapidly for run 19 as the analytic beam. The Galaxy down (LST=4 h) and Galaxy up (LST=17.3 h) RMS errors are summarized in Fig. A.9, top and bottom panels respectively.

The RMS error of the fitted simulated antenna temperature vs LST is shown in Fig. A.8 with the analytic beam results on the right side and the CST derived beam results (Run 19) on the left. Note how the RMS error for the analytic beam quickly drops below 1 mK as the number of fitting terms increase while the CST derived beam remains above 2 mK. The residuals values at LST = 4.0 hours are seen more clearly in the bottom panels. The fit of low order polynomials are very similar in the two cases, but there is more structure in the CST derived beam as the residual errors are not removed when the order of the polynomial is increased as they are in the theoretical analytic beam.

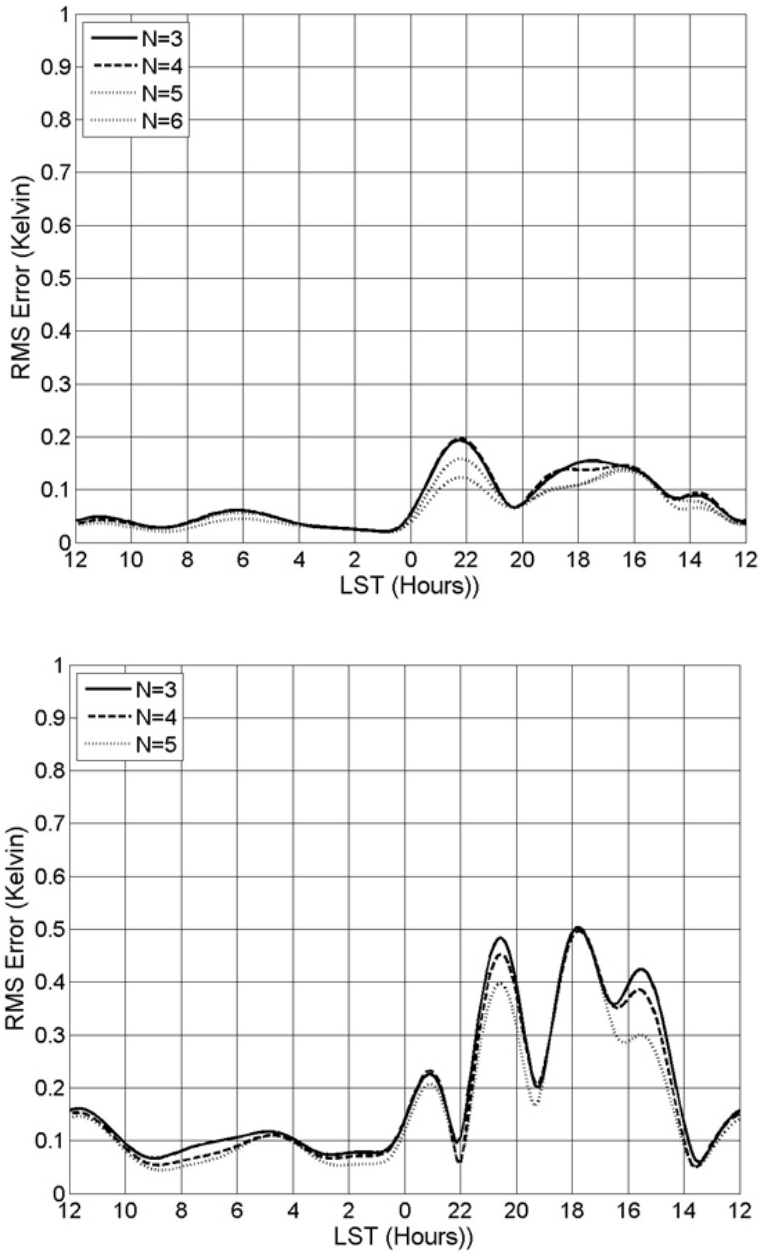

Figure A.6: Simulation runs 3 (top) and 4 (bottom): RMS error values vs LST using a wire dipole with a center gap of $0.50''$ with wire diameters of $0.05''$ (top) and $0.10''$ (bottom). Simulation space between the dipole structure and the end of the simulation boundary is $\frac{1}{2}\lambda$. The wire diameter differences have a significant impact.

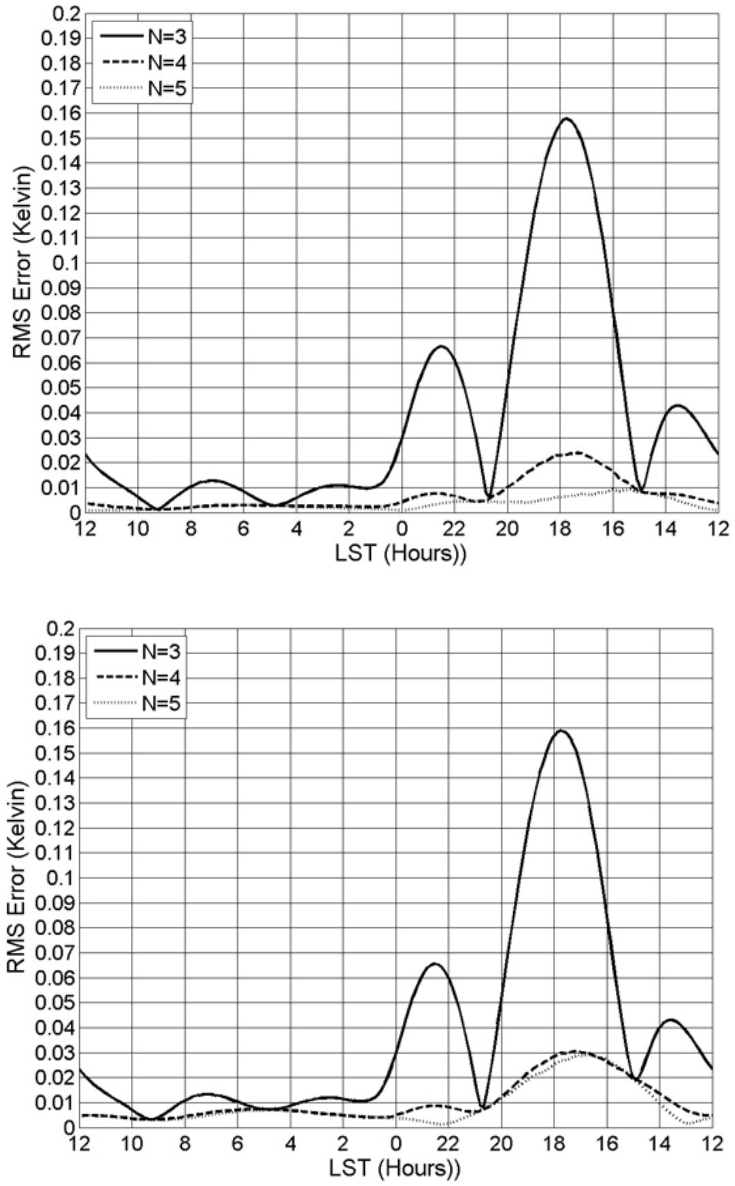

Figure A.7: Simulation runs 19 (top) and 20 (bottom): RMS error values vs LST using a wire dipole with a center gap of $0.50''$ with wire diameters of $0.05''$ (top) and $0.10''$ (bottom). Simulation space between the dipole structure and the end of the simulation boundary is $\frac{1}{32}\lambda$. Run 19 had the best RMS error performance overall. The improved performance is thought to be due to less simulation rounding error due to a lower mesh cell count.

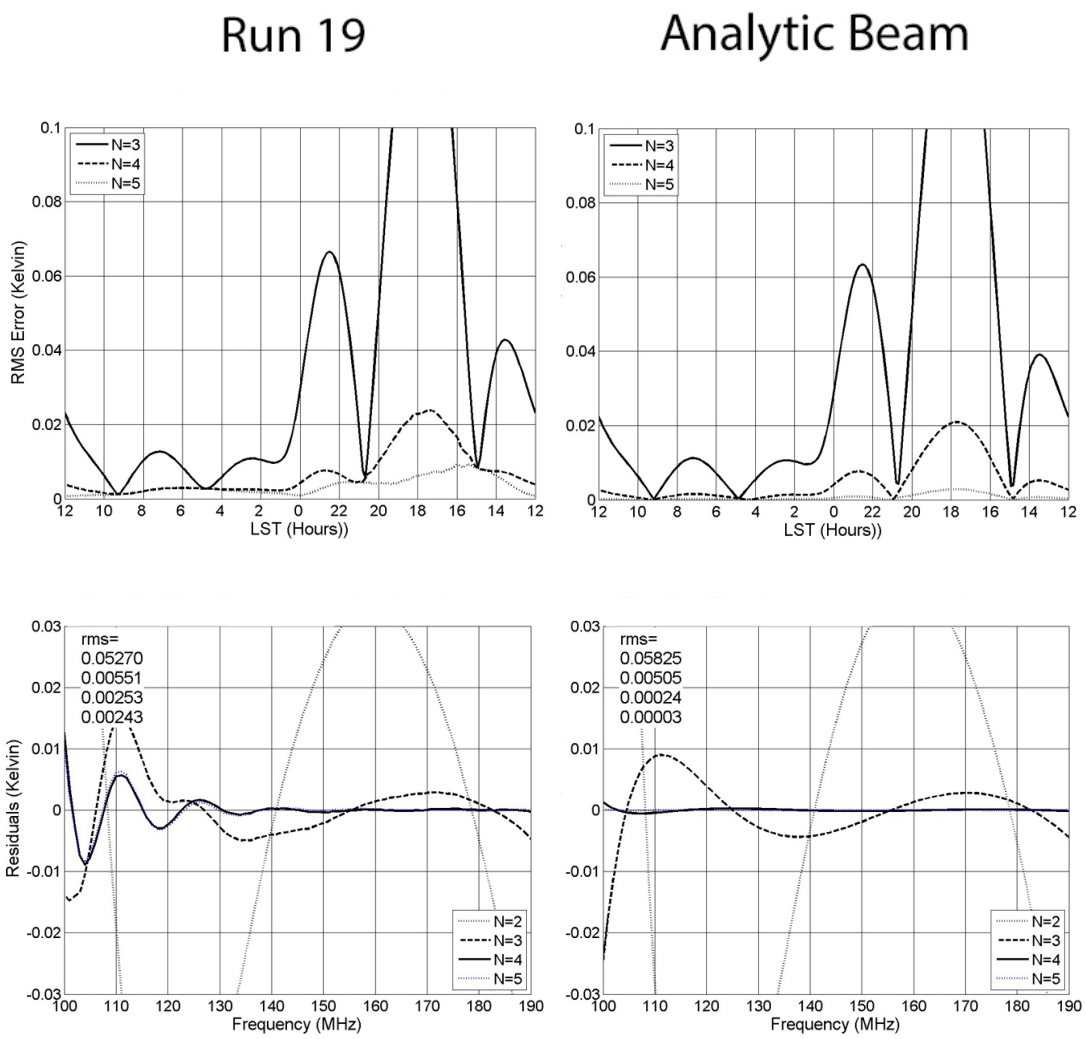

Figure A.8: The RMS error vs LST is shown for the analytic $\frac{1}{2}\lambda$ beam results (top right) and the CST derived beam results, Run 19, (top left). Fitting residuals are shown for the analytic beam (bottom right) and the CST beam (bottom left) at an LST value of 4.0 hrs. Note how quickly the residuals vanish for the analytic model while they saturate near 2 mK for the CST model as the fitting order increases.

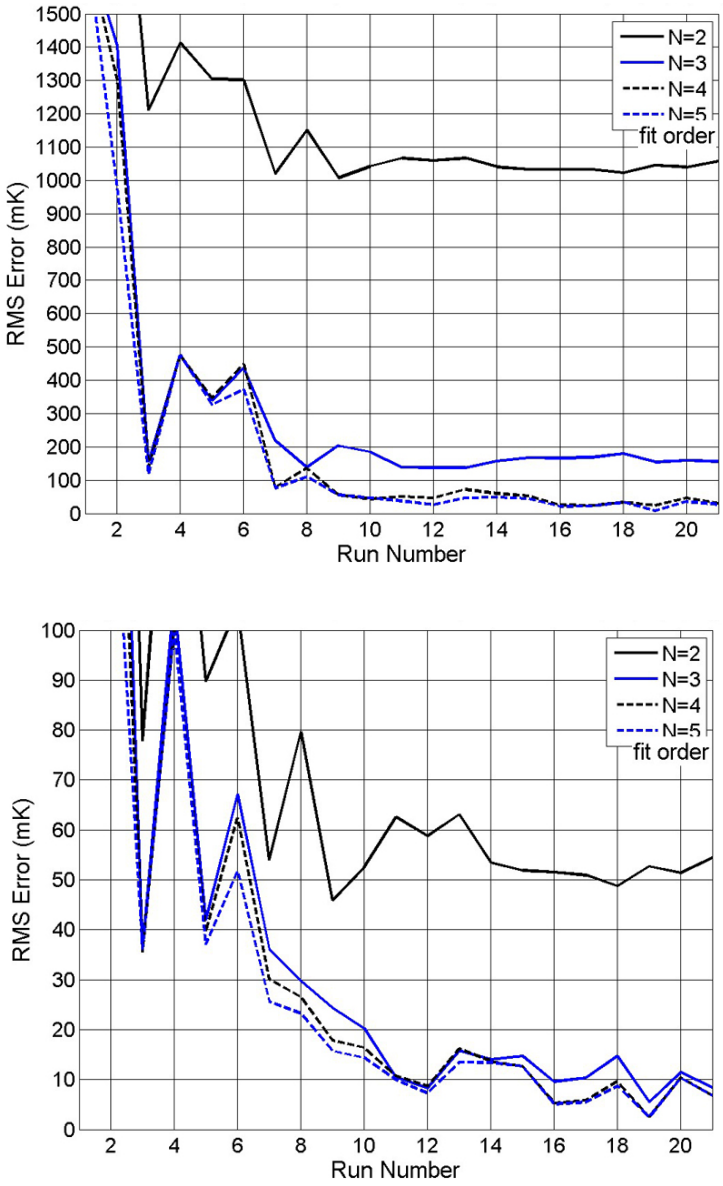

Figure A.9: Summary of the RMS fitting errors for various order polynomial fits for the 21 runs measured at two LST values. The top graph shows values taken with the Galaxy overhead (LST of 17.3 h) during which time the sky in view is not uniform in temperature (structure). The bottom graph uses antenna temperatures with the Galaxy mostly down at LST = 4.0 h and the RMS fitting errors are lower because the sky is fairly uniform in temperature and chromatic beam effects are minimized.

A.3.3 Beam Derivatives

The smoothness of the beam was evaluated by taking the derivative of the beam with respect to frequency. That is, for each beam value at a given θ and ϕ, the difference between the value at one frequency and the next frequency (1 MHz away) was taken ($dBeam(\theta, \phi)/d\nu$) and in this manner a derivative plot was made with frequency on the y-axis and the inclination (angle from the zenith) θ on the x-axis. To aid in the analysis of these plots, it is instructive to plot the magnitude of the derivative vs frequency at a fixed θ value. In this section we will show the derivative plots of runs 7, 19, and the ideal case of the analytic dipole.

Fig. A.10 displays the derivative beam plots for CST runs 7 and 19 (left and right panels respectively) taken in the direction along the excitation axis, $\phi = 0°$ (top panels) and perpendicular to the excitation axis, $\phi = 90°$ (bottom panels). Irregularities can be seen in the lower frequencies in run 19 and some variation near 110 MHz in run 7. A cut line through the value of $\theta = 40°$ was made and the magnitude of the derivative was plotted vs frequency in Fig. A.11. The irregular value for the lower frequencies can now be seen more clearly and indicates a problem with simulation 19 as these sharp oscillations do not look to be caused by a physical phenomenon. Run 7 also highlights issues with the lower frequencies.

Fig. A.12 shows the results for the analytic $\frac{1}{2}\lambda$ dipole beam in which ($\phi = 0°$) is on the left side and ($\phi = 90°$) is on the right. The beam changes across frequency are very smooth and the expected change in slope occurs at 176.7 MHz just as in the case of the CST simulated beams. The smooth derivatives are the reason why the polynomial fits have very low residuals - the beam does not couple the structure in the sky into the antenna temperature. This is the goal for the CST simulations.

One item to note is the jaggedness of the cut lines through $\theta = 40°$ as seen in Fig. A.11. These lines are not causing issues with the fit. CST can simulate a short dipole over a ground plane very accurately because the match to the analytic model is very accurate despite this jaggedness being present. The residuals are less than 0.1 mK even with the presence of these ripples.

A.3.4 Motivation to Investigate CST Meshing Strategies

With the given meshing scheme and accuracy settings presented, CST can simulate the finite dipole over a ground plane accurately to a certain degree (5 to 10 mK RMS residual errors for a 5 term polynomial), but for EoR detection, higher accuracy is needed. Erratic differences of 0.001 dB over 1 MHz frequency steps are enough to cause 10s of mK of extra RMS error when fitting 5 term polynomials to the antenna response.

CST is adding more structure to the beam by inaccurately calculating the beam at low frequencies. Adding extra space to the simulation only makes the problem worse. The gap and diameter of the wire is important, but it is not the cause of the low frequency inaccuracy. The next step is to perform a meshing and accuracy study. We now present our findings of fine tuning the CST meshing scheme.

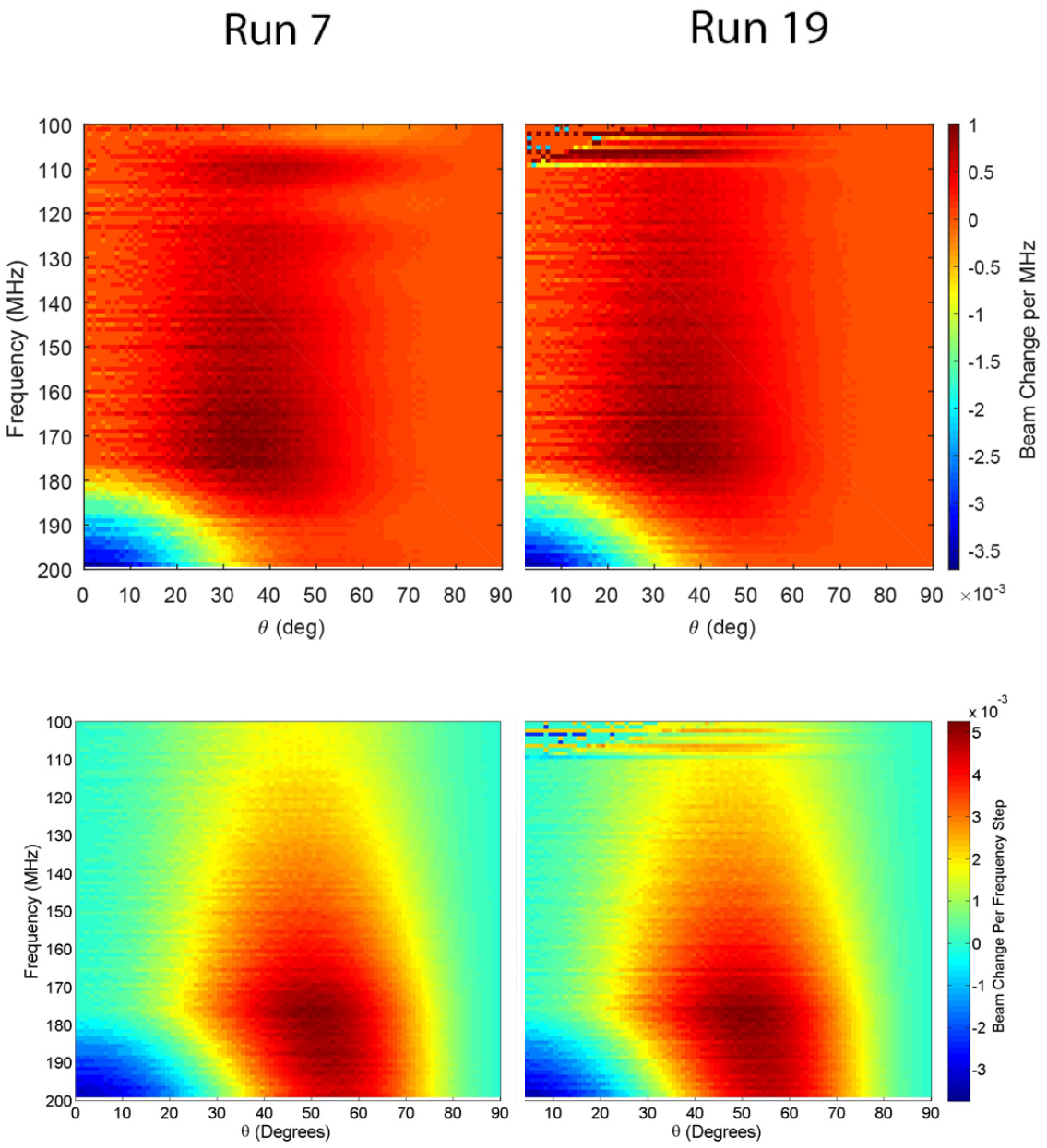

Figure A.10: Beam derivative plots for CST runs 7 and 19 (left and right panels respectively) taken in the direction along the excitation axis, $\phi = 0°$ (top panels) and perpendicular to the excitation axis, $\phi = 90°$ (bottom panels). Irregularities can be seen in the lower frequencies in run 19 and some variation near 110 MHz in run 7.

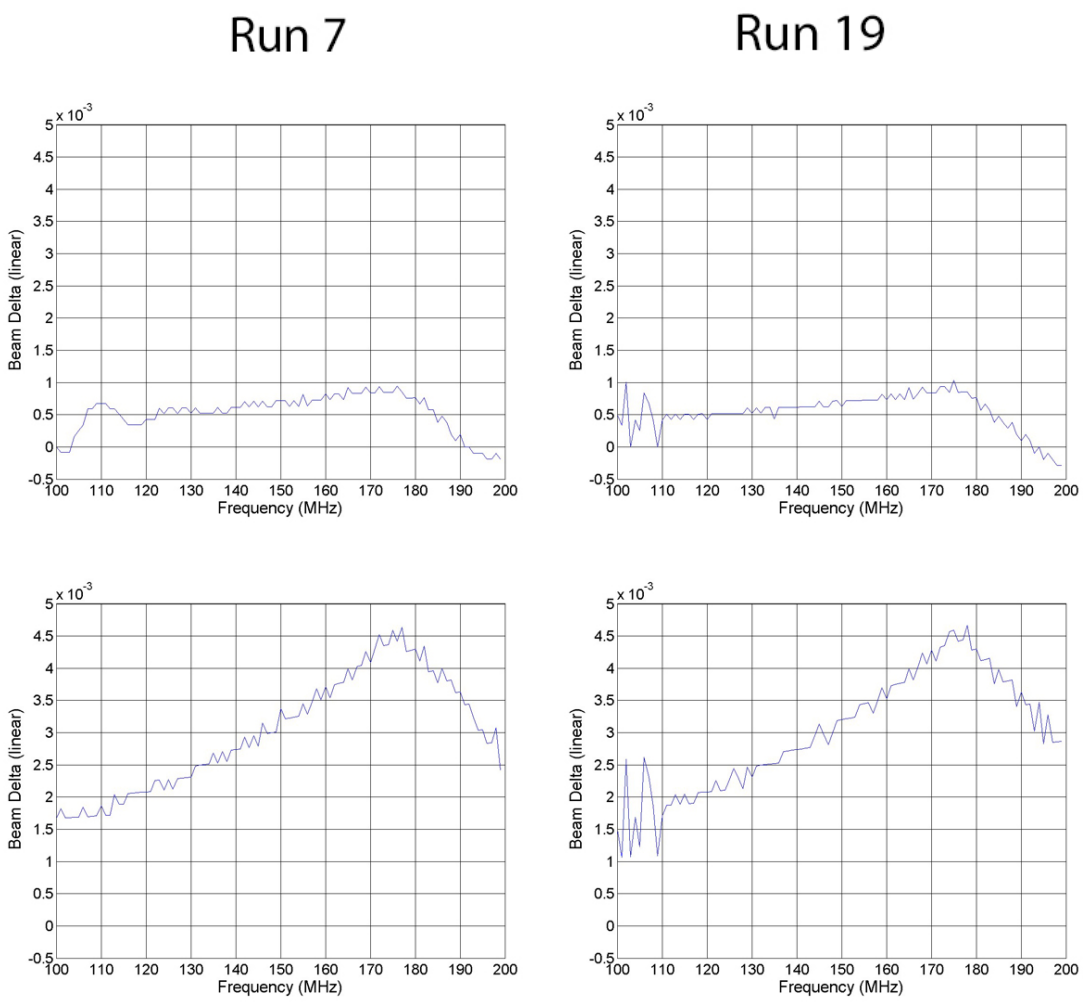

Figure A.11: Beam derivative plots for CST runs 7 and 19 (left and right panels respectively) for a fixed value of $\theta = 40°$ ($\phi = 0°$ [top], and $\phi = 90°$ [bottom]). The structures seen in Fig. A.10 are quantified with these plots and confirm that the irregularity of run 7 is centered on 110 MHz and that the oscillations below 110 MHz in run 19 are erratic. The oscillations are most likely due to the CST solver not converging to a stable solution in this area. Notice the change in slope at 176.7 MHz, the frequency at which the dipole is exactly $\frac{1}{4}\lambda$ above the ground plane.

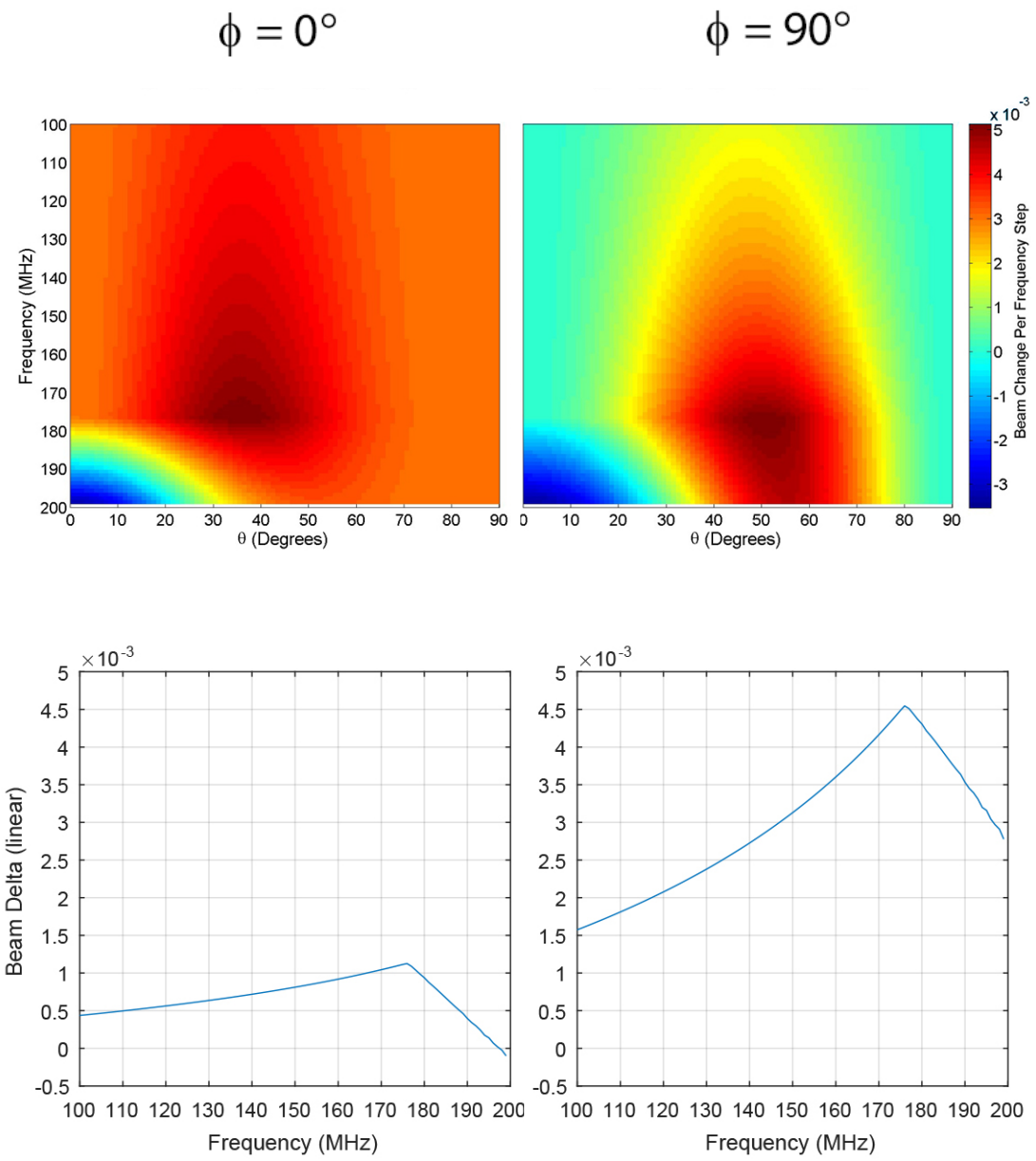

Figure A.12: Analytic $\frac{1}{2}\lambda$ dipole phi=0 deg (left) 90 deg (right) and views across frequency with a fixed angle from the zenith of $\theta = 40°$. The smoothness of the ideal dipole is seen in these graphs. If problems with beam smoothness exist, the derivative plots will quickly highlight the location of the issue.

A.4 Part 2: Results from Meshing Refinement

Choosing the correct mesh parameters is vital to getting accurate CST simulation results, but the procedure to obtain a good mesh differs for every simulation model, thus a meshing study should be the first task for every new simulation. This section reports results from varying the meshing parameters, some of which were generated automatically by enabling the iterative meshing setting. A total of 38 simulation settings were run with only 3 of the settings resulting in unsatisfactory results. A mesh that is too dense can lead to unsatisfactory results as well a mesh that is too sparse.

For brevity, we will not describe the exact meaning of many of the parameters because they are available in the CST User's Guide, but also because the interface and meshing options are enhanced each year resulting in the disappearance of some of the options and the appearance of others. The previous section, A.3, and all but 10 of the runs in this section used the CST legacy meshing scheme (common for CST 2013). Because three years have elapsed since this study was conducted and the CST meshing schemes are different now, the overall approach of finding an optimum mesh is more important than the specific details of the actual steps.

There are some common sense actions that can be taken to improve one's success with meshing. The structure to be simulated should be aligned parallel to the coordinate axis as much as possible because the Time Domain Solver generates rectangular grids. This avoids the need to approximate diagonal surfaces with staircased cuboid meshed cells. The circular nature of the wire dipole can not be avoided, but placing the wire along the x-axis, reduces the mesh count and simulation time, while increasing accuracy. A difficult aspect of this design is that it has both large and small features, requiring a mesh grid that is at least 7 times denser in each coordinate direction than the default typical CST settings.

A.4.1 Meshing Parameters

The first part of this report used PBA (Perfect Boundary Approximation) meshing with 75 mesh lines per wavelength and the S11 accuracy to -50dB. This section explores the realm of higher mesh lines (> 150) per wavelength, which requires Fast PBA with Enhanced accuracy (FPBA). We also raised the S11 accuracy to -80 dB. Tables A.3 and A.4 list the simulation settings, which are described later in this section.

Extra space was varied, but again, too much extra space was found to be detrimental to the results. Sub-gridding and two adaptive mesh methods were explored a) Expert system based and b) Energy system based. Sub-gridding is the use of a non-regular mesh density. Normally, if the density of mesh lines is increased for a small geometry, this mesh density is extended to the simulation boundary. In sub-gridding, the finer grid is not continued out to the simulation boundary edge (see Fig. A.13). CST technical support does not recommend the use of this setting because, in their experience, it often adds more computing overhead than it saves, however we used it for most of the runs.

Adaptive meshing is the process by which CST begins with a starting point for the mesh and then iterates by modifying the mesh until a certain parameter is met. Expert based generally increases the grid density in every direction by a user specified number of lines per wavelength in subsequent iterations and monitors internal errors and convergence metrics to determine when a stable solution has been found. One can also specify other monitors such as changes in the S11 curve. Energy based is similar except CST focuses on the regions of highest energy or electric fields to determine when an optimum point has been reached. The grid density changes in each iteration by an internal calculation.

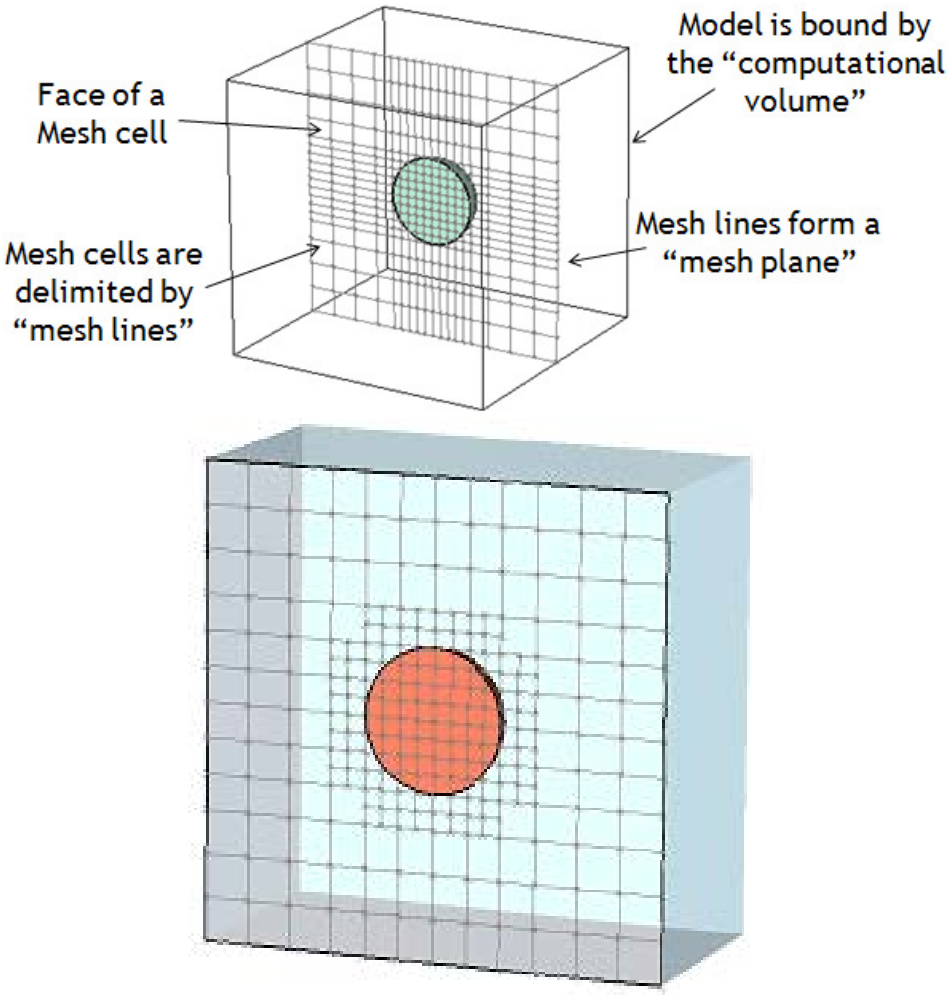

Figure A.13: Illustration of meshing using normal gridding (top) and sub-gridding (bottom). (CST White Paper, 2010).

For an example of setting S11 stability as an adaptive meshing goal, Runs 14-17 used an Energy based adaptive mesh (see Table A.4) and set the goal to be ΔS11 < 0.001 dB. The top of Fig. A.14 shows the S11 response for the 4 passes. The simulation converges on an S11 pattern at the second pass. The bottom of Fig. A.14 shows the convergence for an Expert based system using the 2014 meshing system. The two simulations converge to S11 patterns with minimums slightly different from each other, 163.55 MHz vs 163.10 MHz. The same minimum point is not always reached with different meshes (see Tables A.3 and A.4).

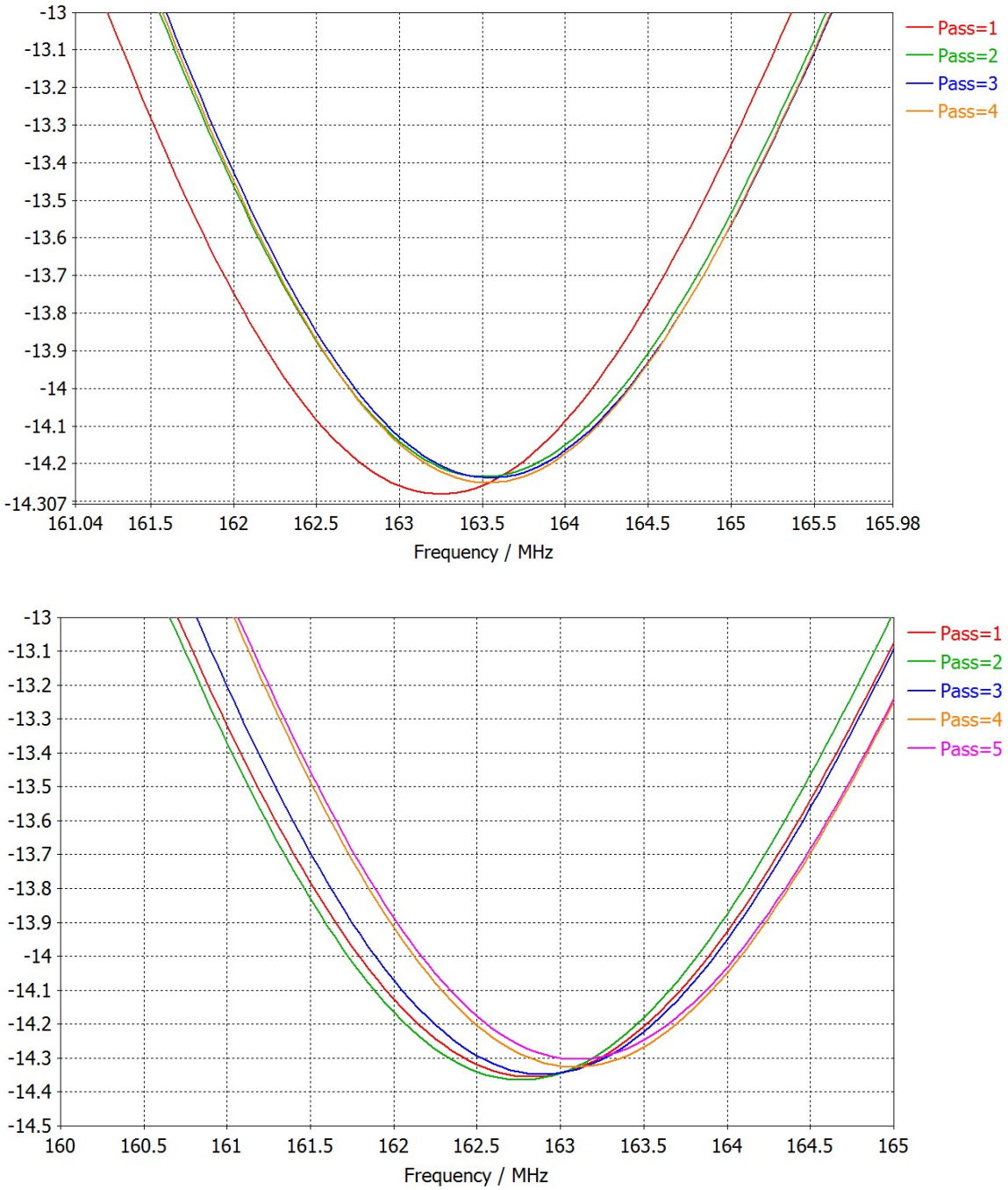

Figure A.14: S11 for each pass of an adaptive mesh iteration.

Three sets of variations, runs 29-38, used the new (at the time) 2014 meshing system (Table A.4) with adaptive meshing enabled. The results using the new system were similar to those of the old system, although the new system was not explored in the same detail as the previous meshing system.

Brief Description of Parameter Table Entries

Tables A.3 and A.4 list the simulation settings. Parameters that were not varied are not shown. This is not an exhaustive list of possible parameters, but the ones deemed to have the most impact on the results. Of the parameters varied, the most influential were grid density, extra parameter space, and the use of adaptive meshing.

Table Inputs and Outputs

We now give a brief explanation of some of the table entries that are inputs to the simulation and whose meanings might not be obvious by the column titles. "Lines per λ" in column 5 is the number of grid lines per wavelength applied in all three dimensions. This setting is a major factor in determining the number of mesh cells, which are rectangular cuboids. "Lower Mesh Limit" means that there should always be this many lines per wavelength even if some other parameter tries to make it sparser. "Mesh Line Ratio Limit" is the ratio of the smallest cell to the largest cell. "Edge Enhancement" directs the mesh algorithm to refine the mesh near edges when setting the mesh density. "Extra Space" is how much additional space the mesh algorithm should add between the structure and the simulation boundary.

The three monitored outputs in the table are 1) "Best RMS Error", which is the metric obtained from 4th order polynomial fitting at LST=4 h; 2) "Mesh Cells", a result of the meshing algorithm inputs, is the mesh count for the simulation; and 3) "S11 minimum" is a manually monitored metric of its location in frequency.

The strategy of the study was to try a different number of starting points for the mesh algorithm to observe the effects upon the metrics. One clear result was that under or over meshing generally made the results worse. Fortunately, many of the results yielded RMS error values between 0.5 and 2.0 mK, a result that could not be accomplished with the technique of modifying simulation boundary space and wire dipole thickness and gap dimensions.

A.4.2 Meshing Metric Results: RMS Error vs Run Number

The RMS error is plotted vs run number for the low RMS error (left) and high RMS error (right) LST locations (4 h and 17.3 h respectively) at latitude -26 in Fig. A.15. Fourth order results ranged between 0.5 mK and 2.2 mK for the low LST region, and 20 mK and 100 mK for the high LST region (magnified view in lower panels). Contrary to the favorable LST case, the least favorable LST case does see a decrease in RMS error when the order of the polynomial is increased from 4^{th} order to 5^{th} order. Eight runs were able to achieve sub mK error levels.

Short Dipole - CST Beam vs. Analytic Beam Models

One more data point that is not listed in the table of variations, but demonstrates the potential for CST accuracy, is the infinitesimal length diode. The short thin analytic dipole over a ground plane has less structure than the finite length dipole because the beam is not dependent upon the length of the dipole, and CST does an excellent job matching the analytic results. The approximation to the infinitesimal diode model used in the CST simulation was a wire 5″ in total length (short compared to 79 inches which is the wavelength at 150 MHz) with a diameter of 0.05″ and a central gap of 0.05″ over an infinite ground plane. The RMS error and residuals match very closely (Figs. A.16) and the beam derivative plots are smooth and absent of abrupt features

(Figs. A.17 and A.18). As noted earlier, the small ripples seen in the CST generated left panels of Fig. A.18 are not detrimental to producing < 1 mK RMS error levels. Also of interest is the fact that the beam is now more symmetrical and the peaks of the derivatives are more equal than in the case of the long dipole.

A.4.3 Meshing Metric Results: Derivative Plots

Run 15 is an example of a run with very low RMS errors (see Table A.3). Figs. A.19 and A.20 show the derivatives of the beams plotted vs frequency for both CST Run 15 and the analytic beam. The analytic beam changes very smoothly and evenly with frequency while the CST beam also changes smoothly, but shows some speckling. The small jaggedness in these plots (Fig. A.20) is at the level seen in the short dipole are not an issue as discussed earlier.

Run 10 is an example of a run that had less than ideal CST simulation parameters and shows relatively higher RMS errors than the other runs. The irregular features can barely be seen in Fig. A.21, but they become more obvious in Fig. A.22. Run 10 began with a relatively low mesh per wavelength setting of 110 mesh cells per wavelength and used a feature that may not be working quite right in CST setting the minimum mesh step instead of setting the max/min ratio. For this reason, it is not recommended to use this mesh parameter option.

A.5 Conclusions and Recommendations

From the results of this study, it is clear that an optimum mesh is needed to yield accurate results. The mesh should be as dense as possible, but not overly dense to the point of reducing accuracy. Adaptive meshing should be used, especially in the beginning, to find this point. The highest simulation frequency should be set above the desired frequency to make the simulator deal with finer structures.

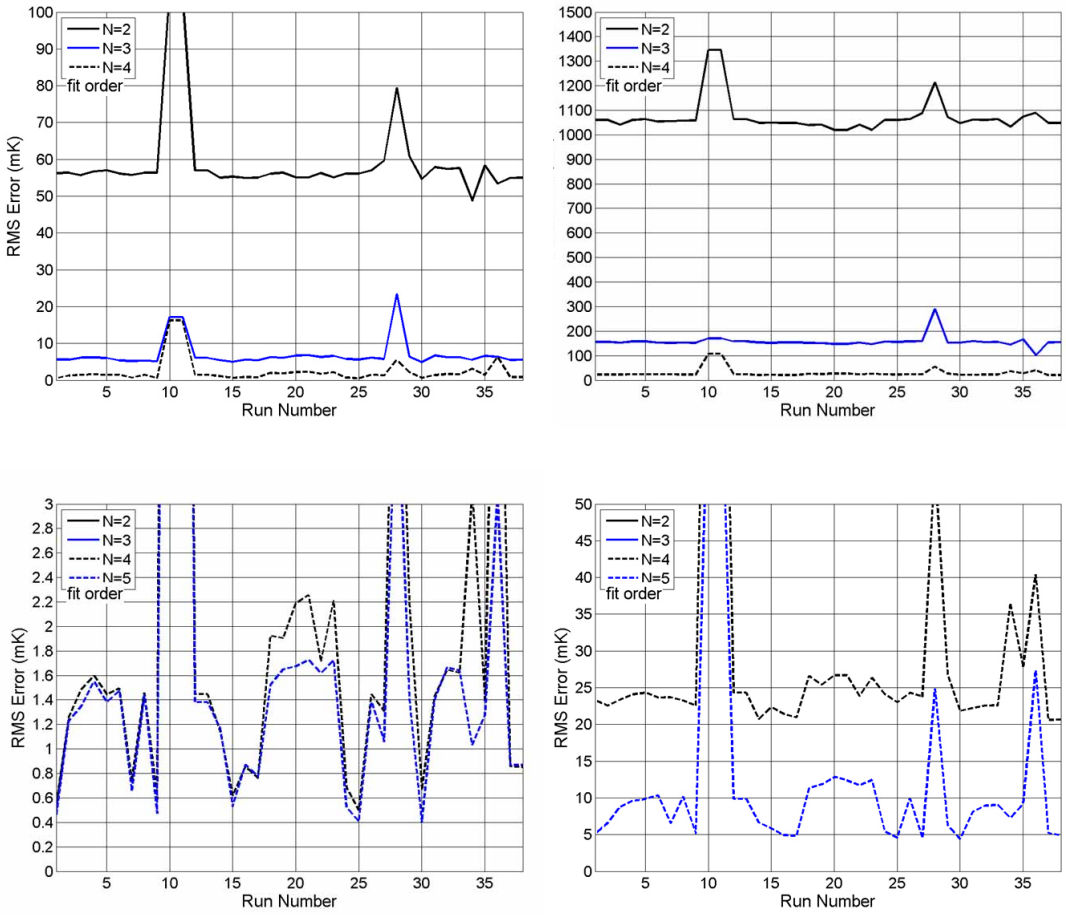

Figure A.15: RMS error vs run number for the low RMS error (left) and high RMS error (right) LST locations (4 h and 17.3 h respectively) at latitude $-26°$. Fourth order results ranged between 0.5 mK and 2.2 mK for the low LST region, and 20 mK and 100 mK for the high LST region (magnified view in lower panels).

Extra simulation space should be kept to a minimum, and only increased slowly while monitoring the results carefully. Sub-gridding was used on most runs and no problems were encountered. S11 accuracy should be set to the highest value possible. Minor parameters such as edge refinement and minimum or maximum line ratio limits did not improve the results. Every project must conduct a mesh study in the beginning to determine appropriate settings to achieve stable results because the critical geometries, which require careful meshing, will be different. If the design changes significantly, the mesh study should be repeated.

Table A.3: Meshing related simulation parameters using CST 2014 and Legacy Hex Meshing.

Run	Best RMS Error (mK)	Adapt. Mesh	Sub grid	Lines per λ	Lower Mesh Limit	Mesh Line Ratio Limit	Edge Enh.	Extra X Space (in)	Extra Y Space (in)	Extra Z Space (in)	Mesh Cells (x10^6)	S11 Min. (MHz)
1	0.6	N	Y	150	50	100	97	29.5	0.0	12.8	8.3	163.00
2[1]	1.3	N	Y	150	50	100	100	29.5	0.0	12.8	8.3	162.40
3	1.5	N	Y	150	50	100	100	29.5	29.5	29.5	13.5	163.05
4	1.6	N	Y	175	55	110	100	29.5	29.5	29.5	13.5	163.35
5	1.4	N	Y	175	50	100	100	29.5	29.5	29.5	13.0	163.50
6	1.5	N	Y	200	50	100	95	29.5	29.5	29.5	19.5	163.55
7 pass1	0.7	Y[2]	N	110	50	100	95	29.5	29.5	29.5	4.0	162.75
(8) pass2	1.5										6.8	163.30
(9) pass3	0.6										11.7	163.45
10	16.2	N	Y	110	50	0.005	25	29.5	29.5	29.5	3.3	162.65
11	16.2	N	Y	110	50	0.005	100	29.5	29.5	29.5	3.3	162.65
12	1.4	N	Y	175	50	0.005	100	29.5	29.5	29.5	13.0	163.50
13	1.4	N	Y	175	50	100	100	29.5	29.5	29.5	13.0	163.50
14 pass1	1.1	Y[3]	N	175	50	100	100	5.0	0.0	5.0	6.4	163.25
(15) pass2	0.6										10.9	163.50
(16) pass3	0.9										18.6	163.55
(17) pass4	0.8										31.7	163.55
18 pass1	1.9	Y[4]	Y	175	50	100	97	29.5	0.0	12.8	13.0	163.60
(19) pass2	1.9										4.3	163.60
(20) pass3	2.2										15.6	163.65
(21) pass4	2.3										16.8	163.70
(22) pass5	1.7										18.1	163.70
(23) pass6	2.2										19.5	163.75

[1] The dipole wire gap and wire diameter were set to 0.05″ for all runs except run 2 that used a wire gap of 0.50'.

[2] Energy based iteration. Repeat until S11 < 0.01.

[3] Energy based iteration. Repeat until S11 < 0.001.

[4] Expert based. Mesh increment automatically by 5 lines per λ

Table A.3: Meshing related simulation parameters using CST 2014 and Legacy Hex Meshing. (*Cont.*)

Run	Best RMS Error (mK)	Adapt. Mesh	Sub grid	Lines per λ	Lower Mesh Limit	Mesh Line Ratio Limit	Edge Enh.	Extra X Space (in)	Extra Y Space (in)	Extra Z Space (in)	Mesh Cells (x10^6)	S11 Min. (MHz)
24	0.7	N	Y	125	50	100	97	29.5	0.0	12.8	4.8	162.75
25	0.5	N	Y	150	50	100	97	29.5	0.0	12.8	8.3	163.00
26	1.4	N	Y	175	50	100	97	29.5	0.0	12.8	13.0	163.50
27	1.3	N	Y	50	50	100	0	29.5	0.0	12.8	0.4	162.15
28	5.6	N	Y	50	50	100	0	59.0	0.0	25.6	1.7	161.85

Table A.4: Advanced meshing related simulation parameters using the new 2014 Hex Meshing system.

Run	Best RMS Error (mK)	Adapt. Mesh	Sub grid	Lines per λ (near)	Lines per λ (far)	Edge Enh.	Cells per Box Edge (near/far)	Extra X Space (in)	Extra Y Space (in)	Extra Z Space (in)	Mesh Cells (x10^6)	S11 Min. (MHz)
29 pass1	2.2	Y[1]	Y	200	100	50	30	29.5	0.0	12.8	1.6	162.85
(30) pass2	0.7			225	125	50	45				4.3	162.75
(31) pass3	1.4			250	150	50	70				6.9	162.90
(32) pass3	1.6			275	175	50	95				10.8	163.10
(33) pass4	1.6			300	200	50	120				15.3	163.10
34 pass1	3.1	Y[2]	Y	225	125	0	100/50	0.0	0.0	0.0	3.0	163.65
(35) pass2	1.4			250	150		125/75				4.7	163.60
(36) pass3	6.3			275	175		150/100				7.0	163.75
37 pass1	0.9	Y[3]	N	225	125	0	25/100	0.0	0.0	0.0	7.3	163.65
(38) pass2	0.9			225	125		25/100				12.5	163.60

[1] 2014 Hex Mesh Expert Based. Mesh increment 25 lines.

[2] 2014 Hex Mesh Expert Based. Δ S11 set to 0.001

[3] 2014 Hex Mesh Energy Based. Δ S11 set to 0.001

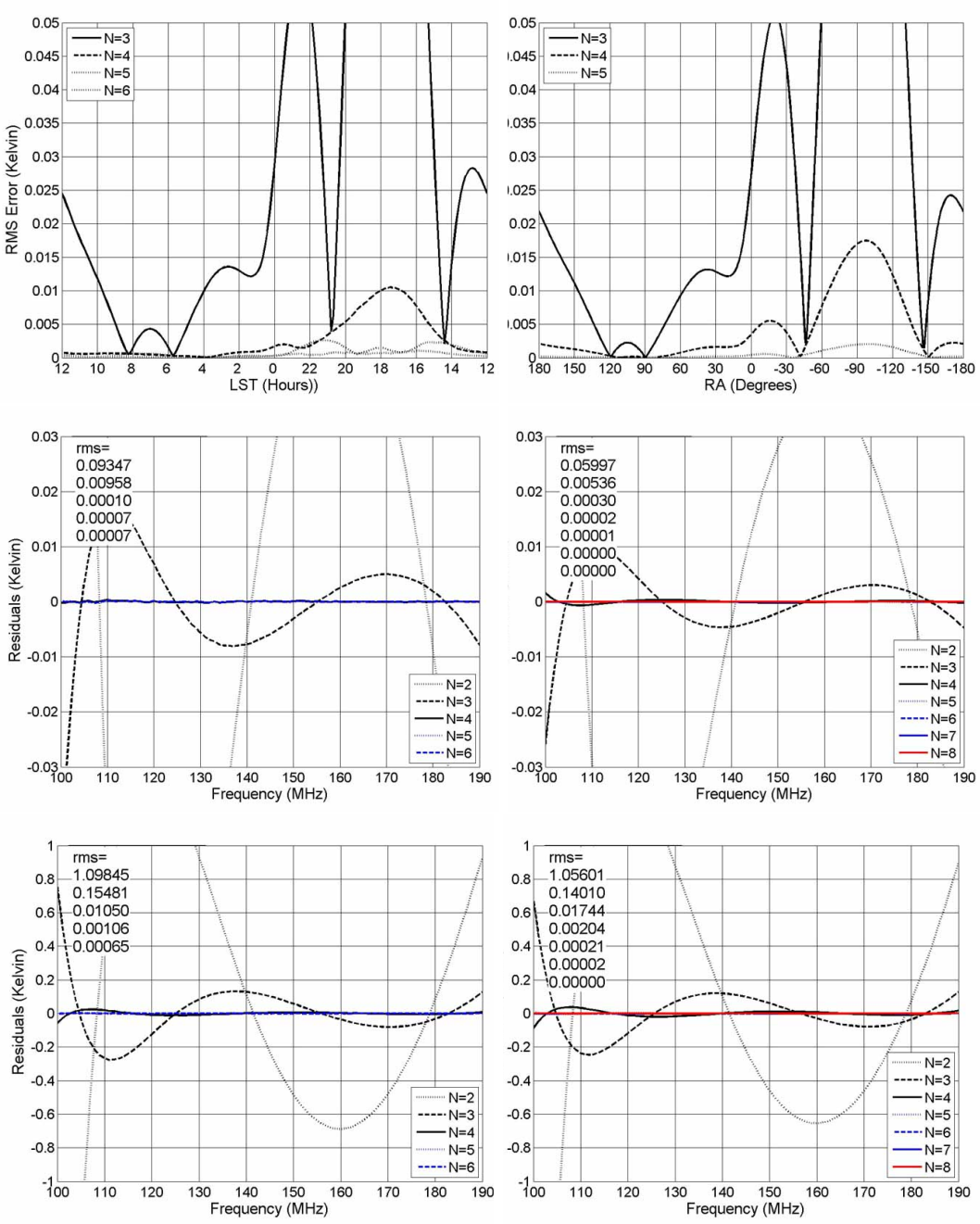

Figure A.16: RMS errors and residuals using the antenna beam from the CST simulation of the small wire dipole on the left and from using the analytic version of the beam on the on right. The top panels show the RMS error vs LST, the middle panels show the residuals taken at LST=4 h, and the bottom panels at LST=17.3 h. Note the scale of the top panels and that the RMS error decreases to the μK level.

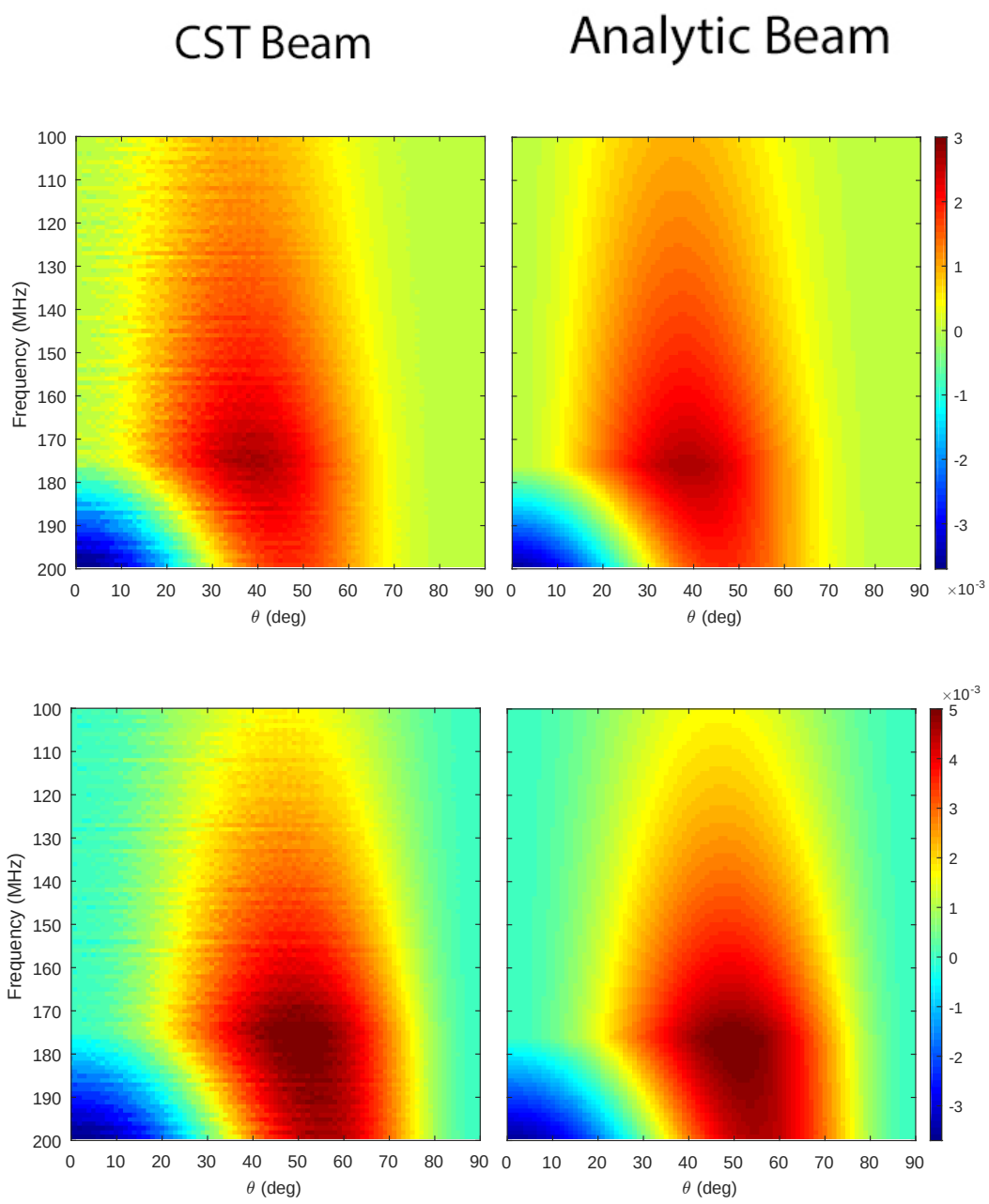

Figure A.17: Derivative plots of the short wire dipole beam derived from CST (left) and of the analytic short wire dipole beam (right). The top panels are along the excitation axis ($\phi = 0°$) and the lower panels along the perpendicular direction ($\phi = 90°$). No irregularities are noticeable other than the minor low level jaggedness of the CST beam derivative.

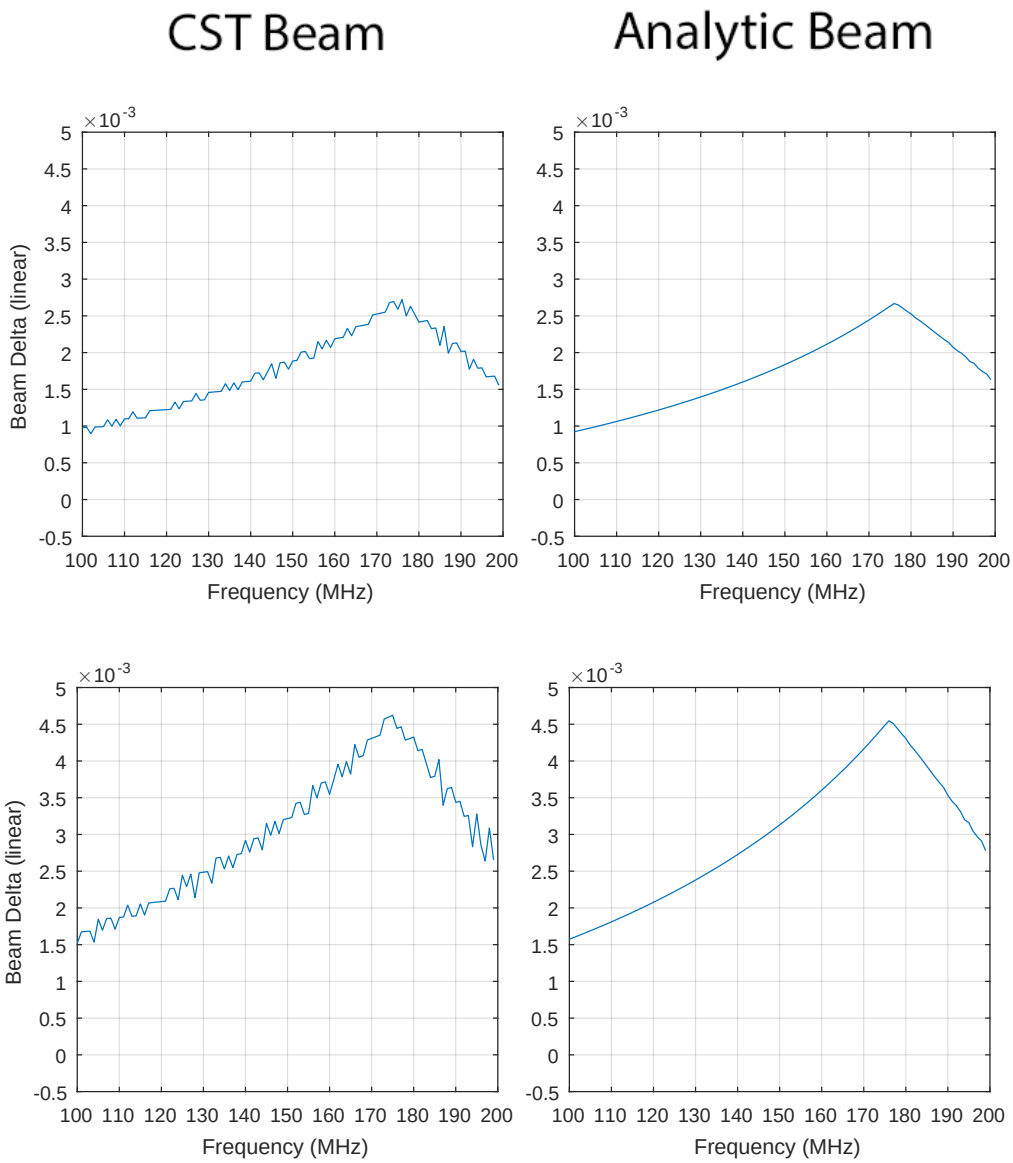

Figure A.18: Derivative plots of the short wire dipole beam derived from CST (left) and of the analytic short wire dipole beam (right) at $\theta = 40°$. The top panels are along the excitation axis ($\phi = 0°$) and the lower panels along the perpendicular direction ($\phi = 90°$). Again, no irregularities are noticeable other than the minor low level jaggedness of the CST beam derivative. The match is near perfect. Also of interest is the fact that the beam is now more symmetrical (less dependence upon ϕ) and the peaks of the derivatives are more equal than in the case of the $\frac{1}{4}\lambda$ dipole.

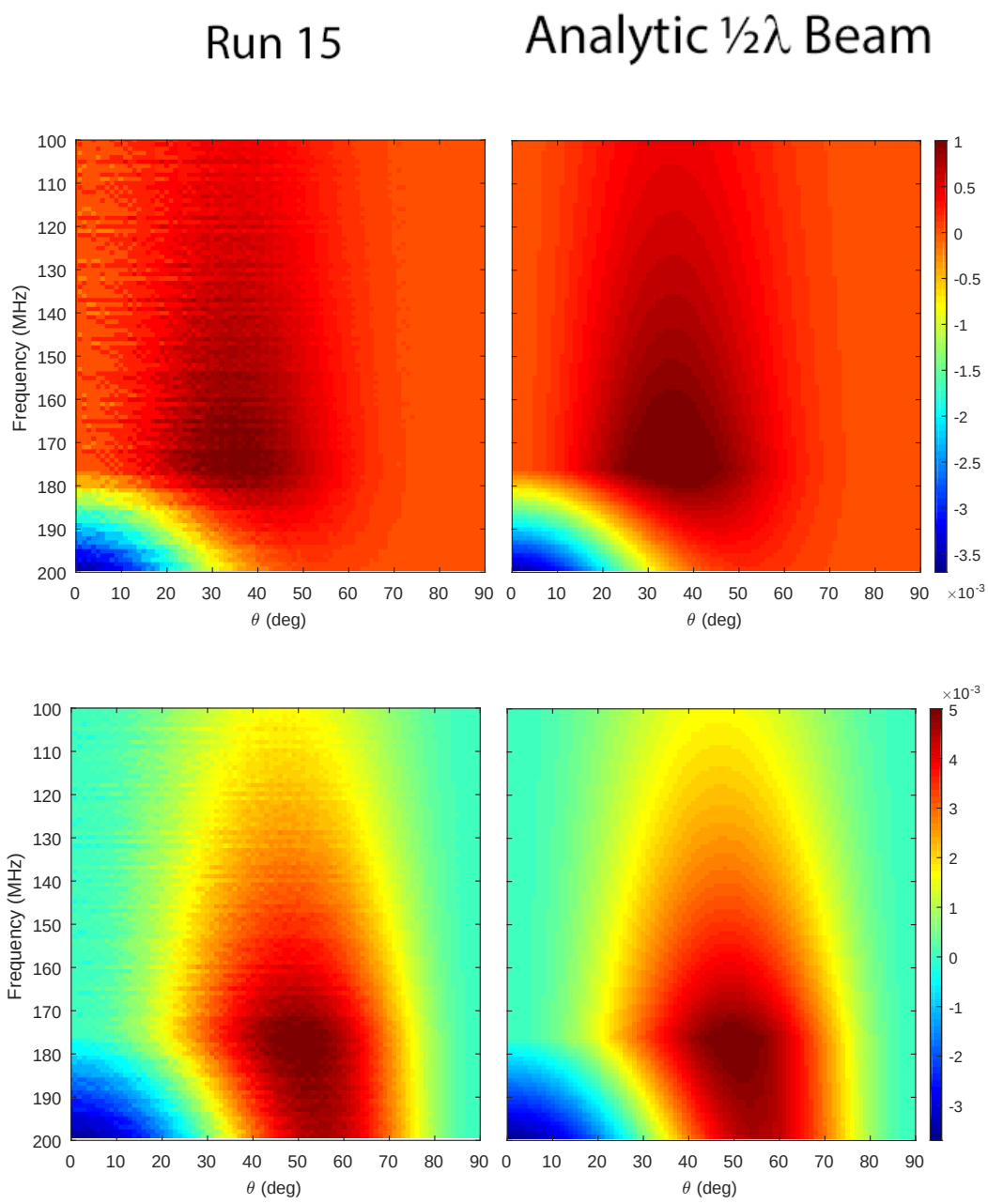

Figure A.19: Derivative Plots of the $\frac{1}{2}\lambda$ Dipole beam derived from CST run 15 (left) and the analytic beam (right). The top panels are along the excitation axis ($\phi = 0°$) and the lower panels along the perpendicular direction ($\phi = 90°$). This is an example of a beam that produced a low RMS error of 0.6 mK at LST=4 h, which is attributed to the smoothness of the beam.

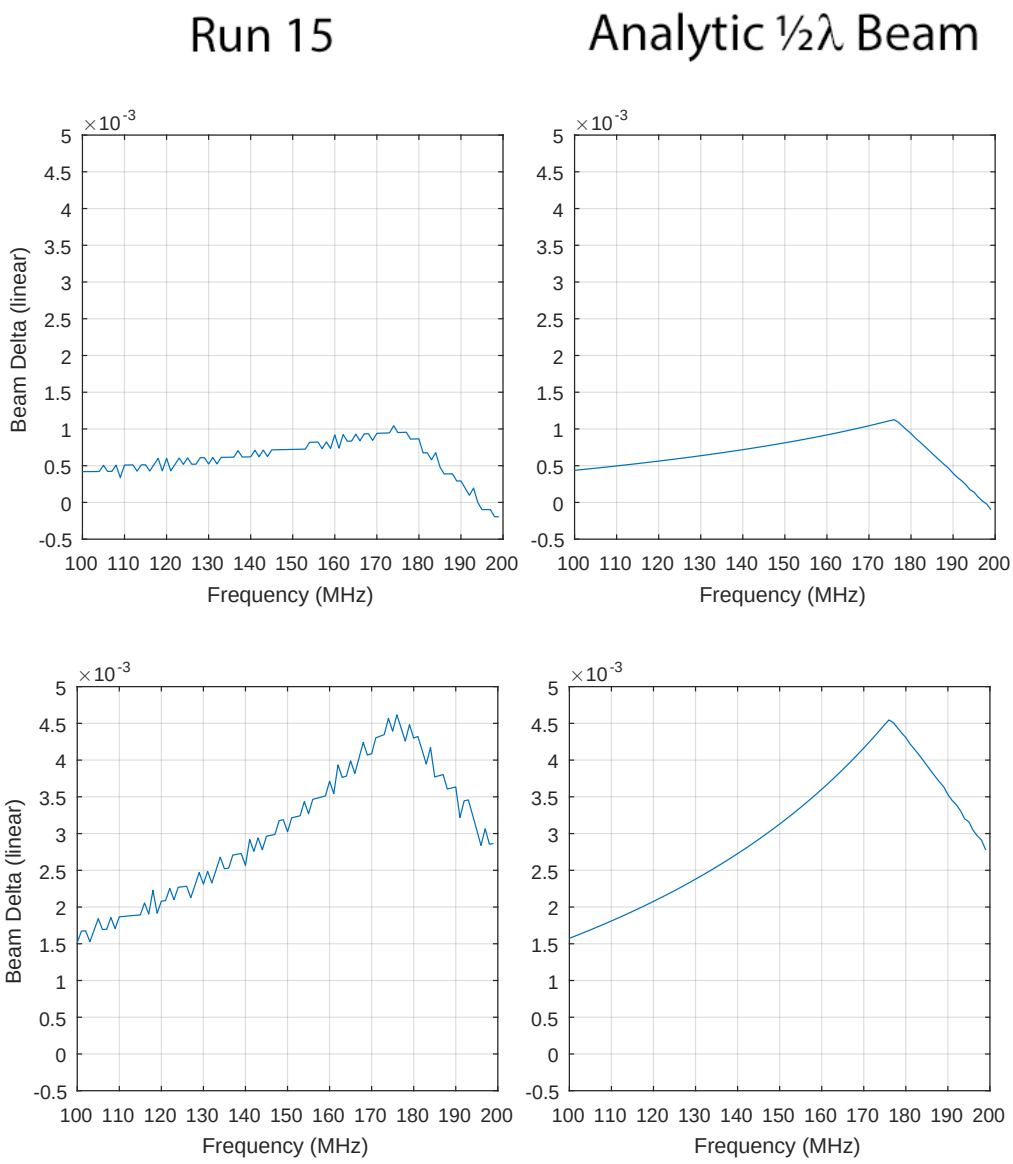

Figure A.20: Derivative plots of the $\frac{1}{2}\lambda$ dipole beam derived from CST run 15 (left) and the analytic beam (right) at $\theta = 40°$. The top panels are along the excitation axis ($\phi = 0°$) and the lower panels along the perpendicular direction ($\phi = 90°$). This is an example of a beam that produced a low RMS error of 0.6 mK at LST=4 h.

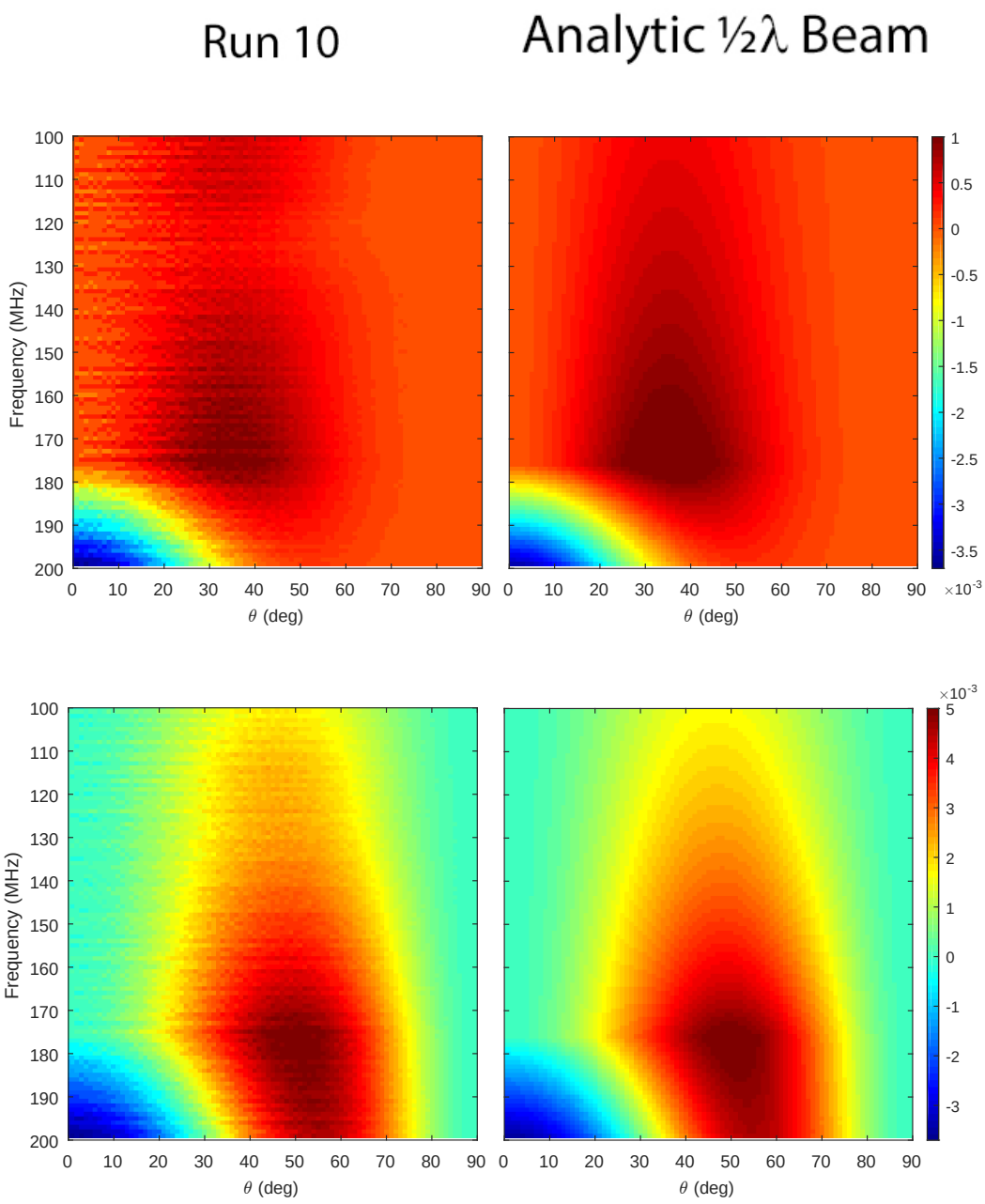

Figure A.21: Derivative plots of the $\frac{1}{2}\lambda$ dipole beam derived from CST run 10, which had a high RMS error (left) and the analytic beam (right). The top panels are along the excitation axis ($\phi = 0°$) and the lower panels along the perpendicular direction ($\phi = 90°$). This is an example of a beam that produced a relatively high RMS error of 16.2 mK at LST=4 h. Structure can be seen in the CST derived beam for $\phi = 0°$ (top left) at 125 MHz, but not in the analytic beam (top right).

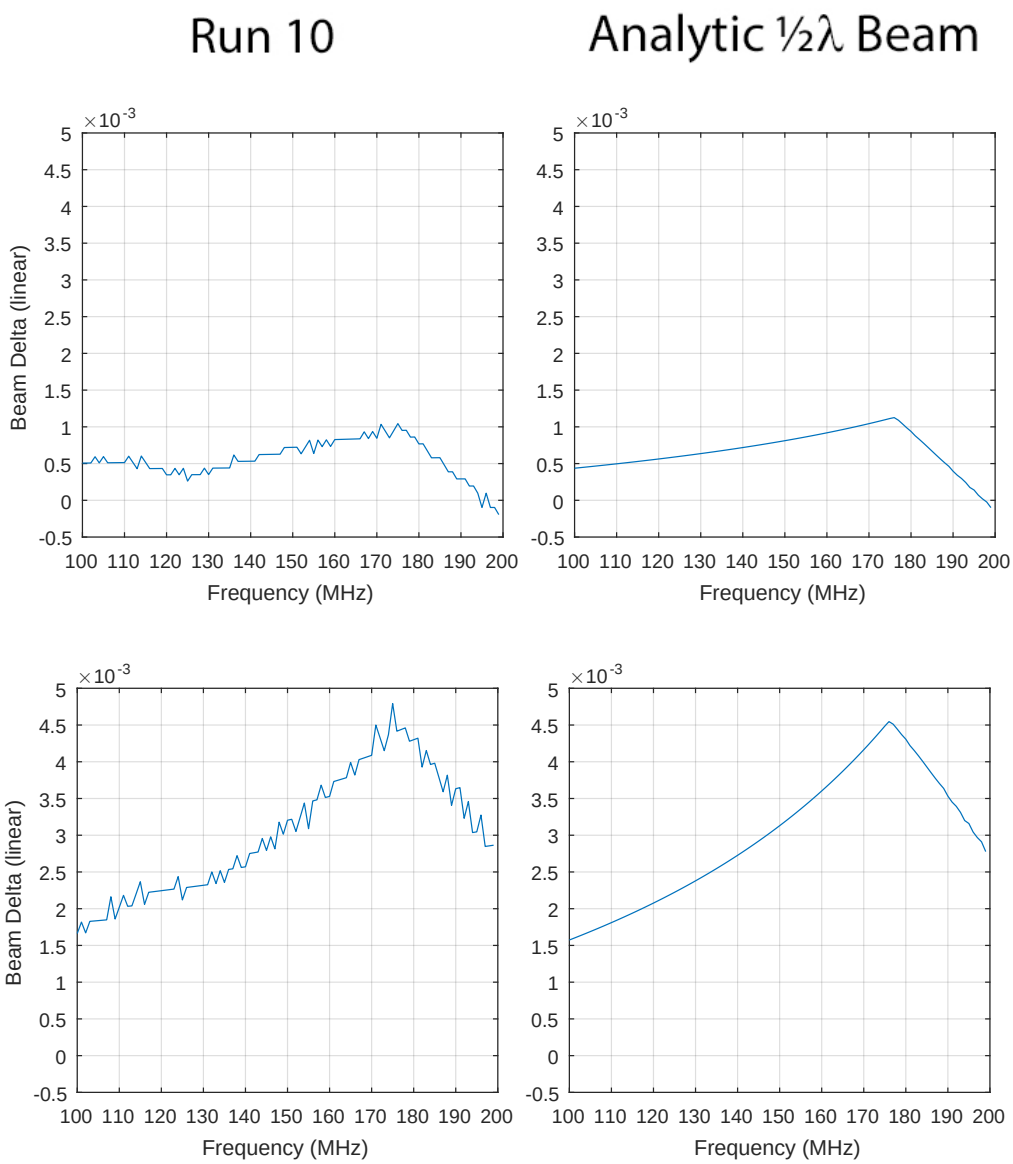

Figure A.22: Derivative plots of the $\frac{1}{2}\lambda$ dipole beam derived from CST run 10 (left) and the analytic beam at $\theta = 40°$ (right). The top panels are along the excitation axis ($\phi = 0°$) and the lower panels along the perpendicular direction ($\phi = 90°$). The change in slope below 130 MHz leads to the relatively high RMS error of 16.2 mK at LST=4 h.

APPENDIX B

GROUND PLANE SIZE VS. GROUND LOSS

B.1 Ground Loss Due to a Ground Plane of Finite Size

The best electrical environment for the EDGES dipole antenna includes a perfectly conducting infinite ground plane at the base of the antenna. Since this is not practical, a simulation study was conducted to determine the minimum size of the ground plane which would provide acceptable electrical properties. A non-ideal ground plane can cause irregularities in the electrical properties of the antenna, namely the beam's directivity and the reflection coefficient (S11) at the input of the antenna. Understanding the magnitude and cause of these effects is important because they can contribute to the overall system error. Simulations of the EDGES antenna model using a finite ground plane of various sizes were run on the model of the EDGES fourpoint antenna deployed in Nov. 2013 using Computer Simulations Technology's Microwave Studio (CST). The goal was to determine the minimum size of the ground plane such that ground loss would be at an acceptable level and that the reflection coefficient of the antenna would not adverserly affected.

The antenna model includes the Rogers' balun, the tall balun shield, the asymmetrical top cap design, and a finite solid ground plane with empty simulation space under the ground plane. The top panel of Fig. B.1 shows the simulation model and some details of the antenna, while the bottom panel show is a side view. This is a worse case simulation because the antenna in the field sits on top of soil with low conductivity, which is better electrically than free space.

The ground loss (beam power fraction below the horizon) is defined as

$$\text{G. L.} = \frac{\text{Power Below Horizon}}{\text{Total Power}}(\nu) = \frac{\int_0^{2\pi} \mathrm{d}\phi \int_{\pi}^{\pi/2} Beam(\phi,\theta,\nu) \sin\theta \,\mathrm{d}\theta}{\int_0^{2\pi} \mathrm{d}\phi \int_{\pi}^{0} Beam(\phi,\theta,\nu) \sin\theta \,\mathrm{d}\theta} \tag{B.1}$$

where ϕ and θ are the angular spherical coordinates, ν is frequency, and $Beam(\phi,\theta,\nu)$ is the directivity of the antenna's beam pattern.

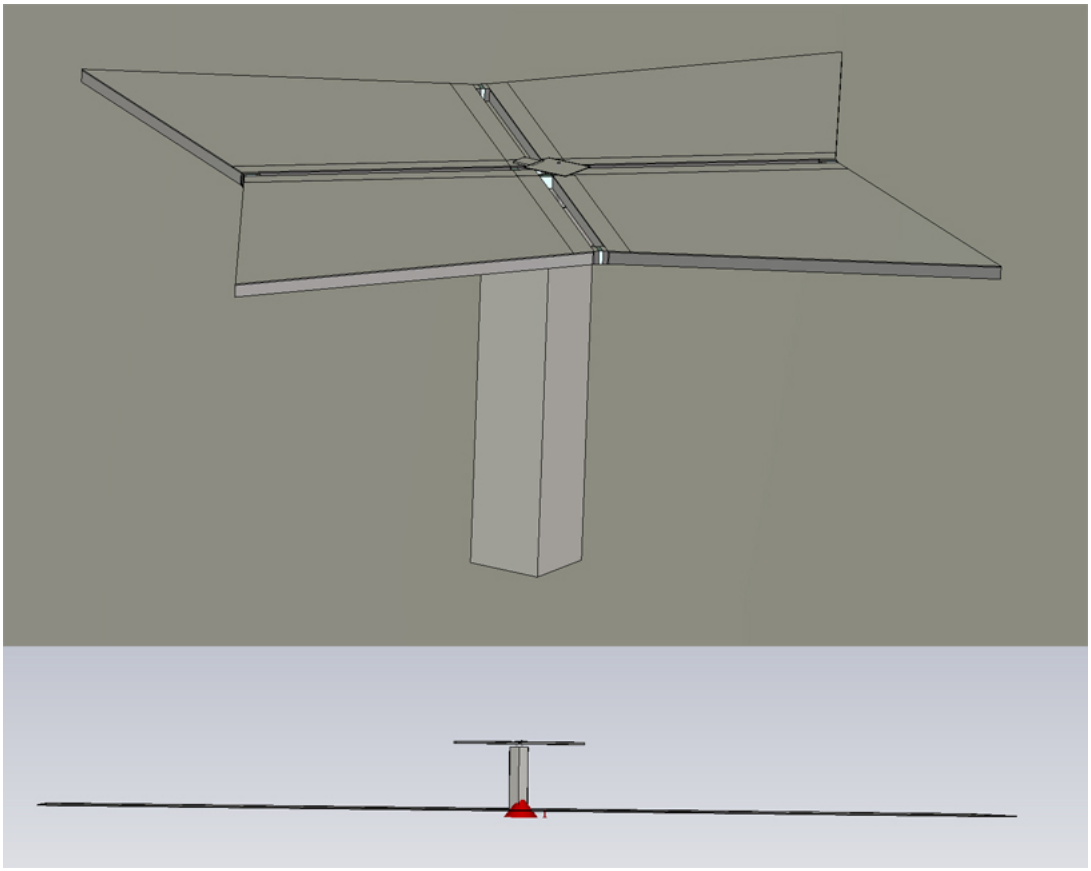

Figure B.1: Fourpoint antenna over a finite ground plane as captured in a CST model (top). The balun shield is in the middle of the antenna and the tuning top capacitor plate is in the center of the antenna on top. Side view of the antenna in free space (bottom). This scenario is a worse case scenario for a ground plane as even a rocky earth beneath the antenna will have some electrical conductivity.

Ideally, when the antenna is over a perfect ground, the antenna's directivity (sensitivity) to stimuli below the horizon ($\theta \leq \pi$) should be zero. In a non-ideal case, where the ground extent is finite, the antenna's directivity below the horizon will not be zero (see Fig. B.2) and a component of the antenna's temperature will be picked up from the ground which is assumed to be uniformly at 300K. This temperature can be computed with the following equation

$$T_{\text{ground}} = \int_0^{2\pi} \mathrm{d}\phi \int_{\pi}^{\pi/2} 300\ K \times Beam(\phi, \theta, \nu)\ \sin\theta\ \mathrm{d}\theta \tag{B.2}$$

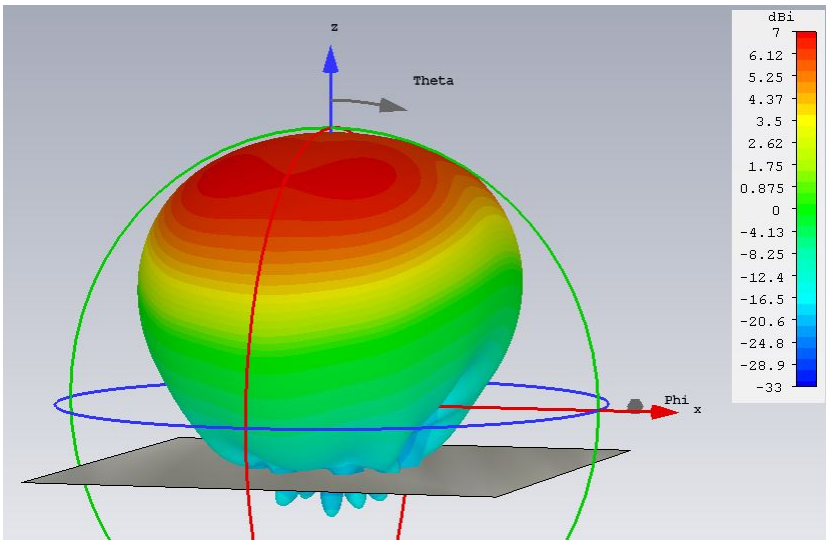

Figure B.2: EDGES 3D beam directivity pattern with a finite ground showing a small response directed below the horizon.

B.2 Description of the Simulations and Comparison with Rogers (2015)

We simulated a variety of square ground plane sizes ranging from 6' x 6' to 48' x 48'. The ground loss is plotted vs frequency in Fig. B.3. As a reference point, six feet corresponds to the wavelength at 164 MHz. Thus sizes plotted begin at 1 λ x 1 λ and end at 8 λ x 8 λ. The ground loss values obtained via CST are similar to the values in Rogers (2015) if one compares the solid ground plane to the finest mesh ground planes in the report. Note that Rogers (2015) uses 2m wavelengths (150 MHz) as the unit λ and uses FEKO (by Altair Engineering) instead of CST. Table B.1 lists the ground plane size variations and the ground loss values at 164 MHz.

Comparing the values in Rogers (2015) to the values in this report for the 1 λ and 2 λ sizes (and remembering that the λs differ by 10%), he reports losses of 5.5% and 1.5% respectively vs our CST values of 5.5% and 1.6% respectively. The CST values quoted are the minimum values along the frequency range. Also, the CST values tend to increase above these levels at the low and high ends of the frequency range (see Fig. B.3).

Table B.1: Ground loss for various sizes of square ground planes

Ground Plane Size (ft)	λ units (at 164 MHz)	Ground Loss (%)	RMS Error to a 4^{th} Order Fit (mK)
6 x 6	1 x 1	4.0	119
12 x 12	2 x 2	1.7	31
18 x 18	3 x 3	0.8	57
24 x 24	4 x 4	0.55	20
48 x 48	8 x 8	0.60	3

B.2.1 Smoothness of the Ground Loss with Frequency

Since the ground loss affects the antenna temperature, which mainly comes from the diffuse radio sky synchrotron radiation (foreground), and which must be eventually removed with polynomial fitting, more of the ground loss effect will also be removed from this fitting if its shape is smooth over frequency. Thus we fit a 5 term (4^{th} order) polynomial $\Sigma_{n=0}^{4}$ A$_n$ log $(\nu/150\ MHz)^n$ to the ground loss (assuming the ground is at 300 K) and record the RMS error of the fit to check for smoothness. Table B.1 lists the RMS errors for the fitting. We note that the ground loss values for a 48' structure are nearly the same as the 24' structure, but that the smoothness of the larger ground plane has a drastically lower RMS fitting error and as such is superior.

B.2.2 Reflection Coefficient Robustness

Also of importance is the electrical performance of the antenna. We monitored the S11 of the antenna during simulations and present the results in Fig. B.4. The conclusion is that the 6' x 6' (1 λ x 1 λ) size is not wide enough to reach the best-case

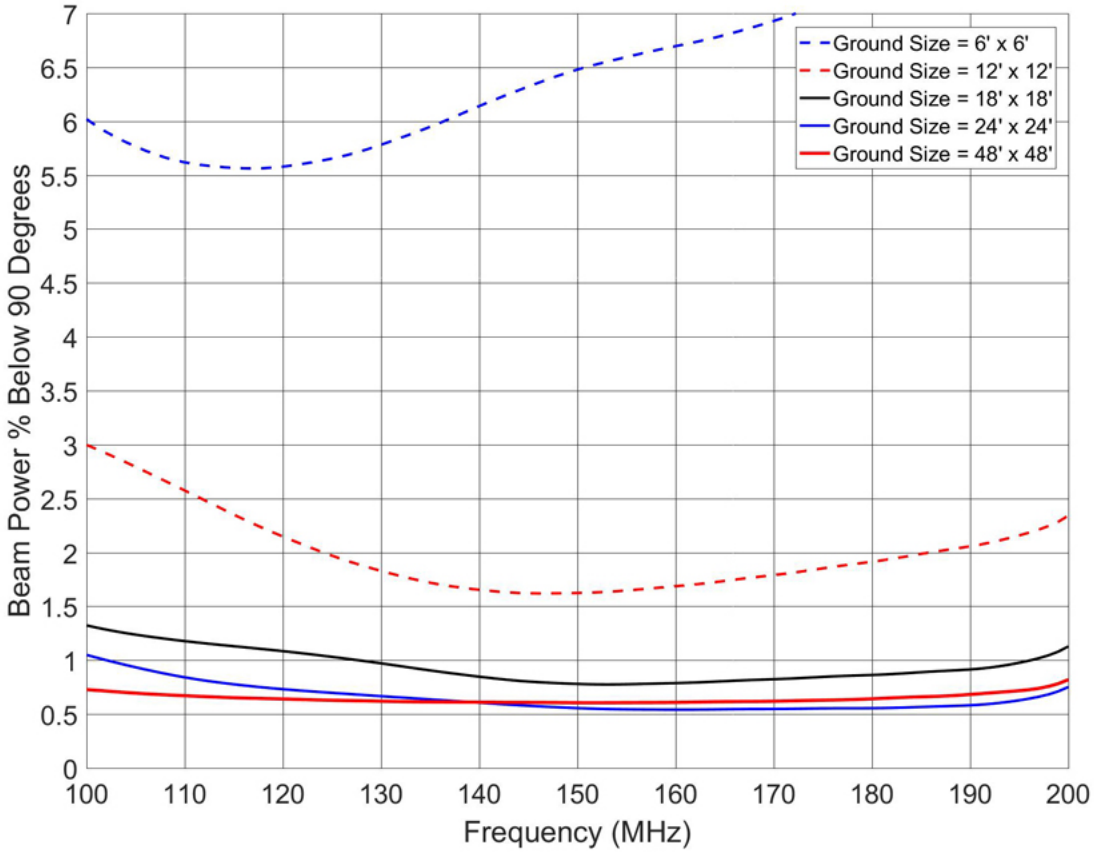

Figure B.3: Ground loss for various ground plane sizes. To achieve <1% loss the size needs to be at least 3λ x 3λ (18' x 18') in extent.

asymptotic value of the S11 parameter and that a 2 λ or 3 λ structure size is needed. Fortunately, to keep the ground loss under <1% requires a structure at least this big so that the S11 parameter will also reach the asymptotic value.

B.2.3 Computer Resources

Finite ground plane simulations are very compute intensive and can become unwieldy in both terms of time and memory required. The 3 λ x 3 λ ground plane took 10 hrs. to simulate, the 4 λ x 4 λ took 12 hrs., and the 5 λ x 5 λ took 27 hrs.

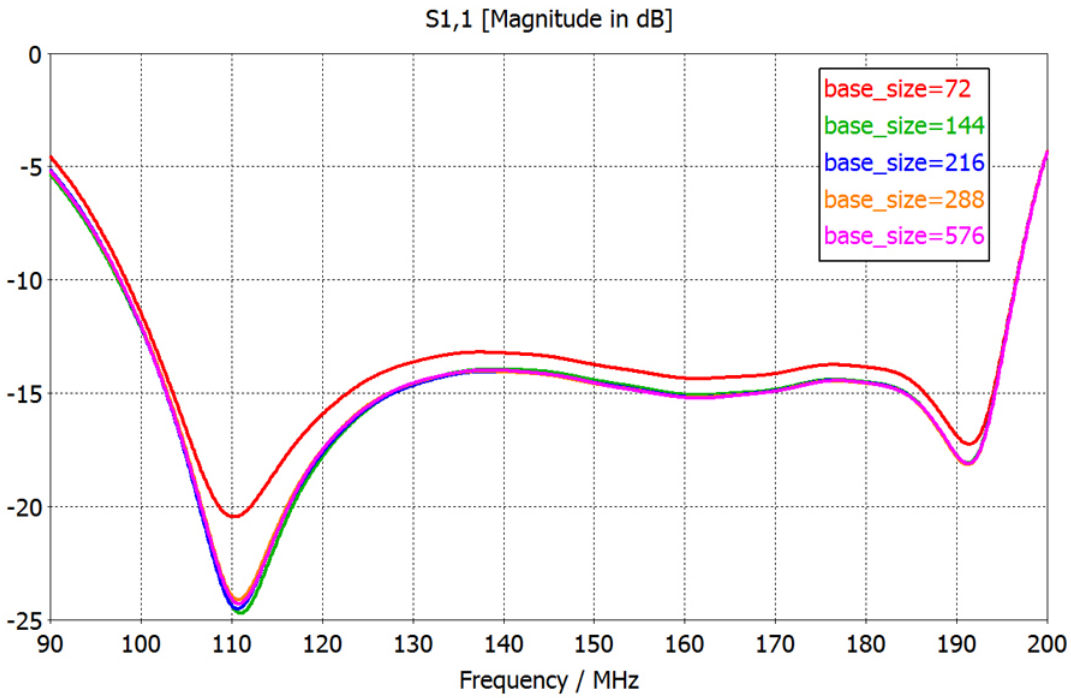

Figure B.4: Impact of the ground plane size on the reflection coefficient S11. The base size is the length in inches of one side of the square ground plane. We see stabilization in S11 when the ground plane is wider than 12 feet on a side (144 inches).

B.3 Results for Irregularly Shaped Ground Planes

At this point of the study, it became clear that a ground plane larger than our 3 λ x 3 λ solid metal ground plane would be highly desirable. However, it would be too expensive to build a solid ground plane that large and the most practical way to enlarge the ground plane was to attach 3' x 16' mesh screens that were readily available at the deployment site. Thus a small extension to the previous study was conducted to determine the effectiveness of a ground plane that is not square. Our base square ground plane in the field is 18' x 18' (3 λ x 3 λ) and by extending the edges of the square ground plane the resulting structure looks like Fig. B.5.

Referring to Table B.2 and Fig. B.6, the ground loss for the "plus" shaped ground planes is very similar to their counterparts with no corners missing. Furthermore, the

Table B.2: Ground Loss for various sizes of ground planes including "plus" shapes.

Ground Plane Size (ft x ft)	λ units (at 164 MHz)	Ground Loss (%)	RMS Error to a 4^{th} Order Fit (mK)
18 x 18	3 x 3	0.8	57
24 x 24	4 x 4	0.54	20
24 x 24 minus corners	4 x 4	0.54	21
30 x 30 minus corners	5 x 5	0.51	13
48 x 48	8 x 8	0.60	3

smoothness of the ground loss with frequency is nearly identical to their full square counterparts, while keeping the benefit of lower RMS fitting errors. Thus extending the ground plane with mesh sheets, without covering the corner areas, is a very practical way to create larger ground planes.

B.4 Conclusion

We determined that a 4 λ x 4 λ sized ground plane would meet our ground loss and our S11 stability requirements. Furthermore it could be implemented by starting with a 3 λ x 3 λ square and extending each side an additional λ in a plus-shaped configuration.

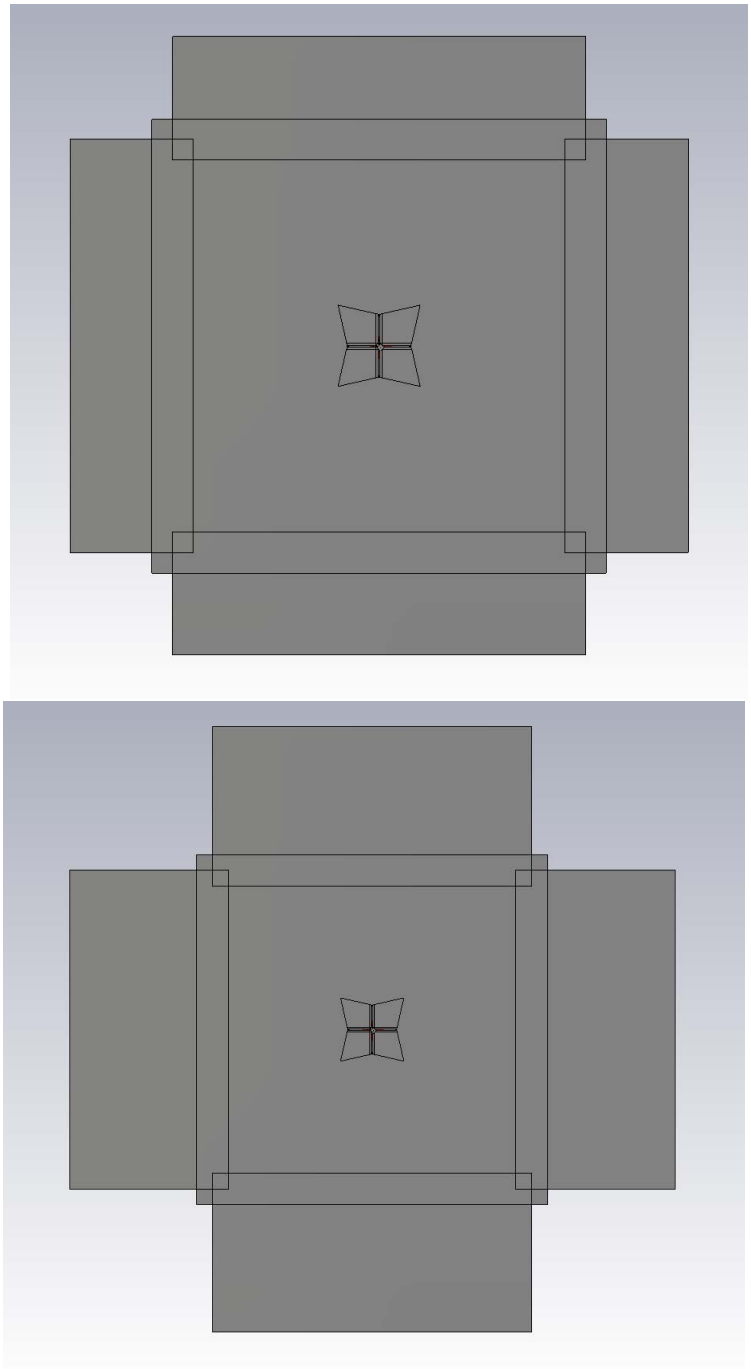

Figure B.5: Extending the 18’ x 18’ ground plane with one 3’ x 16’ extension sheet on all four sides (top). The equivalent structure is similar to a 24’ x 24’ square with 6’ x 6’ sections removed from each corner. Using two extension sheets to create a 30’ x 30’ square with 12’ x 12’ corners missing (bottom).

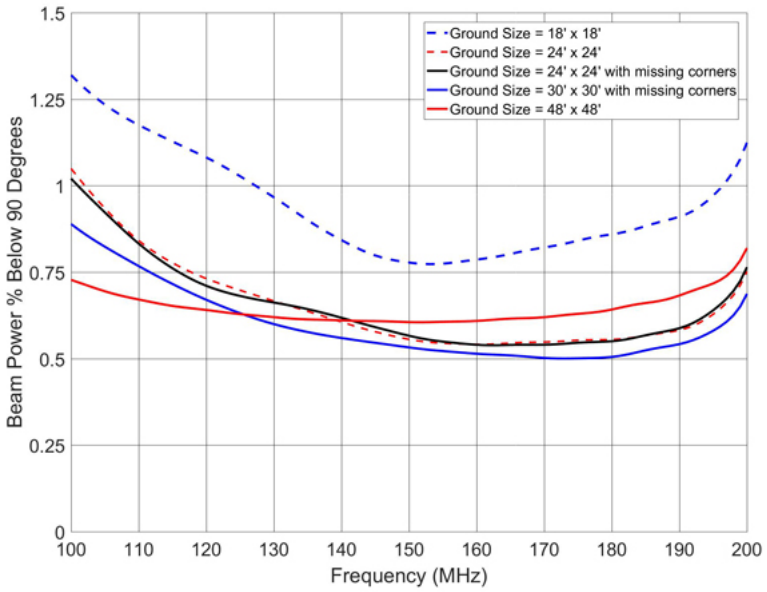

Figure B.6: Ground loss for various ground plane sizes for comparison against the "plus" shaped structures. The "plus" shaped structures have similar ground loss as their counterparts with no corners missing. The larger ground planes do not always have absolutely lower ground loss at all frequencies, but the ground loss shape is smoother with frequency, aiding foreground removal.